Master Thesis

Characterisation of a neutron experimental station at the Lund Ion Beam Analysis Facility

Markus Kristensson

Nuclear Physics Division

Supervisor: *Dr. Linus Ros*
Co-supervisors: *Dr. Charlotta Nilsson*
Dr. Robert Frost
Prof. Per Kristiansson

October 27, 2018

LUNDS UNIVERSITET
Lunds Tekniska Högskola

Abstract

At the 3 MeV light ion accelerator of the Lund Ion Beam Analysis Facility (LIBAF), a beamline is about to be constructed with the purpose of producing neutrons as a higher yield complement to the current Source-Testing Facility. When operational, the beamline will provide the possibility of tagging both thermal and fast neutrons. These neutrons will be used to test and characterise new available materials to improve future detector systems.

In this thesis, evaluations of three aspects of accelerator-based neutron production are presented: high yield neutron producing reactions and their related target materials, effective moderators as well as lower yield neutron producing materials to be used in a beam dump. The evaluations are based on literature studies, calculations and an experiment conducted at LIBAF in the late fall of 2017. The thesis is to serve as a decision basis for the construction of the coming beamline.

The results of the evaluation indicated that the use of two different targets will be beneficial for the coming beamline. The use of a beryllium target with impinging deuterons will result in the highest yield of neutrons for the considered reactions. The reaction ^{9}Be(d,n)^{10}B is suitable for producing neutrons which are to be tagged using a deflector system. A second target of tritiated titanium (TiT_x) will be required if the facility is to provide fast coincidence measurements with the neutron and the recoil of the T(d,n)^{4}He reaction. The feasibility of LIBAF of providing tagged fast neutrons with a target of tritium was demonstrated.

For the thermalisation of the created neutrons, suitable moderators were found to be both hydrogenous or deuterated materials. Which material to choose will depend on if a higher thermal flux is prioritised over a higher brilliance. Simulations to optimise a suggested moderator design will be required.

Materials which are to be considered for the use in a beam dump at LIBAF are required to result in a low yield of neutrons for incoming protons or deuterons. This is to reduce the activation of the material and to reduce the background. Both gold and tungsten were found to be beneficial. For a final decision thereof, simulations related to the activation of these materials will be required.

Preface

The work of this thesis was performed as part of the Lund Ion Beam Analysis Facility (LIBAF) group at the division of nuclear physics of Lund University. The experiment presented was conducted at the micro beam laboratory of LIBAF during the late fall of 2017.

I would like to start by thanking the people of the division of nuclear physics for your welcoming attitudes and helpful working environment.

The following persons deserve a special thank you. Firstly, my supervisor Linus Ros for guiding me through the bulk of this thesis and for all of your work with the experiment. My co-supervisor Per Kristiansson for your time, calm explanations and supervising. My co-supervisor Charlotta Nilsson for your proofreading, reviewing, helpfulness and cheerful approach. Last, but not least, my co-supervisor Rob Frost for invaluable support on the experimental chapter of this thesis as well as on language skills.

I would also like to acknowledge the input of the following persons. Mikael Elfman for your help with the measurements with the tritium target. Nathaly De La Rosa for your input on statistics, KMAX and for Spanish lessons. Jason Park for your input on the χ^2-test. Jan Pallon for lending me the booklet about the physics of nuclear reactors. Nicholai Mauritzson for the discussion of the normalisation of the experimental yield. And finally Anton Såmark-Roth, for always being ready to assist, for valuable discussions of physics, for good advice and many pleasant lunches. Thank you all.

Popular Scientific Summary

Evaluation of materials for target, moderator and beam dump for accelerator based neutron production

Markus Kristensson

A new experimental station for neutrons is to be constructed at the research facility Lund Ion Beam Analysis Facility (LIBAF), complementing the current Source Testing Facility with a higher neutron flow and with the possibility of tagging both thermal and fast neutrons to identify their energies. These neutrons will be used to test and characterise new available materials to improve future detector systems. This thesis includes an evaluation of reactions and materials producing many neutrons through bombardment of accelerated charged particles (protons and deuterons). Also evaluated are materials used to effectively reduce the energy of neutrons and suitable materials for a beam dump.

Neutrons

The neutron is a particle which, together with the proton, is a part of the nucleus of most elements. As neutrons are particles without electrical charge, they can be used to see things in e.g. archaeology artefacts, biological samples or material sciences which would otherwise be invisible to an eye or to other particles.

Producing neutrons

Different sources of neutrons exist. In nuclear power plants, neutrons are produced by splitting heavy atoms in a process called fission. At the European Spallation Source, a coming neutron experimental facility in Lund, neutrons will be released as highly energetic charged particles (ions) bombard a target of a heavy metal. At LIBAF, a small particle accelerator will be used to produce neutrons through fusion, as is happening on the sun where lighter elements react with each other to form heavier ones. In the thesis, the element which was found to produce the most neutrons per second in calculations and in the experiment was beryllium with bombarding deuterons (heavy hydrogen). The calculated flow for a current of 10μA was close to 9 billion neutrons per second.

Slowing down neutrons

Depending on their energy, neutrons interact with other atoms differently. Slow neutrons, which are useful in research, are obtained by letting the released neutrons from the fusion reaction bounce back and forth in a material called a moderator. With every bounce, the energy of the neutron is reduced. If the moderator consists of heavy atoms, the process of slowing down is inefficient compared to if it consists of atoms of similar mass to the neutron. A similar effect can be seen in an everyday experiment where a ping-pong ball first is shot on a billiard ball and then on another ping-pong ball. The materials which were found to slow down neutrons the fastest were water or plastics, both containing many hydrogen atoms which are of comparable mass to the neutron. Other good materials found were those being rich with heavy hydrogen, an atom twice as heavy as a neutron.

Beam Dump

In the beamline, a device which flips the beam between the target and the beam dump will be used. This will enable energy measurements of slower neutrons as their time of creation will be

known as well as the time of detection. At the beam dump, the incoming ions should be captured without releasing many neutrons. The smaller the number of neutrons produced, the less the beam dump will become radioactive. The evaluation of possible beam dump materials indicated that both gold and tungsten were suitable materials. In the experiment, a number of materials were found to be directly unsuitable: carbon, materials involving carbon (steel and tungsten carbide) and titanium.

Coincidence measurements

An important experimental technique in nuclear physic is based on the detection of two particles at the same time. This is called coincidence measurements. The most suitable reaction for such measurements was found to be the fusion of heavy hydrogen with super heavy hydrogen (hydrogen with two neutrons). This fusion reaction produces a neutron and a heavier helium ion. If the energy of the incoming beam of heavy hydrogen is low, the helium nucleus will be very likely to leave the target. By placing a neutron detector and an ion detector at two different positions, these particles can be measured within the defined time window. The setup is indicated in Figure 1. During the experiment in this thesis, the neutron detector was placed at the three different angles indicated in the setup. In Figure 2, the result of these measurements are shown. On the vertical axis, the energy of the helium particle is indicated. It is plotted to the deposited energy of the detected neutron on the horizontal axis. This is a demonstration of the ability of LIBAF of providing such measurements.

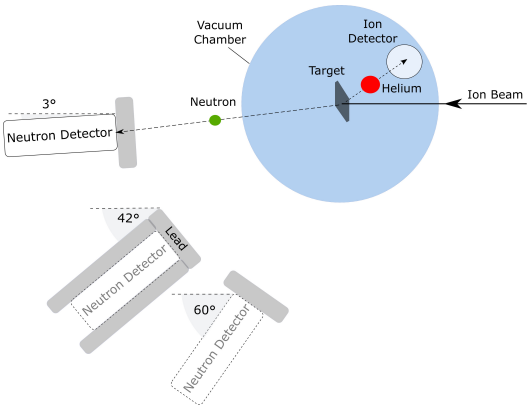

Figure 1: The setup of the coincidence measurement.

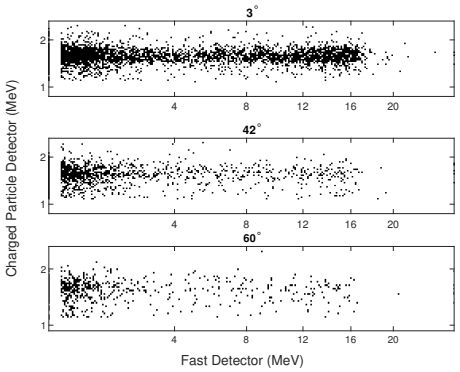

Figure 2: The energy of the particles detected simultaneously in the ion detector (vertical axis) and the neutron detector (horizontal detector).

Acronymns

ADC	Analogue to Digital Converter
DAQ	Data Acquisition
EXFOR	Experimental Nuclear Reaction Data
ESS	European Spallation Source
HV	High Voltage
LIBAF	Lund Ion Beam Analysis Facility
MP	Moderating Power
MR	Moderating Ratio
PE	Polyethylene
PMT	Photomultiplier Tube
SRIM	Stopping and Range of Ions in Matter
STF	Source-Testing Facility
TDC	Time to Digital Converter
ToF	Time-of-Flight

Contents

Chapter 1

Introduction

As revealed by its name, the neutron is a particle without electric charge. Even though being chargeless, it still has a magnetic moment. In its free form, it is unstable with a half-life of 10.6 min, decaying to a proton, an electron and an antineutrino (β^-) [1]. It is almost of equal mass to a proton, but is 1839 times heavier than an electron (the proton is 1836 times heavier). Neutrons can be characterised according to their energy. From the nuclear reactions of relevance for this thesis, fast neutrons are created (E>0.25 eV), while thermal neutrons (E=0.025 eV) are obtained as the neutrons scatter and lose energy on different materials until they reach thermal equilibrium with the surrounding atoms. Neutrons of different energies can beneficially be used to probe matter for a number of reasons. Because of their chargeless characteristics, neutrons can be used to penetrate deep into a target nucleus to study atomic structures or to study the insides of a running engine [2]. Because of their magnetic moment, neutrons can be used to study phenomena related to magnetism. Its range of usefulness stretches from fundamental research and material development, to applications within chemistry and biology. Also worth to note is their usefulness as non-destructive probes, which is of importance to fields like archaeology, art and homeland security.

The coming European Spallation Source (ESS) is about to put Lund at the centre of European research using neutrons. Its first neutrons are expected in 2022, but once the facility is fully operational, its unprecedented high brightness will provide new possibilities to measure and characterise e.g. materials, the biology of bacteria and viruses as well as atomic structures [2]. At ESS, the probing neutrons will be created through the process of spallation. On their way to the object of investigation, a large quantity of the created neutrons will disappear through scattering events or nuclear reactions. To utilise as much of the remaining neutrons as possible, efficient neutron detectors need to be developed and employed. The commonly used materials for these detector systems have either been poisonous and inflammable or expensive because of low availability. New materials, which could possible replace the existing ones, have become available. However, thorough testing and characterisation is needed in order to verify these materials.[3]

Presently, the Source-Testing Facility (STF) in Lund uses time tagged fast neutrons to characterise detectors [4]. As the interaction of neutrons with matter is energy dependent, another highly interesting energy region is that of thermal neutrons. At STF, simulations of the use of tagged thermal neutrons have been performed. This setup will be suitable for longer and continual measurements. As a compliment to the STF, the particle accelerator of the Lund Ion Beam

Analysis Facility (LIBAF) can be used to produce neutrons through a fusion reaction using a beam of protons/deuterons impinging on a target with low mass number. Such a setup will be beneficial for shorter measurements and would enable a higher flow of neutrons compared to the current source at STF. The produced neutrons can be tagged using two different approaches. For the thermal neutrons, the use of a deflection system will give a window of time for neutron production. Thereafter, through the use of the time-of-flight method (ToF), the energy of the detected neutrons can be decided. For the fast neutrons however, the recoil of the reaction will need to be utilised.

Beyond the increase in flux and the possibility of tagging both thermal and fast neutrons, accelerator based neutron production is beneficial from the perspective of versatility in providing neutrons of different energies to a user. Also, the neutron production can easily be turned off when it is not needed, simply by shutting down the accelerator. Evidently, the cost of constructing a new accelerator facility for neutron production would be large. Since much of the needed infrastructure already is in place at LIBAF, the required investments would mainly be limited to the construction of the new beamline and the required security systems.

Purpose and Method

The main purpose of this thesis is to evaluate different aspects related to the coming neutron beamline at the accelerator of LIBAF. The evaluation will include the following three topics:

- Target materials and reactions for high neutron production.
- Effective moderation materials.
- Low neutron-producing materials for a beam dump.

To evaluate and find suitable materials for these three aspects of the coming beamline, both literature studies, calculations and experimental verification will be employed.

Contents

To begin with, the physical background of importance for producing and detecting neutrons is presented in Chapter 2. Subjects included are the cross section, ion and matter interaction, moderation and neutron detection. In the following chapter, a theoretical evaluation is presented concerning possible target, moderator and beam dump materials. Parameters like neutron yield, Q-value, moderation efficiency and pulse broadening will be discussed. In Chapter 4, an experimental evaluation of most of the subjects covered in Chapter 3 is given. Before the results are presented, the experimental setup, as well as the treatment of the data, is discussed. The theoretical and experimental evaluation leads up to a final discussion where a recommendation of which reaction, moderator material and beam dump material to use in the coming neutron beamline.

Chapter 2

Physical Background

Scientific experiments involving neutrons require a wide knowledge of different scientific disciplines. This chapter introduces the most relevant topics needed related to nuclear physics. The subjects covered include a definition of cross section, the interaction between ions and matter, how to slow neutrons down to the desired energy as well as how to detect them.

2.1 Cross Section

The concept of cross section is related to most of the topics covered in this thesis. As will be seen, the concept appears in the formulas when neutrons are produced using nuclear reactions, when the produced neutrons are slowed down using a moderator material and when they are to be detected. Because of its centrality when the possible outcomes of an experiment are described, it is natural to begin with an investigation of this subject.

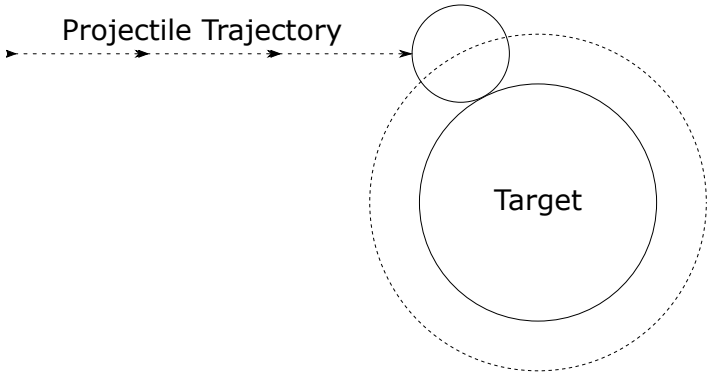

Figure 2.1: Classical representation of cross section through a hard sphere collision of a projectile and target. Inspired by [5].

The starting-point of explanation is the hard sphere collision of a projectile and a target seen in Figure 2.1. The projectile will be on a collision path if the distance between the centre points of the projectile and the target is less than the sum of their radii. The surface area of the circle

resulting from this sum forms the classical representation of the cross section (σ). The unit of σ is barn, where 1 barn = 10^{-28} m^2. The order of magnitude of barn can be understood from a classical representation since the radius of a nucleus is in the order of 10^{-14} m.[5]

In Chapter 3.1, it will become evident that the classical model of the cross section fails to describe a number of phenomena which affect its magnitude. In Figure 2.2 three such phenomena related to nuclear fusion are highlighted, tunneling, resonances and high-speed decay. Also herein, a classical model of the cross section (marked with dots) is compared to a modified model. As can be seen, the classical model do not incorporate the effect of tunneling, high speed projectiles and resonances. These are quantum mechanical effects caused by the wavelike characteristics of nuclear particles. They do all have a profound effect on the cross sectional value.[6]

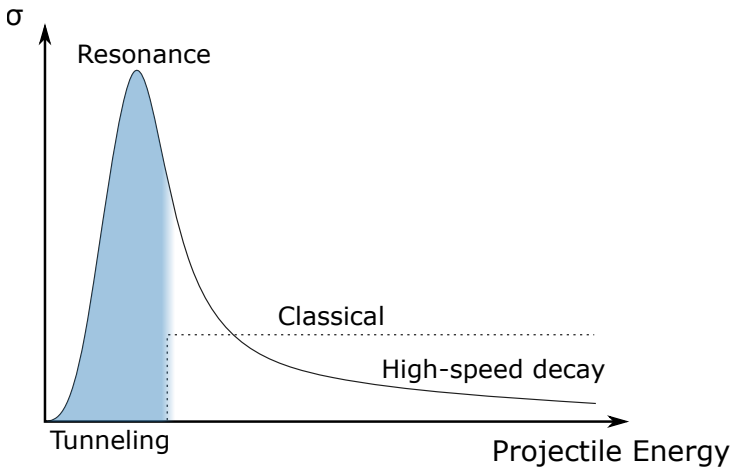

Figure 2.2: The quantum mechanical modifications to a classical model of the cross section. Inspired by [6].

Tunneling is the first phenomenon which modifies the cross section. The reason the classical model of the cross section does not start at zero energy in Figure 2.2, is because of the repulsion occurring between like-charged nuclei. Classically, a particle with too low kinetic energy would not be able to penetrate such a barrier, which translates to an impossibility for the projectile to participate in, for example, a nuclear reaction like fusion. This repulsion will be discussed further in Chapter 2.2.2. However, the modified model in Figure 2.2 indicates that it is possible for projectiles with less kinetic energy than the Coulomb barrier to participate in nuclear reactions. This is the quantum mechanical concept of tunneling which consequently does imply that the cross section for lower projectile energies must be increased compared with the classical model.[7]

The second phenomenon involves the decrease of the cross section for increased projectile energies. Related to what will be discussed in the section about fusion, this decrease corresponds to the decreased time for the nuclear distributions of the projectile and the target to overlap and thus form a coupled interaction. Hence, for fusion the classical cross section must be modified to incorporate a decrease of the cross section as the projectile energy is increased.[6]

The third phenomenon is the peak seen in Figure 2.2 related to resonant reactions. Again, this is a phenomenon which is related to the further discussion of nuclear reactions. An appetiser is that these resonances are possible because of the presence of excited energy levels in the compound nucleus formed. If the obtained excitation energy from the incoming projectile is roughly similar to an energy level in this compound nucleus, the reaction will be facilitated. Thus, the classical

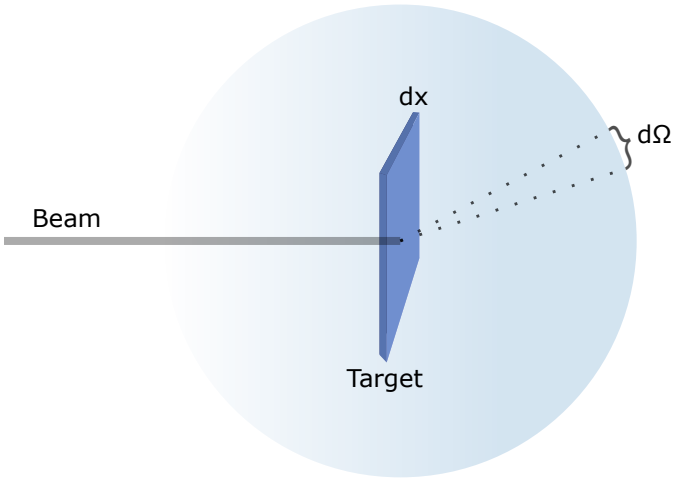

Figure 2.3: A beam of particle is directed perpendicular on a target material. As a result of the interaction, the particles are scattered anisotropically (gradient of blue sphere). Inspired by [8].

cross section needs to be modified anew, this time to incorporate the increase of the cross section caused by resonances in the compound nucleus.[5]

Figure 2.3 is a schematic illustration of the scattering cross section. The following discourse is based on [8] if not otherwise stated. Herein, a beam of particles with a uniform flux is directed onto a target. The flux, F, is defined as the number of particles passing through the unit area per second, F $[\mathrm{m}^{-2}\ \mathrm{s}^{-1}]$. The density of the target is N atoms per volume. The particles which have interacted with the target atoms are scattered into different angles represented by the blue coloured circle. The gradient of the colour indicates that the scattering in this figure is anisotropic. A definition of the differential cross section is obtained if the average number of scattered particles per unit time, N_s, in a certain angle, $\mathrm{d}\Omega$, is regarded. This is summarised in Equation 2.1. Thus, the differential cross section is defined as the proportion of the average number of scattered particles into $\mathrm{d}\Omega$ per time over the incoming flux. Generally, σ will vary as a function of the measured angle of the outgoing particles. By integrating the differential cross section over all solid angles, a total cross section is obtained as a function of energy.

$$\frac{d\sigma}{d\Omega}(E,\Omega) = \frac{1}{F}\frac{dN_s}{d\Omega}, \tag{2.1}$$

The cross sectional value of Equation 2.1 is the microscopic cross section. It is related to one target atom. Often a macroscopic cross section is defined, pertaining to the material as a whole. Equation 2.2 gives this macroscopic cross section as the product between the number of atoms per volume and the microscopic cross section.[5]

$$\Sigma = N\sigma \tag{2.2}$$

Carelessly, the concept of cross section is sometimes equated with the probability of a certain reaction to occur. This is only partially true as it is obvious that the interaction probability also will depend on the thickness of the thin target (dx) as well as on the density of target atoms per volume. The probability is also proportional to what type of interaction that occurs. The

expression of this interaction is quantified using σ. By combining the three parameters, Equation 2.3 gives the interaction probability (dP) for one particle in a thin sliced target material.[9]

$$dP = dxN\sigma \tag{2.3}$$

This equation is only valid if dx is small. By invoking this limitation, multiple target atoms are prevented to shield each other from the point of view of the incoming particle. Without this limitation, multiple target atoms could be shielded from the projectile. Also noteworthy is that σ in Equation 2.3 is the total cross section for a given energy. Again, if the differential cross section is given, this parameter can be obtained through the integration of Equation 2.1 over all solid angles.

If the cross section value is known, Equation 2.3 can be used to calculate the expected number of interaction events per unit time. This reaction rate, R, is given in Equation 2.4 over all solid angles, where n_{inc} represents the quantity of incoming particles per unit time and is given by the product of F and A, where A [m^2] is the area of the target hit by the beam.

$$R_{thin} = n_{inc}Ndx\sigma. \tag{2.4}$$

Further considerations need to be taken in order to deal with thicker targets. Therein, the probability for a particle to not have undergone interaction a distance x into the material is inversely exponential. This result leads on to Equation 2.5, which represents the probability for a particle to have interacted during x in a thick target material.

$$P(x) = 1 - e^{-N\sigma x}. \tag{2.5}$$

Hence, for a beam with many incoming particles, Equation 2.4 is complemented through Equation 2.5, giving the reaction rate in a thicker target as

$$R_{thick} = n_{inc}(1 - e^{-N\sigma x}). \tag{2.6}$$

2.2 Ion and matter interaction

As ions and matter interact, concepts like fusion, fission, compound formation, direct reactions and spallation are important for the scope of this thesis. Other interactions do also occur and may result in the emission of Cherenkov radiation and bremsstrahlung. However, in excess of all the mentioned reactions, it is far more probable for ions which pass through matter to slow down through inelastic collisions with the electrons of the target material or through elastic scattering with the nuclei.[8]

Before the different kinds of ion and matter interactions are further discussed, a small introduction about notation is of importance. A common way to describe different interactions is given in Equation 2.7. The uppercase letters outside the brackets represents the target atom (A) and the recoil (B). The lowercase letters inside the brackets corresponds to the incoming projectile, (a) and the outgoing ejectile (b).

$$A(a, b)B \tag{2.7}$$

Equation 2.7 can be explained through a simple example. Consider a hydrogen projectile which is aimed at a target material consisting of tritium atoms. After a nuclear reaction, a neutron and a ^{3}He atom are detected. According to Equation 2.7, this reaction can be simplified to the following notation: T(p,n)^{3}He. This notation will be commonly used in this thesis. However, when no confusion arises and since this thesis specifically deals with nuclear reactions for neutron production, this and other reactions will often be simplified to an even shorter notation, a-A, or specifically for this example p-T.

2.2.1 Energy-loss through scattering interactions

In the introduction to this section it was stated that the probability for scattering is much higher than the probability for nuclear reactions. The scattering interactions causes the projectiles to lose energy. Relating to this, two processes were mentioned: inelastic collisions with the electrons of the target material and elastic scattering with the nuclei of the target. In the following part these processes are discussed qualitatively as well as the resulting energy loss.

Of the two scattering processes, the primary contribution to the energy loss occurs through inelastic collisions with the electrons of the target material. The cross section for this interaction is in the order of 10-100 Mbarn [8]. As a comparison, the highest cross section for a fusion reaction in the energy interval of our interest is around 5 barn. Because of the difference in mass between ions and electrons, such collisions will only minimally deflect an ion from its original path.[1]

The process of elastic scattering with nuclei is also probable. In Chapter 2.3, i.e. in the theory section about the slowing down of neutrons, it will become evident that elastic scattering of a particle with nuclei is most effective if it occurs on target materials of similar size. This is also true for ions. Thus, if the masses of the nuclei in the solid material are much larger compared to the projectile, the energy loss through elastic scattering will be small.

The combined and total energy loss is described by the modified Bethe-Bloch formula in Equation 2.8,

$$-\frac{dE}{dx} = 2\pi N_A r_e^2 m_e c^2 \rho \frac{Z_2}{A_2}\frac{Z_1^2}{\beta^2}\left[\ln\left(\frac{2m_e\gamma^2 v_1^2 W_{max}}{I^2}\right) - 2\beta^2 - \delta - 2\frac{C}{Z_2}\right], \tag{2.8}$$

where r_e is the classical electron radius, ρ the density of target, m_e the mass of the electron, N_A Avogadro's number and W_{max} the maximum amount of energy that is possible to transfer in one collision. The parameters denoted with a subscript of 1 pertains to the projectile, while those with the subscript 2 specifies the target material. The parameters related to the subscripts are Z, the atomic number, A, the atomic weight and β, the speed of the projectile (v_1) over the speed of light (c) [8]. I is the mean excitation potential and is considered to be a material constant. It corresponds to the average energy required to excite the atomic electrons of the material.[1]

The density correction, δ, is part of Equation 2.8 because of how the interaction occurs a certain distance away from the path of the projectile. As a result of the polarisation of the encountered atoms, the intensity of the electric field will diminish for electrons further away from the projectile. The effect of such a shielding will cause the interaction, and therefore the stopping power, to be reduced. As the name of the correction might reveal, the effect is greater for more dense materials.[8]

The shell correction, C, is added to compensate for the changes occurring when the velocity of

the projectile is roughly similar or less than that of the bound electrons in the target. If this is the case, the correction is needed because the electron can no longer be viewed as stationary compared to the projectile.[8]

Since the incoming projectiles lose energy and eventually stop, Equation 2.8 forms the basis for the calculation of how far projectiles of different energies penetrate into materials. The distance is referred to as the range and can be calculated through the integration of Equation 2.8 over all the energies of the incoming ion [1]. The approximations needed and tabulated values of the different parameters in Equation 2.8 can be found in [8].

2.2.2 Nuclear reactions

In the introduction to this section, different kinds of nuclear reactions where mentioned as a possible way for ions and matter to interact. These reactions will be further introduced in this subsection. An emphasis will be put on the primary reaction of interest for the scope of this thesis, the fusion reaction. Relevant physical concepts will be discussed in relationship to this reaction.

2.2.2.1 Fusion

The nuclear reaction where lighter nuclei are combined to form heavier nuclei is called fusion. Naturally, fusion relates to energy production since the process is the actual energy source of the sun (through multiple fusion steps). However, as neutrons can be released during a fusion reaction, the process can also be utilised for neutron production. This can be achieved using different types of accelerators, of which a high-yield neutron generator is an example. Such devices can reach a neutron production rate of 10^{12} neutrons/s and have applications in for example homeland security.[10][11]

Generally, a fusion reaction releases energy. The reason of why will be highlighted in the following discussion starting with the topic about the Q-value. It is defined in Equation 2.9 by invoking Einstein's relationship between energy and mass to the difference of the initial mass (m_i) of the reactants and final mass (m_f) of the products. The difference between the masses, if positive, indicates that energy is released when a nucleus is formed. Such a reaction is called exothermic. If $Q < 0$ the reaction is endothermic, i.e. a minimum amount of energy has to be supplied to the system in order for the reaction to be possible. If the increase of the final mass is not compensated, the reaction will not occur.[1][12]

$$Q = (\sum_i m_i - \sum_f m_f)c^2 \tag{2.9}$$

Equation 2.10 defines the binding energy (B) of a nucleus as the energy difference between the individual components of the atom (Z = number of protons, N = number of neutrons, A = mass number) and the atom taken as a whole.[1]

$$B = [Zm(^1H) + Nm_n - m(^AX)]c^2 \tag{2.10}$$

By incorporating Equation 2.10 with Equation 2.9, the Q-value can be identified as the difference between the final binding energy (B_f) of the products and the initial (B_i) of the reactants.[12]

$$Q = (\sum_f B_f - \sum_i B_i)c^2 \tag{2.11}$$

This discussion will inevitably lead on to Figure 2.4, which is a classic representation of the binding energy per nucleon plotted as a function of mass number. For the lighter elements the binding energy per nucleon is lower than the peak value just below 9 MeV/nucleon for the most bound systems. Also noticeable in this region is the positive gradient of the binding energy per nucleon for increasing mass number. Exemptions to this rule do exist because of the quantum mechanical rules concerning the allowed configurations of different nuclei [1]. The opposite phenomena can be seen in the right part of Figure 2.4. For the heavier elements, the binding energy per nucleon has a negative gradient for increasing mass numbers.

By relating the left region of Figure 2.4 to Equation 2.11, the reason of why the fusion reaction releases energy can be understood. As lighter elements are fused, the binding energy per nucleon generally increases. According to Equation 2.11, such an increase of binding energy per nucleon equals a positive Q-value, which in turn indicates that energy is being released as a result of the nuclear reaction. The release of energy is thus a result of the change of mass in the system.

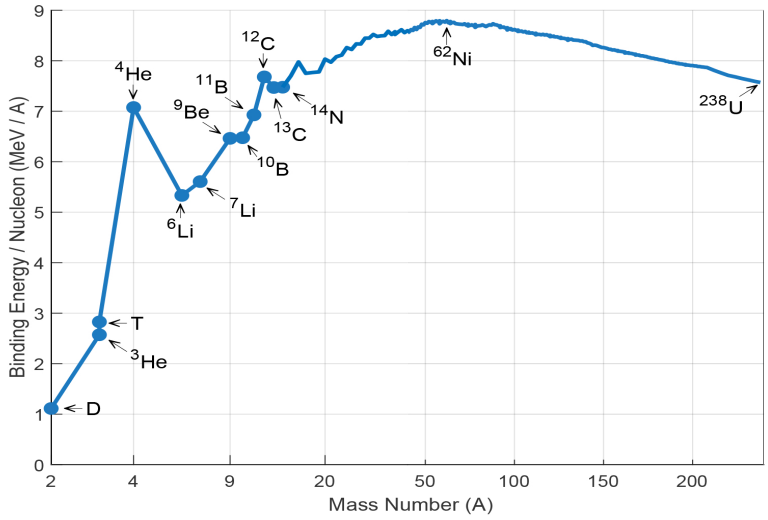

Figure 2.4: The binding energy per nucleon for primarily stable elements. To emphasise the lighter elements, which is of most importance for this thesis, the scale of mass numbers is logarithmic up to A=40. For A>40, the scale is linear. The most bound nucleus, ^{62}Ni, is indicated at the maximum of the parabola. Inspired by [12]. Data from [13].

2.2.2.1.1 Threshold Energy and Coulomb Barrier

An endothermic reaction is possible if a certain amount of energy is supplied to the system. It was previously stated that this is because of the necessity to compensate for the increase in mass of the final state. The minimum required energy is defined as the threshold energy (E_{th}). The threshold energy is not equal to the Q-value because of momentum conservation. In the laboratory frame of reference, the threshold energy is given according to Equation 2.12, where m_a represents the mass of the incoming projectile and Q is given by Equation 2.9 or 2.11.[1][12]

$$E_{th} = -Q\frac{\sum m_f}{\sum m_f - m_a} \tag{2.12}$$

Exothermic reactions are not limited by the threshold energy. However, since fusion only is possible if two nuclei are brought into close proximity, the problem of electrostatic repulsion between like charges is present [1]. The repulsive force (F_{Col}), or Coulomb repulsion, between two charges is

$$F_{Col} = \frac{1}{4\pi\epsilon_0}\frac{q_a q_A}{\mathbf{r}^2}, \tag{2.13}$$

where q_a and q_A are the charges of the respective nuclei, ϵ_0 the permittivity of free space and $\mathbf{r}$ the distance between the nuclei. Equation 2.13 gives that the force is inversely proportional to the square of the distance between the nuclei.[14]

Because of the repulsive nature of the Coulomb force (for nuclei of the same charge), a supply of energy is required to bring the nuclei together. If the radii of the nuclei are r_a and r_A, the required energy, or work, to bring a distant nucleus closer to a stationary nucleus ($\mathbf{r} \geq r_a + r_A$), can be found by integrating Equation 2.13 [14]. The resulting potential energy is

$$V = \frac{1}{4\pi\epsilon_0}\frac{q_a q_A}{\mathbf{r}}. \tag{2.14}$$

The Coulomb barrier (V_{Col}) is defined as being the potential energy at the point of contact between the two nuclei [14]. It is given from Equation 2.14 as

$$V_{Col} = \frac{1}{4\pi\epsilon_0}\frac{q_a q_A}{r_a + r_A}. \tag{2.15}$$

Figure 2.5 shows an outline of the potential energy of a nucleus. The Coulomb barrier is indicated at a distance r_N from the centre of the nucleus. Classically, the barrier translates to the minimum kinetic energy an incoming particle would have to have in order for the nuclear distributions of the projectile and the target to begin to overlap. For such a case, a projectile with too low energy to overcome the Coulomb barrier would not be able to participate in fusion. However, as indicated in Figure 2.5, the barrier is finite and proportional to the inverse of $\mathbf{r}$ at distances beyond the Coulomb barrier. Therefore, because of the concept of tunneling from quantum mechanics, even projectiles with lower energy than the Coulomb barrier have a probability to participate in fusion.[12]

2.2.2.1.2 The strong force and formation of a compound nucleus

The strong force is negligible at length scales beyond the Coulomb barrier. However, in the region where the nuclear distributions of the projectile and the target begin to overlap, the strong force overcomes the Coulomb repulsion [14]. At this distance, the strong force is attractive, thus forming the potential well (V_0)out lined in Figure 2.5. At an even smaller distance, $r < 0.4$ fm, the nuclear force is repulsive, keeping the nucleons at a certain distance.[15]

Because of the attractive characteristics of the strong force, the overlapping nuclear distribution of the projectile and the target can form a compound state. A compound state is a concept originating with Niels Bohr. It results in a lifetime greater than the average time the projectile

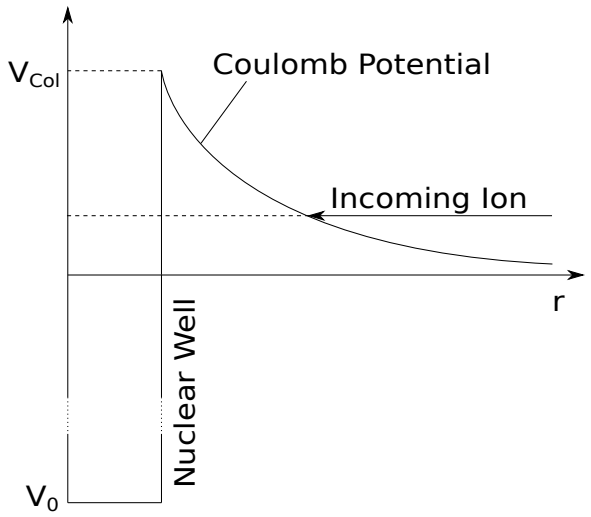

Figure 2.5: Illustration of the Coulomb potential and nuclear square well. Inspired by [12].

would need to pass through the nucleus of the target [15][16][17]. When a compound state is formed, the energy of the incoming particle is distributed almost uniformly between the combined nucleons of the projectile and the target through a series of collisions [1]. The evaporation of a nucleon is improbable until the energy, through random collisions, happens to be focused in one degree of freedom [17]. The particle ejected from the compound state is not needed to be identical with the incoming particle.

Equation 2.16 is a summary of a nuclear reaction using similar parameters as in Equation 2.7. As can be seen, the formation of a compound state (C^*), as well as the deexcitation thereof, is indicated. The final product(s) will be the result of the governing laws of conservation, which control both the formation of the compound state and the deexcitation thereof.[5]

$$a + A \longrightarrow C^* \longrightarrow b + B. \tag{2.16}$$

The formation of a compound nucleus is not the only entry path for a fusion reaction. An alternative is direct reactions, where the interaction between the projectile and the target is mainly limited to a single nucleon on the surface of the target nucleus [1]. The concept of direct reactions involves different processes, including both stripping, pickup, break-up and knock-out reactions.[18] In comparison with compound formation, the characteristics of direct reactions involves faster reactions (occurring in the order of 10^{-22} s) and a clearer anisotropy of the outgoing particles.[1]

Generally, the compound formation is of greater importance than direct reactions in the energy domain of interest in this thesis ($\leq$3 MeV). However, some reactions have the possibility to occur both through compound formation and direct reaction.[1]

2.2.2.1.3 Radioisotope sources

Beyond the use of accelerators for obtaining neutrons from fusion reactions, radioisotope sources are also in use. Radioisotope sources produce neutrons through the (α,n)-reaction. Since these sources are based on induced nuclear reactions, the emitter is commonly mixed with the tar-

get material. Radioisotope sources are advantageous because of their size which makes them portable. For a higher neutron flux, it is necessary to have larger quantities of the particular element. Using for example americium (Am) as the alpha emitter, it is possible to obtain fluxes of $10^6 - 10^8$ n/(s·g).[19]

The Source Testing Facility in Lund uses two different radioisotope sources consisting of plutonium or americium (the α-emitter) together with a surrounding powder of ^{9}Be. The ^{9}Be(α,n)^{12}C-reaction have a positive Q-value of 5.71 MeV and forms the compound state of ^{13}C* during the process. Together with evaporation of neutrons, the exit channels from the compound nucleus involves various states of ^{12}C, as well as the possibility of α-emission.[8][11]

2.2.2.2 Fission

In the previous discussion around Figure 2.4, it was stated that energy will be released as lighter elements undergo fusion because of how the masses and binding energy of the nuclei change. From the right region of the same figure, a similar argument can be made from the perspective of splitting heavier nuclei into lighter fragments. This process is called fission and results in the release of lighter elements as well as neutrons. The energy released in the fission process is close to the energy of the Coulomb barrier of the initial nuclei.[1]

The process of fission is controlled in reactors, where around 2.5 neutrons per fissioned ^{235}U is produced on average. Of these, one neutron is required to continue the fission process [20]. Using this technology, high continual fluxes in the order of 10^{15} neutrons/cm^2/s is obtained in for example the Institut Laue-Langevin in France [21].

Beyond the use of controlled fission in reactors, sources with spontaneous fission are also used for neutron production. This concept involves short-lived elements like ^{252}Cf. The rate of neutron production will vary with the available amount of the specific source. However, sources exist which can produce in the order of 10^9 neutrons/s.[11][22]

2.2.2.3 Spallation

Another highly relevant way to produce neutrons is through spallation. This is the process that will be used at the ESS facility in Lund. Spallation is possible when an energetic small nucleus hits a target consisting of medium to heavy nuclei. At ESS, neutrons will be produced using proton projectiles of 2 GeV and a tungsten target.[23] Such high energies are beneficial as the number of neutrons per projectile increases with the energy of the incident particle (to a certain limit) [24]. Even though favourable at higher energies, the process is still possible using projectiles with energies from around 10 MeV [5]. As the accelerator of LIBAF is limited to around 3 MeV, the accelerated ions will be of too low energy to be of use for spallation. Thus, the topic of spallation is merely of academic interest for this thesis.

2.2.3 Reaction kinematics

Related to the topic of nuclear reactions using accelerators, is the kinematics of a reaction. For the experimental part of this thesis, it is of importance to know the energy of the outgoing neutrons (E_n). This energy is stated in Equation 2.17. The background of the physics involved is explained in [1]. The result depends on the angle of detection (θ), the mass and energy of

the incoming ion (m_a, E_a), the mass of the outgoing particles (m_n, m_D) and the Q-value of the reaction.

$$E_n^2 = \frac{(m_a m_n E_a)^{1/2}\cos\theta \pm [m_a m_n E_a \cos^2\theta + (m_D + m_n)(m_D Q + (m_D - m_a)E_a)]^{1/2}}{(m_D + m_n)} \tag{2.17}$$

2.3 Moderation

In Equation 2.17 it was shown that the energy of the produced neutrons will depend on the chosen fusion reaction, the kinetic energy of the ions at the point of interaction and the angle of emission. It is often of interest to slow down the obtained neutrons, thus decreasing their energies to levels suitable for different experiments. The process of reducing the energy of neutrons is denoted moderation.

It was previously mentioned that ions primary lose energy in matter through inelastic collisions with the electrons of the target material. Neutrons, however, lack charge and will not interact with electrons or protons through the Coulomb interaction. Because of the lack of Coulomb repulsion, neutrons are able to approach a target nucleus close enough for the strong force to dominate the interaction.[8]

The results of the interaction between neutrons and matter are manifested in a variety of ways: elastic and inelastic scattering, neutron capture, fission and high energy hadron shower production [8]. For the scope of this section, it is primarily the first three interactions that are of interest. Of these, specifically elastic and inelastic scattering are related to the process of moderation. These two topics will thus be introduced in the following. The phenomenon of neutron capture is a concern when choosing moderator materials. This topic will therefore be introduced in the final part of this section.

2.3.1 Elastic Scattering

The following section about elastic scattering is based mainly on [25]. In an elastic scattering event, the nucleus of the target remains in the ground state after the scattering. Using the same notation as before, elastic scattering can be described as A(n,n)A. Figure 2.6 illustrates the elastic scattering of a neutron on a nucleus in both the laboratory system (L) and the centre of mass system (CM). The two different coordinate systems describe the process of elastic scattering from two different point of views. The L-system proceeds from the perspective of a coordinate system in rest relative to a spectator. In contrast, the CM-system is a coordinate system in motion, following the centre of mass of the system.

Various velocity components and scattering angles are indicated in Figure 2.6. In the L-system, a neutron with a velocity of v_{n0} collides with a nucleus approximated as being at rest initially. Such an approximation is not valid around thermal energies, since the speeds of the neutron and the nucleus then are relatively similar [1]. The velocity of the neutron after the collision is v_{n1} and its scattering angle θ. The transformation of the velocity of the neutron from the L-system to the CM-system is given in Equation 2.18. Also of importance for the scope of this thesis is the velocity of the CM-system given in Equation 2.19. Since the velocity of the nucleus is zero in the L-system, Equation 2.19 also represents the velocity of the nucleus in the CM-system. The masses of the nuclei have been normalised to the mass of the neutron, giving that the mass of the particle corresponds to the atomic mass number (A) [5][8].

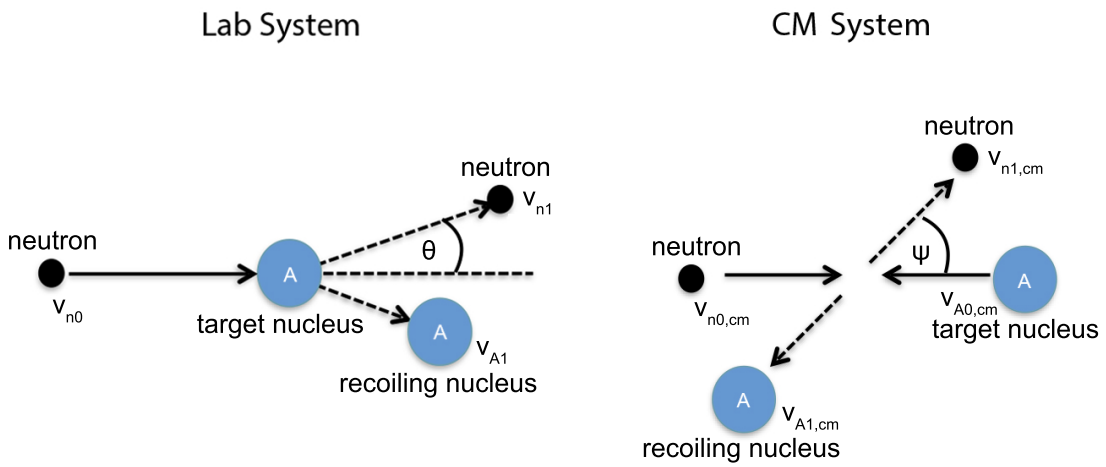

Figure 2.6: Illustration of the elastic scattering of a neutron on a target nucleus, A. The scattering event is described both in the laboratory system (left) and the centre of mass system (right).[26]

$$v_{n0,cm} = \frac{A}{A+1} v_{n0} \tag{2.18}$$

$$v_{cm} = \frac{1}{A+1} v_{n0}. \tag{2.19}$$

The benefit of transforming the parameters of the L-system to the CM-system can be seen from analysing the precollision parameters. If the momentum of the particles before collision is considered in the CM-system, it is evident that the total momentum in this system equals zero. Since elastic scattering is considered, the total momentum will be conserved after the collision and, as a result, also the speed. After the collision, the trajectory of the neutron changes with an angle ψ in the CM-system.[8][25]

Figure 2.7 indicates the summary of two post-collision velocity vectors pertaining to the CM-system. The horizontal vector corresponds to the velocity of the moving coordinate system (v_{cm}) and the far right vector to the velocity of the neutron. As is indicated, the addition of these vectors gives the post-impact velocity of the neutron in the L-system, (v_{n1}). By utilising the law of cosines, this velocity can be stated as in Equation 2.20,

$$v_{n1}^2 = \left(\frac{v_{n0}}{A+1}\right)^2 + \left(\frac{v_{n0}A}{A+1}\right)^2 + 2\frac{v_{n0}}{A+1}\frac{v_{n0}A}{A+1} cos(\psi), \tag{2.20}$$

where the angle ψ is related to θ according to Equation 2.21 [8].

$$\cos\theta = \frac{A\cos\psi + 1}{\sqrt{A^2 + 1 + 2A\cos\psi}} \tag{2.21}$$

By utilising the relationship between kinetic energy and velocity, Equation 2.22 gives the relative

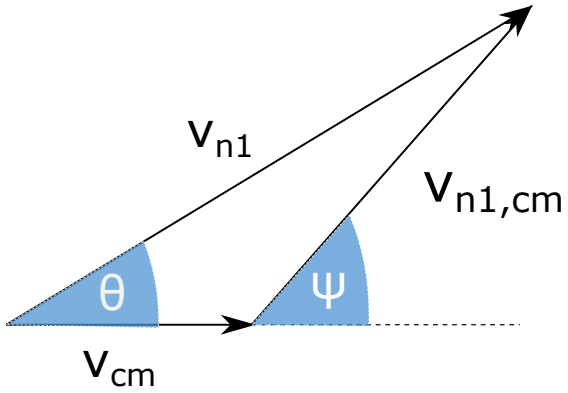

Figure 2.7: Schematic illustration of the summation of two velocity vectors from the CM-system, that of the moving coordinate system and that of the scattered neutron. The notation is related to Figure 2.6. Inspired by [25].

energy of the neutron as the fraction between its post-collision kinetic energy (E_{n1}) and its original energy (E_{n0}).

$$\frac{E_{n1}}{E_{n0}} = \frac{A^2 + 1 + 2A\cos(\psi)}{(A+1)^2}. \tag{2.22}$$

While ψ=π, i.e. when the neutron is backscattered in the CM-system, the energy of the scattered neutron is at a minimum. The corresponding angle in the L-system can be found from Equation 2.21. The largest value occurs for ψ=0, i.e. for forward scattering. Thus, the range of the neutron energy after scattering is:

$$\left(\frac{A-1}{A+1}\right)^2 E_{n0} < E < E_{n0}. \tag{2.23}$$

Equation 2.23 indicates that the target nucleus will have a profound effect on the range of the post-collision energy of the neutron. Evidently, moderation will be most effective if lighter nuclei are used. Hydrogen (A=1), as an example, has the potential of completely stopping the incoming neutron in a single scattering event. The result is intuitive if exemplified through an analogy in the macro world. Consider a table tennis ball which is shot onto a billiard ball. Naturally, the recoil of the much heavier billiard ball will be very small, resulting in that the table tennis ball will preserve most of its original energy, even when its direction is changed.

2.3.2 Inelastic scattering

Inelastic scattering is the phenomena where the target nucleus is left in an excited state after the scattering event. In the shorted notation, inelastic scattering is written A(n,n)A*, where the star indicates that the initial nucleus has entered an excited state. Since a certain amount of energy is needed to excite a nucleus, E_{exc}, inelastic scattering is only possible if the kinetic energy of the neutron is above a certain threshold. The relative kinetic energy of the neutron after scattering can be derived in a similar way as Equation 2.22. The result is stated in Equation 2.24,

$$\frac{E_{n1}}{E_{n0}} = \frac{\gamma^2 + 1 + 2\gamma\cos(\psi)}{(A+1)^2}, \tag{2.24}$$

where $\gamma = (A\sqrt{1-(A+1/A)E_{exc}/E_{n0}})$. If the excitation energy is zero, Equation 2.24 is reduced to the case of elastic scattering in Equation 2.22.[5]

From the previously given analogy about elastic scattering, as well as from Equation 2.23, it is evident that neutrons which are elastically scattered in heavier material only lose a small fraction of the initial energy in each collision. Hence, inelastic scattering will be of greater importance in moderators consisting of heavier elements [5].

2.3.3 Lethargy and the required average number of collisions

With the knowledge of the energy of the neutron before and after the collision, it is possible to calculate the average number of collisions necessary to slow down a neutron to a certain energy. To find the average number of collisions needed for moderation, the concept of lethargy change (u) is utilised. If only elastic scattering is taken into consideration, the concept is defined in Equation 2.25 as the difference of the logarithms of the pre- and post-collision energy. Evidently, the gain in lethargy is increased as a function of the reduced energy of the neutron.[8]

$$u(\theta) = \ln\left(\frac{E_0}{E_1}\right) = \ln\left(\frac{(A+1)^2}{A^2+1+2A\cos(\psi)}\right) \tag{2.25}$$

The average lethargy change for one collision, ξ, is of relevance for the further analysis. The derivation is found in [8] or [25]. Here, the result is stated in Equation 2.26. The equation indicates that the average lethargy change for one collision is a constant which only depends on the mass number of the target nuclei, not on the energy of the neutron.

$$\xi = 1 + \frac{(A-1)^2}{2A}\ln\left(\frac{A-1}{A+1}\right) \tag{2.26}$$

From the results in Equations 2.25 and 2.26, the average number of collisions (n) needed to reduce the initial energy of the neutron (E_0) to a lower energy (E_1), can be found through Equation 2.27. This equation is of importance for the further evaluation in Chapter 3.3.

$$n = \frac{u}{\xi} = \frac{\ln(\frac{E_0}{E_1})}{\xi} \tag{2.27}$$

2.3.4 The non-relativistic kinematics

The kinematics introduced above is written in non-relativistic formulae. The reason for this is the physical limitation of the accelerator at LIBAF. The maximum projectile energy is 3 MeV, resulting in maximum neutron energies of below 20 MeV. Compared to the rest mass of a neutron at 939.56 MeV, the neutron energies considered in this thesis are only a couple of percent. According to [9], such an approximation is sufficient for the considered neutron energies.

2.3.5 Neutron capture

Beyond elastic or inelastic scattering, two other processes are worth mentioning for the scope of this thesis: radiative neutron capture and the emission of a charged particle (or fission) resulting from the capture of a neutron. Based on [8], the phenomena of radiative neutron capture will be briefly described in the following, while the discussion about neutron capture followed by emission of a charged particle is saved until Chapter 2.4.1.

Radiative neutron capture involves two processes, absorption and relaxation. Absorption is the process where an incident neutron is absorbed by a nucleus. The contribution of energy from the neutron leaves the nucleus in an excited state. The process of relaxation occurs as the excited nucleus releases gamma quanta and subsequently returns to its ground state. Hence, according to the previously given notation, radiative neutron capture can be described as A(n,γ)B.

The cross section for radiative capture is typically of greater importance for thermal neutrons than fast neutrons. This is reflected in the cross section which, if resonances are disregarded, decreases proportional to the energy. The relatively high cross section for thermal neutron capture of hydrogen will be highlighted further in Chapter 3.3, suggesting that hydrogen rich materials need special attention if to be used as a moderator.

2.4 Neutron Detection

For the purpose of detecting neutrons, different types of detectors exist. Regardless of whether the detection occurs in a gas, a semiconductor or a scintillator material, the process will be based on nuclear scattering or nuclear reactions. This is due to the neutron having no electrical charge [1]. During the experimental part of this thesis, two detectors using scintillator materials were used. Hence, both the gas and the semiconductor detector will not be discussed further. Of the two scintillator detectors, one is to be used for thermal neutrons, while the other is aimed at detecting fast neutrons. Even though the detection process for the two different neutron velocities is somewhat different, the general design characteristics of the scintillator detectors are similar. A schematic illustration of this design is shown in Figure 2.8, which highlights three different parts: the photomultiplier tube (PMT), the light guide and the scintillator. The PMT and the scintillator will be discussed briefly in the following, before an introduction to the different detection processes of thermal and fast neutrons are given. A more thorough treatment is given in [8].

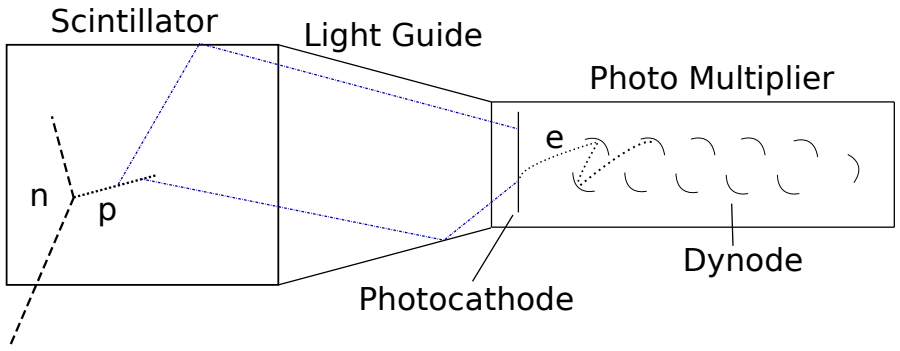

Figure 2.8: Illustration of a scintillator detector. Inspired by [26].

The scintillator consists of a material that emits photons as a result of interaction with particles (or photons). This is illustrated in the figure where a neutron (n) has scattered on a hydrogen atom (p), causing scintillations as the recoiled atom travels in the material. For this purpose a wide selection of materials with different characteristics can be used, from organic scintillators to inorganic crystals, gaseous scintillators or glass materials. Since the detection of a particle is based on the emittance of photons, the material used must be transparent to the emitted wavelengths. The plastic scintillators used during the experimental part of this thesis is a subgroup of organic scintillator materials, consisting of "*aromatic hydrocarbon compounds containing linked or condensed benzene-ring structures*"[8]. The scintillations in such a material result from transitions of excited free valence electrons. Ideally, the deposited energy would be directly proportional to the emitted light.[8]

In the PMT, the scintillations are converted into an electrical current using a photocathode with an efficiency of up to 30%. The conversion process results in a weak current and is thus in need of amplification. This is achieved in the PMT through a chain of dynodes, each with an increasing potential. As the original electron (e) from the photocathode (pertaining to one certain deexcitation in the scintillator) collides with the first dynode, more electrons are released and in turn accelerated towards the next dynode. Thus, through each collision with a dynode, the number of electrons is increased until an analysable current is obtained.[8]

Beyond this brief introduction to the scintillator and the PMT, it is of importance to mention some factors that affect the data when an experiment is carried out. Figure 2.9 shows the ideal proton recoil spectrum from the detection of monoenergetic neutrons (solid line), as well as the effect thereupon from the nonlinearity of the scintillator and the detector resolution.

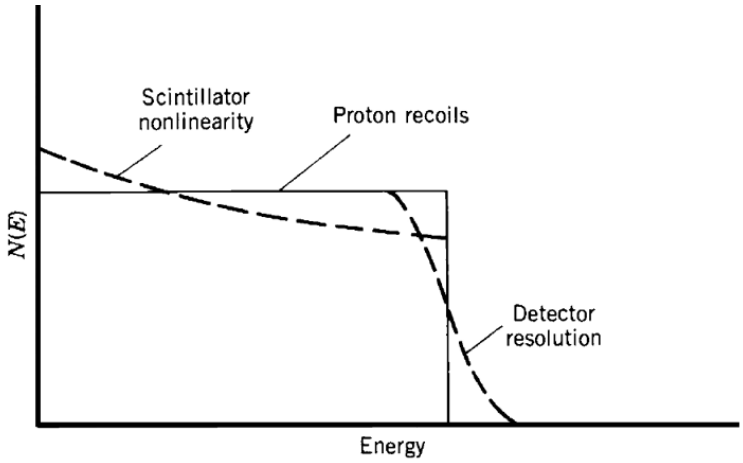

Figure 2.9: The ideal and the distorted spectrum of the recoiled protons after scattering by monoenergetic neutrons.[1]

The effect of nonlinearity is related to the scintillator. It was previously mentioned that the light response to the deposited energy ideally is linear. However, this linearity fails at lower particle energies, especially for particles heavier than the electron [8]. The result of the nonlinearity is a conflation of the spectrum at lower energies.

In the PMT, both the photoemission of the initial electron and the secondary emissions occurring in the dynodes, are linked to a certain probability. Thus, the conversion to current, as well as its amplification, result in gain variations known as statistical noise [8]. The combined statistical

nature of the detection event in both the scintillator and the PMT, results in a limitation of the detector resolution.

2.4.1 Thermal Neutron Detection

In the following sections the detection process of both thermal and fast neutrons will be explained separately, starting with the detection of thermal neutrons using scintillators.

Thermal neutron detection is based on nuclear reactions, as slow neutrons are prone to be captured by certain isotopes. To detect the incoming neutrons, isotopes like ^{3}He, ^{6}Li and ^{10}B can be used. The following discussion will be limited to ^{10}B-absorption, since this is the material used in the scintillator during the experiment in this report. The absorption reaction ^{10}B(n,α) is highlighted in Equation 2.28.

$$ {}^{10}_{5}B + n \longrightarrow \begin{cases} {}^{7}_{3}Li + \alpha & \text{(Q=2.792 MeV)} \\ {}^{7}_{3}Li^{*} + \alpha & \text{(Q=2.310 MeV)} \end{cases} \tag{2.28} $$

The exit channel of the reaction in Equation 2.28 has two branches. The probability of accessing the excited state of ^{7}Li is 96 % [9]. A 478 keV photon is emitted as a result of the deexcitation to the ground state [1][27]. If the incident neutron is slow (in the range of eV or keV), the emitted α-particle will have a kinetic energy of 1.47 MeV and the ^{7}Li-nucleus 0.84 MeV [1]. Both particles are thereafter detected through their generation of scintillations in the plastic material. The charged particles do have a relatively small range in a plastic material ($<$10 μm) [28]. Therefore, and since the released energy of the reaction always is approximately similar (for slow neutrons), the resulting spectrum has a characteristic peak around a certain energy.

2.4.2 Fast Neutron Detection

Rather than being detected through nuclear reactions, fast neutrons are commonly "seen" as a result of the detection of the recoil from the elastic scattering between the neutron and the plastic material. In Chapter 2.3.1, the moderation of neutrons was discussed. From Equation 2.22 it was seen that if hydrogen atoms were considered as the moderator material, the energy of the scattered neutron after one scattering event would be between zero and the original energy of the neutron. Accordingly, the resulting energy of the recoil would vary between the original energy of the incoming neutron and zero. For a general moderator material, the maximum obtainable energy of the recoil is given in Equation 2.29 [1].

$$ E_{R,max} = E_{n0}\frac{4A}{(A+1)^2} \tag{2.29} $$

Due to the possibility of total energy absorption, as well as the high cross section for elastic scattering, hydrogen rich materials like plastics are beneficial to use as the scintillator material. As was previously mentioned, a plastic is the material of choice in the scintillator used for fast neutron detection in the experimental part. This is discussed further in Chapter 4.1. The function of the plastic material is two-fold, as it both acts as a target material for the scattering of the incoming neutrons and as a scintillator for the recoiled nucleus. When one neutron scatters multiple times in the scintillator, the scattering is fast enough for the detector to interpret the combined scintillations as corresponding to a higher energy.

2.4.3 Coincidence measurement

Coincidence measurements can be used in nuclear physics to determine if different reactions are related and as a means to reduce the background of unwanted radiation [1]. The measurement is based on that a detected particle generates a gate with a certain time width. A coincidence event is found if a second particle is detected within the set gate. The certainty of a detected coincidence is a function of the chosen time window. If the width of the gate is limited, neutrons that travel a longer route and scatter and lose energy can be disregarded, thus lowering the background radiation. Moreover, once the energy of the detected ion is known, the energy of the detected neutron can be calculated because of the fixed kinematics of a two-body reaction. A circuit diagram and a possible experimental setup for a coincidence measurement will be demonstrated in Chapter 4.

2.4.4 Time-Of-Flight

At LIBAF, it will be possible to produce pulsed neutrons using either a deflector or a rotating wheel with multiple targets. With such a solution, it is possible to calculate the energy of the detected neutrons using the time-of-flight method (ToF). The method is based on the known time signature of the detected neutrons and the known flight path between the point of creation and the point of detection. As an alternative to a pulsed neutron source, a chopper could be used together with the ToF-method. A chopper blocks the flight path of neutrons to the detector until, at well-defined times, the windows of the rotating device let particles pass.

Chapter 3

Theoretical Evaluation

This chapter deals with the theoretical evaluation of the upcoming neutron experimental station. Four aspects of this experimental station are included: appropriate target materials, approximations of the possible number of neutrons obtained from different reactions, the characteristics of moderators and which materials to use as a beam dump for the deflected beam.

3.1 Evaluation of Target Materials

The reactions that will be characterised are the result of accelerated ions of an isotope of hydrogen (protons or deuterons) bombarded onto targets of different materials. Table 3.1 contains a selection of possible nuclear reactions which could be used in order to produce neutrons. The last projectile in the table (α) and its corresponding reaction is included mainly for historical reasons. This was the reaction used by James Chadwick to discover the neutron [29].

Table 3.1: Various accelerator based neutron sources.[29][30]

Projectile	Reactions		
Proton	T(p,n)^{3}He	^{9}Be(p,n)^{9}B	^{11}B(p,n)^{11}C
	^{6}Li(p,n)^{6}Be	^{10}Be(p,n)^{10}B	^{12}C(p,n)^{12}N
	^{7}Li(p,n)^{7}Be	^{10}B(p,n)^{10}C	^{14}C(p,n)^{14}N
Deuteron	D(d,n)^{3}He	^{6}Li(d,n)^{7}Be	^{9}Be(d,n)^{10}B
	T(d,n)^{4}He	^{7}Li(d,n)^{8}Be	
Triton	T(t,2n)α	^{3}He(t,np)α	
Alpha	^{9}Be(α,n)^{12}C		

Henceforth, only part of the vast amount of possible accelerator neutron sources will be considered, with the focus of the evaluation being on low Z materials. Reactions which are directly disqualified from further evaluation are all reactions involving ^{3}He as projectile or target because of its limited natural supply. ^{3}He originates from the decay of tritium and is separated as part of the "*tritium cleaning process*" of nuclear weapons. However, as the number of nuclear weapons

has been reduced, along with an increased use of ^{3}He in for example homeland security and science laboratories, its current production fall short of the demand.[14][31]

The second group of reactions which also is directly disregarded for further evaluation is reactions involving tritium projectiles. In order to use such projectiles in the accelerator at LIBAF, proper monitoring and licenses would need to be in place. Reactions involving tritium as a target material will still be considered, even though the use thereof would entail to a more careful planning because of its radioactive characteristics.

3.2 Fusion cross sections for neutron production

To calculate the neutron production rate from Equation 2.6, special attention needs to be given to the cross section. As was previously discussed in Chapter 2.1, the fusion cross section varies with the energy of the incoming particle. For many reactions, measurements of the values of the cross section as a function of energy can be found in the database of the Experimental Nuclear Reaction Data (EXFOR) [32]. With the discussion in the previous section in mind, Figure 3.1 presents the cross sections of a selection of the reactions to be further evaluated as a potential source for the production of neutrons at LIBAF. The given cross sections therein correspond to reactions which produce neutrons. Values of the cross section are, for most cases, given up to the highest working range of the accelerator at LIBAF. The given reactions are d-D, p-T, d-T, d-^{6}Li, p-^{7}Li, d-^{7}Li, p-^{9}Be, d-^{9}Be, d-^{10}B, d-^{11}B, d-^{12}C and d-^{13}C. The cross sections of the reactions which are induced with protons are marked with a dashed line, while a solid line is used for those pertaining to deuterons. Pay attention to the cross section of the d-T-reaction which has been scaled down with a factor of 5 in order to highlight the cross sections of the other reactions. The peak value of the cross section of the d-T reaction is thus in reality around 5 barn. Also note that the cross sections given for d-^{7}Li and d-^{11}B are marked with '+' signs on the solid line. This is to indicate the scarce data sets of the cross sections being 1 MeV between each value. The values for these reactions originate from both [32] and [33].

The cross sections in Figure 3.1 vary highly with the incoming projectile energy. For the p-T-, p-^{7}Li- and p-^{9}Be-reactions, the value of the cross section is 0 barn up to a certain projectile energy, at which point the threshold energy of the reaction is overcome. Above the threshold, their cross sectional values increase with increasing energy. A similar increase in cross section with the projectile energy is also visible for most deuteron induced reactions. For the given energy range, the cross sections of these reactions are relatively constant once their respective peak value has been reached. If the projectile energy is increased to energies that are beyond the scope of this thesis (>3 MeV), the cross sections of all the given reactions will eventually decrease.

The character of the cross section for the d-T- and p-^{7}Li-reaction are in sharp contrast to the other reactions. Both reactions clearly display characteristic peaks around two different energies of the incoming particles. The peaks correspond to resonant reactions. In Chapter 2.1, it was mentioned that resonances are possible if the energy of the incoming projectiles broadly matches the energy needed to excite the formed compound nucleus to a certain energy level. Reactions with similar clear resonances could prove to be beneficial because of the possibility of obtaining a more uniform neutron spectrum from the source.

The cross sections of Figure 3.1 give an indication that, depending on which energy is used in the accelerator, different reactions could be chosen. Since the accelerator of LIBAF is running smoother at 2.5 MeV than 3 MeV, this is the projectile energy that will constitute the basis for

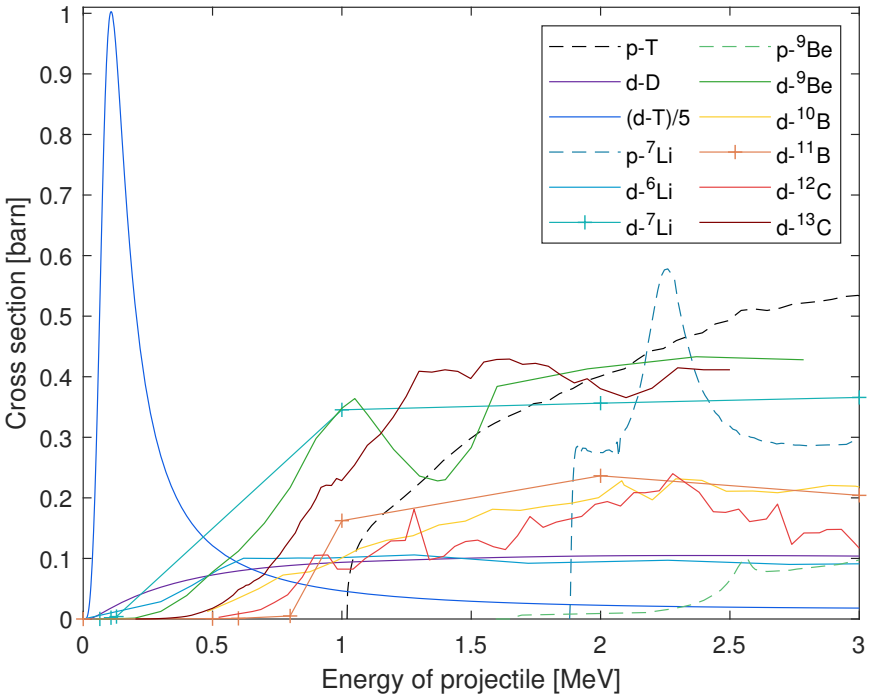

Figure 3.1: Multiple cross sections for neutron production as a function of projectile energy. The proton induced reactions is marked with a dashed line, while the reactions induced by deuterons are denoted with a solid line. Observe that the cross section of the d-T-reaction has been scaled down a factor 5.[32][33][34]

the further evaluation. However, as was shown in Equation 2.6, it is not only the cross section which is an important factor in calculating the number of produced neutrons. Apart from the current, two other factors of great importance are the density of target atoms and the range of the ions in the material. To be able to draw approximative conclusions from such data, Table 3.2 is given. The table includes reaction and target specific data on the integrated cross section, density of the target material, number of specific target atoms, range and the surface density of specific target atoms. The approximation of the number of atoms per cubic centimetre as well as the calculated ranges for 2.5 MeV projectiles were found using SRIM [28]. SRIM is a useful software to calculate both the stopping power as well as the range of ions in different materials through a quantum mechanical approach. For the endothermic reactions, the stated range is lower than what would be expected for a projectile of 2.5 MeV, the reason being that beyond the stated range, most ions have lost a significant amount of energy which disqualifies them from further participating in neutron production through fusion (again, because of the endothermic nature of the reaction). The fifth column corresponds to the specific number density of target atoms. For the titanium tritide, this value was calculated with the assumption of having 1.5 tritium atoms per titanium atom [35]. For the targets of lithium fluoride, boron and carbon, the number density was calculated with respect to the isotopic abundance related to the specific target atoms.

From the given values of the integrated cross section and the surface density of targets in Table 3.2, a coarse comparison between targets can be made in order to approximate their potential

Table 3.2: The integrated cross sections for the reactions from Figure 3.1, as well as the density of the target material (ρ), the specific target atom number density (N_A), the range and the surfwace density (N_A ·Range). The stated range corresponds approximately to the length an ion travels before losing too much energy to be able to participate in a fusion reaction.[28][35][36]

	σ_{int}	Target	ρ	N_A	Range	N_A·Range
d-D	2.2E5	CD_2	1.06	8E22	66.37	5.3E20
p-T	5.0E5	Ti_2T_3	3.8	6.5E22	35.44	2.1E20
d-T	1.3E6	Ti_2T_3	3.8	6.5E22	32.96	2.2E20
d-^{6}Li	2.1E5	LiF	2.6	4.76E21	36.44	1.7E19
p-^{7}Li	2.3E5	LiF	2.6	5.6E22	19.44	1.1E20
d-^{7}Li	6.9E5	LiF	2.6	5.6E22	36.44	2.0E20
p-^{9}Be	1.4E4	Be	1.848	1.23E23	31.66	3.9E20
d-^{9}Be	6.6E5	Be	1.848	1.23E23	45.35	5.6E20
d-^{10}B	3E5	B	2.35	2.61E22	36.06	9.4E19
d-^{11}B	3E5	B	2.35	1.05E23	36.06	3.8E20
d-^{12}C	9.5E4	C	2.253	1.12E23	35.21	3.9E20
d-^{13}C	6.4E5	C	2.253	1.21E21	35.21	4.3E18
	[barn]		[g/cm^3]	[targets/cm^3]	[μm]	[targets/cm^2]

in producing neutrons. From the perspective of the integrated cross section, it is especially two σ_{int} that are distinguishable from the others. The integrated cross section related to p-^{9}Be is a factor 15-100 less compared to most other targets. The contrary applies for the cross section of d-T, having an integrated cross section which is a factor 2-100 higher than the values of most other targets. The low integrated cross section of the p-^{9}Be-reaction leads us to suspect that this reaction is not a relevant alternative as a future source for neutron production at LIBAF. By relating the integrated cross sections to the surface density in the last column of Table 3.2, it is seen that none of the included reactions and targets display any particular high surface density compared to the others. Thus, the low cross section of the p-^{9}Be-reaction is also thought of as not being a practicable alternative. Additionally, the surface density of the ^{13}C-target is remarkably low, between a factor 25-125 lower than most other target materials. When this is compared to the value of its integrated cross section, even though relatively high, this reaction is also put on the list of targets which are suspected of resulting in a too low flux of neutrons. A similar argument applies for d-^{6}Li.

3.2.1 Calculations of the neutron yield

To confirm the initial suspicions drawn from Table 3.1, as well as finding a broader basis for deciding upon which targets to be further evaluated, the possible number of produced neutrons were calculated with support from Equation 2.6 for each reaction. The values for the thicknesses of the targets, corresponding to the range of the ions, and the number density of target atoms were taken from Table 3.2. The small straggling, or deviation, from the original path of an ion, was disregarded for the reason mentioned in Chapter 2.2.1, i.e. because of the smaller mass of the projectile compared to the target atoms. For the lower-A-materials it is not a perfect approximation, this is however overlooked in the following analysis.

The calculations of the yield of neutrons were made through an algorithm which looped over the relevant energy interval. For this purpose, some approximations were made. Firstly, the energy loss of the ion was approximated as being linear. Thus, the total possible range of an ion was divided with the total energy available for the reaction, giving a constant thickness of the segments which were to be integrated. For 2.5 MeV ions, the resulting segments were mostly in the order of a few nm. Thereafter, the cross sections needed were interpolated in MatLab using *spline*. In some cases, the obtained cross sections reported multiple values for a certain ion energy. In order to be able to use spline, the mean average of the multiple values were taken and used as the cross section for that specific energy. If the interpolation resulted in negative values of the cross section, these were put to zero.

The algorithm which was used to calculate an approximation of the number of neutrons produced is presented as a flow chart in Figure 3.2. Firstly, a value for the cross section at the relevant projectile energy was found. This value, and the values obtained from Table 3.2, were used to calculate the neutrons produced for that particular energy. To account for the loss of incoming particles as they reacted to form neutrons, this number was removed from the number of incoming particles. Finally the projectile energy was decreased, and the calculation redone for a new energy. This loop was executed from the highest projectile energy considered (2.5 MeV) to a certain threshold energy for neutron production was reached (or 0 eV).

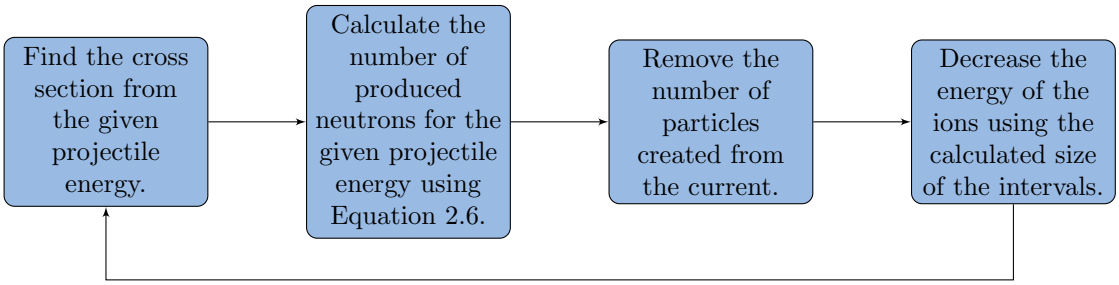

Figure 3.2: The flow chart of the algorithm used.

The calculated neutron yield for projectiles of 2.5 MeV can be seen in the the light grey coloured rows of Table 3.3. The remaining targets in these tables correspond to the neutron yields calculated from the program code DROSG-2000 [37]. DROSG-2000 is a software released under the International Atomic Energy Agency which includes information on 60 accelerator-based reactions for neutron production. The yields obtained from DROSG-2000 serve partly as a comparison to the calculated values made by the author of this thesis.

Before going into any further discussion of the yields in Table 3.3, it is of importance to recognise that the results are largely influenced by the target materials used. The choice of compound will naturally have a profound effect on the number density of target atoms as well as on the range of the ions in the material. The target materials for the lightest elements in Table 3.3 are given as a compound, while the materials considered for the slightly heavier nuclei are of the elements themselves. A similar argument applies to the choice of phase for the target material. Yields of both gas and liquid targets are therefore also stated for some of the reactions in Table 3.3. A continued discussion of the selection of target material is given in Chapter 3.2.3.

With the influence of target materials kept in mind, the calculated values of Table 3.3 are studied. From this, it is evident that the initial suspicions from Table 3.2 are confirmed. For solid targets, the number of neutrons obtained from p-^{9}Be and d-^{13}C are relatively few compared to most of

Table 3.3: Neutron yield with 2.5 MeV projectiles. The light grey boxes are from calculations made by the author. The numbers in the white rows originates from the program DROSG-2000 [37]. The stated maximum energy of the neutron is stated for the forward direction and was obtained from Equation 2.17.

Reaction	**Target**	**Total [n/μC]**	**E$_{n,max}$ [MeV]**
p-T	Ti_2T_3	4.9E8	1.712
p-T	gas	4.8E9	1.712
p-T	T_2O	1.3E9	1.712
d-D	CD_2	2.8E8	5.759
d-D	gas	8.9E8	5.759
d-D	D_2O	2.7E8	5.759
d-T	Ti_2T_3	7.2E8	18.936
d-T	gas	2.5E9	18.936
d-T	T_2O	9.6E8	18.936
p-^{7}Li	Li	9.6E8	0.787
p-^{7}Li	LiF	2.5E8	0.787
p-^{7}Li (n_0)	Li	8.6E8	0.787
p-^{7}Li (n_0)	LiF	2.6E8	0.787
d-^{7}Li	Li	1.1E9	17.058
d-^{7}Li	LiF	3.5E8	17.058
d-^{7}Li	Li	1.4E9	17.058
d-^{7}Li	LiD	9.8E8	17.058
p-^{9}Be	Be	3.5E7	0.574
p-^{9}Be (n_0)	Be	2.8E7	0.574
d-^{9}Be	Be	9.1E8	6.848
d-^{9}Be (n_0)	Be	3.5E8	6.848
d-^{10}B	B	7.1E7	8.914
d-^{11}B	B	3.1E8	15.971
d-^{12}C	C	2.7E8	2.174
d-^{13}C	C	6.8E6	7.804

the other reactions. Compared to p-^{7}Li and d-D, the yield of p-^{9}Be is lower by a factor of 27 and 8. For d-^{13}C, the same comparisons are a factor of 141 and 38. The yield of the other considered isotope of carbon, ^{12}C, is in parity with the yield of d-D, but a factor of 3.5 below p-^{7}Li. The calculated yields of the two isotopes of boron are slightly higher than that of ^{12}C and ^{13}C. These reactions are, however, all outperformed by the reactions using tritium and pure lithium as a target material. The d-^{7}Li-reaction has slightly higher calculated yield compared to that of the p-^{7}Li. The factor of 1.15 is less than from the findings of Lone et al. [38], indicating a factor of 2 in difference to the advantage of the deuteron projectile. The yield from the d-^{9}Be-reaction is also good, being a factor of 2.6 higher than what is obtained from the d-^{7}Li-reaction using a LiF target. If a pure lithium target was to be considered however, the yield of the d-^{7}Li-reaction is a factor 1.2 higher.

The yields of most of the reactions in Table 3.3 are presented as a function of energy in [39]. Generally, the data confirms the trends observed in Table 3.3. This includes the advantage of d-^{7}Li over p-^{7}Li for the energy range of interest in this thesis. Also confirmed is the slight prevalence of the d-^{7}Li-reaction over d-^{9}Be at E$_d$=2.5 MeV. Moreover, the reaction of p-^{9}Be is anew confirmed as being of less importance as a possible source of neutrons for the coming neutron beamline. The yields of d-D and d-T are not included for the projectile energy discussed

here. If the yields are extrapolated however, the given values are relatively close to what was indicated in Table 3.3.

In order to delimit the evaluation of possible accelerator neutron sources, it is of importance to narrow down the selection of reactions. From the discussion around Table 3.3, the first reaction to be disqualified from further evaluation is, not unsurprisingly, p-^{9}Be. The maximum yield of this reaction is around 3.5E7 n/μC, with a maximum neutron energy of 0.574 MeV. The yield is considerably lower than many of the other reactions. From the pure perspective of threshold reactions, higher yields are obtainable with both p-T and p-^{7}Li. In light of this argument, this reaction will not be further elaborated upon.

Comparing the yields of the higher Z-target atoms in Table 3.3, it is evident that the production of neutrons using boron and carbon is of no advantage from the perspective of yield compared to using beryllium. Also noteworthy is the velocity of the produced neutrons. For the most proficient boron isotope, the velocity of the neutrons are much higher compared to those obtained from both the beryllium and carbon target. If the boron target was to be used, this would require an increased length of moderation compared to the two other reactions. Moreover, the recoil products originating from the impinging deuterons on boron and carbon will not facilitate further coincidence measurements. Therefore, in light of these arguments, both the boron and carbon target will not be regarded in the further evaluation.

3.2.2 Evaluation of reactions for accelerator based neutron production

The coming section presents the reactions from Table 3.3 which have been selected for further evaluation, i.e. p-T, p-^{7}Li, d-D, d-T, d-^{7}Li and d-^{9}Be. The reactions are first ordered by projectile (lightest first) and last by target atom (lightest first). If not otherwise stated, the given Q-values and thresholds have been calculated using the QCalc tool from NNDC [40]. The given values do not take into account the energy of the incoming particle. If desired, the maximum kinetic energy of the neutron in a certain angle can be found from Equation 2.17. These values are presented in Table 3.3 for neutrons in the forward direction.

3.2.2.1 p-T

The fusion of protons with tritium forming ^{3}He and neutrons is an important source of neutrons in physics.[41] According to Table 3.3, the reaction is one of the more interesting reactions with respect to the yield of neutrons. Worth noting is that the inverse reaction is a common way to detect neutrons.

$$p + T \longrightarrow {}^{4}_{2}He^{*} \longrightarrow \begin{cases} {}^{3}_{2}He + n \text{ (Q=-0.764 MeV, } E_{th}\text{=1.02 MeV)} \\ {}^{4}_{2}He + \gamma \text{ (Q=19.8139 MeV)} \end{cases} \tag{3.1}$$

Equation 3.1 summarises the p-T-reaction [42]. The reaction is endothermic with a threshold of 1.02 MeV. The release of a neutron with the product ^{3}He is one of the possible exit branches of this excitation shown in Equation 3.1. The other branch is deexcitation through γ-emission leading to the stable ^{4}He. For a 2.5 MeV proton projectile, the maximum energy of the released neutrons in the forward direction is 1.712 MeV. For more energetic projectiles, break-up reactions are also a possibility.[42][43] These reactions are irrelevant to the scope of this thesis because of the physical working range of the accelerator.

The energy of the recoil is of low value having a maximum energy of 1.3 MeV (in the forward direction). The range of such an ion in the given target material of TiT_2 is below 3 μm [28]. This can be compared with the range of protons (E_p=1 MeV-2.5 MeV) in the material being 6.87-27.33 μm. Naturally, the energy, and thus the range, of such an ion is reduced even more in a backward direction. From the perspective of coincidence measurements, this reduces the possibility of being able to detect the recoils and thus performing a coincidence measurement.

3.2.2.2 p-^{7}Li

Historically, the fusion of protons with ^{7}Li has been an important source of neutrons [44]. This reaction is still of importance because of its beneficial yield and low energy divergence at 0° [16][39]. The usefulness of its yield was confirmed in Table 3.3 for E_p=2.5 MeV.

$$p + {}^{7}_{3}Li \longrightarrow {}^{8}_{4}Be^{*} \longrightarrow \begin{cases} {}^{7}Be + n & \text{(Q=-1.644 MeV, } E_{th}\text{=1.880 MeV)} \\ {}^{7}Be^{*} + n & \text{(Q=-2.073 MeV, } E_{th}\text{=2.378 MeV)} \\ {}^{8}_{4}Be + \gamma & \text{(Q=17.254 MeV)} \end{cases} \tag{3.2}$$

Equation 3.2 is a representation of the fusion reaction occurring as a result of bombarding a target consisting of ^{7}Li with protons. The Q-value of the reaction is -1.644 MeV. Once the resulting threshold of 1.880 MeV is overcome, neutron production is possible together with the created recoil of ^{7}Be. As is obvious from Figure 3.1, there is a resonance for proton energies around 2.25 MeV which nearly doubles the value of the cross section. If the energy of the incoming projectiles are increased only a small amount beyond the resonance peak, the threshold of the p-^{7}Be* reaction can be reached. For this a minimum projectile energy of 2.378 MeV is required. If the nucleus is left in its excited state, neutrons with a lower energy signature is emitted.[16][39]

The theoretical energy spectra of the produced neutrons as a function of angle is given in [39]. For projectiles with energies slightly higher than the threshold at 1.88 MeV, the emission of neutrons occurs in the forward direction with a limited emission angle. The benefit of this is threefold. Although the total production of neutrons is lower, the relative percentage of neutrons being emitted in a certain forward direction is higher. Moreover, a lower projectile energy will decrease the energy spread of the emitted neutrons, increasing the resolution. The third benefit is related to the radiation being directed in the forward direction, which possibly decreases the required robustness of backward shielding.[39]

The recoil of the ^{7}Li(p,n)^{7}Be has a maximum energy of 0.616 MeV for E_p=2.5 MeV. The range for such an ion in pure lithium is 5.42 μm. The decay of the ground state of ^{7}Be is through electron capture, transforming the nucleus to ^{7}Li. The half life is 53.22 days [45]. Altogether, this implies that a coincidence measurement using the recoil is difficult to achieve. However, the 0.429 MeV γ-decay from the first excited state of ^{7}Be is fast, being in the order of femtoseconds. It is possible to use such a γ in a coincidence measurement. The downside of this is that this limits the analysis to the neutrons from the reaction resulting in the excited state of ^{7}Be. From DROSG-2000, it is clear that the neutrons from this energy group is a factor 10 lower compared to the n_0. A possible alternative to such a measurement is to use a deflector coupled with the ToF-method.

3.2.2.3 d-D

The nucleus of a deuterium atom consists of both a proton and a neutron. Being an isotope of hydrogen, it is probably most famous in the state where it is bound to an oxygen atom, a molecule called heavy water (D_2O). The fusion reaction occurring as a deuterium ion is projectiled onto a deuterium target, is a commonly employed reaction for neutron production [39]. For projectiles of 2.5 MeV, it is seen in Table 3.3 that the yield from this reaction is comparable to that obtained from the p-^{7}Li-reaction.

$$d + D \longrightarrow {}^4_2He^* \longrightarrow \begin{cases} {}^3_2He + n & \text{(Q=3.269 MeV)} \\ T + p & \text{(Q=4.032 MeV)} \\ \alpha + \gamma & \text{(Q=23.846 MeV)} \end{cases} \tag{3.3}$$

Equation 3.3 is a summary of the possible exit branches resulting from the fusion of deuterium projectiles targeted on a deuterium target.[43][46] The deexcitation of the compound nucleus has a low probability of exiting through the forbidden γ-emission. The first two branches of Equation 3.3, involving an ejectile of either a neutron or proton, have a probability close to 0.5 each [46]. For this thesis, the main branch of interest is the formation of ^{3}He and a neutron. The reaction is exothermic with a positive Q-value of 3.269 MeV. The threshold for the break-up reaction forming D, n and p is, again, above the energy range relevant for this thesis.[47]

The maximum energy of the recoil at E_d=2.5 MeV is around 4.131 MeV in the forward direction. At an angle of 45° relative to the incoming beam, this energy is ∼2.5 MeV. The maximum range of such an ion in CD_2 is 14.3 μm. This can be compared to the range of the deuteron projectile being 66.4 μm. To be able to detect such an ion, the distance into the target where the reaction is allowed to occur is maximum around 10 μm. This corresponds to an energy loss of the deuteron of around 0.25 MeV. Even though possible to perform, such a measurement would limit the usefulness of this reaction since only a relative low part of the total produced neutrons would be possible to detect in coincidence with the ^{3}He.

3.2.2.4 d-T

The fusion reaction of deuterium with tritium has a Coulomb barrier of 0.4441 MeV, corresponding to the lowest barrier of the evaluated reactions. Partly because of the low barrier, this is the reaction which is most probable to be used in possible future fusion reactors. As can be seen in Table 3.3, the d-T reaction is a potent source for producing neutrons using an accelerator. From Figure 3.1 it is evident that this reaction should be the most effective reaction in producing neutrons if lower energetic projectiles are used.

$$d + T \longrightarrow {}^5_2He^* \longrightarrow \begin{cases} \alpha + n & \text{(Q=17.6 MeV)} \\ {}^5_2He + \gamma_0 & \text{(Q=16.75 MeV)} \\ {}^5_2He + \gamma_1 & \text{(Q∼13.5 MeV)} \end{cases} \tag{3.4}$$

Equation 3.4 gives a summary of the d-T reaction[48]. As deuteron projectiles bombard a target of tritium, a compound nucleus of $^5_2$He can be formed. The common deexcitation thereof forms an α and a neutron. Since the reaction has a positive Q-value of 17.6 MeV, the maximum possible neutron energy is expected to be large. This is also confirmed in Table 3.3, giving the maximum energy of the neutrons to around 19 MeV if 2.5 MeV projectiles are used. However,

the deexcitation of the compound nucleus can also result in the emission of γ-quanta. For this thesis, the highest photon energy is in the 16.75 MeV range, relating to the transition to the ground state of $^{5}_{2}$He (which thereafter decays with the emission of a neutron and an α). From the same excited level, a γ-transition to the first excited state of $^{5}_{2}$He is also possible. The energy of this γ-quanta is uncertain and is thereby noted in Equation 3.4 with a tilde. Related to the energy used in the experiment for the d-T-reaction, the branching ratio between γ- and neutron-emission is in the order of 10^{-4}-10^{-5}.[48][49]

For E_d=2.5 MeV, a coincidence measurement could be hard to implement because of the higher penetration depth of the incoming deuterons compared to the range of the fusioned α-particles. This could be resolved by reducing the energy of the projectile, limiting the maximum depth of the reaction. As will be demonstrated in Chapter 4.4.4, this is feasible. From Figure 3.1, it is evident that if the energy of the deuterons is lowered within reasonable limits, the decrease in yield should be small because of the high resonance at lower projectile energies.

3.2.2.5 d-^{7}Li

Using accelerators to produce neutrons by bombarding deuterons on a ^{7}Li-target is common [50]. As was previously mentioned, the obtained values of the cross section for this reaction are scarce. If the extrapolated values are relevant, its potential as a source of neutrons is large. Regardless of the accuracy of the cross sectional values, the relative high yield of this reaction was confirmed in [39].

$$d + {}^{7}_{3}Li \longrightarrow \begin{cases} {}^{8}_{4}Be + n & \text{(Q=15.03 MeV)} \\ 2\alpha + n & \text{(Q=15.12 MeV)} \\ {}^{5}_{2}He + \alpha & \text{(Q=14.39 MeV)} \\ {}^{9}_{4}Be + \gamma & \text{(Q=16.69 MeV)} \end{cases} \tag{3.5}$$

Equation 3.5 is a summary of the d-^{7}Li-reaction with focus on neutron production and γ-deexcitation. The reaction is more complex than the previously mentioned reactions, involving direct two- and three-body branches as well as the formation of a compound nucleus ($^{9}_{4}$Be) and the different possible deexcitation branches thereof [51][52]. In the equation, four different branches of the reaction are stated, all with a high Q-value. The maximum energy of the neutrons can thus be relatively large. In the forward direction, Table 3.3 states this value to $\sim$17 MeV. As the stated exit branches of Equation 3.5 also involve three-body break-up reactions, a continuum of neutron energies can be obtained. The fusion reaction forming $^{9}_{4}$Be and the related γ-emission is only of minor importance. For the energies considered in this thesis, the branching ratio of γ-emission over neutron emission is, in most cases very low.[53] The density of levels in ^{8}Be is much higher above 16.6 MeV. Thus, even when more energy is supplied to the system, the relative yield of fast neutrons decreases in favour of lower energy neutron emission to the higher excited states of ^{8}Be.[38]

Coincidence measurements are not as certain for d-^{7}Li as for the d-T-reaction. The problem is twofold. The main problem concerns the range in LiF. The range of the most energetic ^{8}Be-ions is 6.5 μm, compared to the range of 2.5 MeV deuterons being 36.44 μm. The decay of ^{8}Be to two α (Q=92 keV) additionally complicates the analysis. If the decay to α-particles is prompt, and they share the maximum energy of the ^{8}Be-ion, the maximum energy of one α should correspond to a range in LiF of about 6.8 μm. This corresponds to a maximum energy loss for a 2.5 MeV ion of about 0.25 MeV. From Figure 3.1 it is evident that if a similar approach is taken as was

suggested for the coincidence measurement for the d-T-reaction, i.e. the lowering of the projectile energy to limit the range into the target, the yield will be affected more drastically. The range of a deuteron of around half of the original projectile energy is ∼13 μm. The resulting maximum energy of the recoil is then around 3 MeV at around 45° relative to the incoming beam. This corresponds to a range of ∼4.36 μm. The maximum energy loss of the deuterons is thus around 0.3 MeV (i.e. before the distance into the target is too deep for the ions to escape). Again, such an approach would affect the yield much more drastically than for the d-T reaction. The alternative of using a deflector to tag the beam is not relevant because of the highly energetic neutrons resulting from this reaction.

3.2.2.6 d-^{9}Be

The production of neutrons using deuterons impinging on a beryllium target is not uncommon [39]. The reactions with relevance for the scope of this thesis are summarised in Equation 3.6. Noteworthy is the exothermic characteristics of the production of a neutron and boron, having a positive Q-value of 4.36 MeV. This Q-value is much lower than that of the d-^{7}Li-reaction, resulting in neutrons where the maximum energy is a factor 2.5 lower than that obtained from the lithium target.

$$d + {}^{9}Be \longrightarrow \begin{cases} {}^{10}B + n & \text{(Q=4.36 MeV)} \\ {}^{6}Li + n + \alpha & \text{(Q=-0.989 MeV, } E_{th}\text{=0.121 MeV)} \\ 2\alpha + n + d & \text{(Q=-1.572 MeV, } E_{th}\text{=1.924 MeV)} \\ {}^{8}Be + n + d & \text{(Q=-1.665 MeV, } E_{th}\text{=2.037 MeV)} \end{cases} \tag{3.6}$$

As was previously discussed, the neutron yield of this reaction is relatively high, comparable to that of d-^{7}Li. One reason for this is because of excited states in ^{10}B. In Chapter 2.1, it was mentioned that such resonances will contribute to an increase of the total neutron yield. For the projectile energies relevant to this thesis, the threshold reactions stated in Equation 3.6, as well as the resonances, will significantly increase the yield of lower energetic neutrons.[54][55]

The energy of the recoil of ^{10}B, i.e. the product of the first reaction indicated in Equation 3.6, is ∼1.1 MeV at an angle of 45° relative to the incident ions. The range of such an ion is 1.65 μm in the given material. If this is compared with the range of 2.5 MeV deuterons, it is evident that the coincidence technique is not a feasible solution for the recoil product of this reaction. However, if a solution using a deflector or a chopper is considered, such a system could be used coupled with the method of TOF.

3.2.3 Target compositions

In Chapter 3.2.1, the influence of the target material on the calculated yield was briefly mentioned. Here, the discussion of different target materials will be continued for the reactions which were chosen for further evaluation in Chapter 3.2.2.

For the calculation of the yield from the d-D reaction, a deuterated plastic was chosen as the target material. A solid target could use a number of other compositions, e.g. TiD_2, ZrD_2. From an analysis of the range in SRIM, as well as a comparison of the cross sections, the choice of using the deuterated plastic (CD_2) is the most beneficial from the point of view of yield [28] [56]. The finding is confirmed in [57] which, however, also points to the problem of erosion with deuterated plastics as target materials. Thus, even though the yield is higher from the deuterated plastic,

a metal target could be more beneficial from the perspective of durability. Recently, improved techniques for the manufacturing of deuterated polyethylene have been suggested [58]. In these, both carbonisation and changes to the thickness of the plastic were observed using an ion beam of ^{134}Xe. It is currently unclear how such a target would withstand a beam of deuterons. For the d-D reaction, liquid or gas targets are alternatives to the use of solid targets because of the limited use of the recoil for coincidence measurements as discussed in Chapter 3.2.2.3. From the calculations of DROSG-2000 [37], it was clear that a gas target is a factor 3 more prolific than both a solid and a liquid target. Thus, for this reaction, a gas target could be chosen for its higher yield, even though a solid target would be easier to handle.

The yield of the reactions related to tritium in Table 3.3 was calculated using a Ti_2T_3-target. In solid targets, a titanium layer is common to use in order to absorb tritium into its structure [59] [60]. A problem with such targets is the relatively low temperature where tritium begins to be released from the titanium structure (250°C) [35]. This problem can be prevented with an appropriate cooling system. To increase the range of the ions, a lower-Z-material is desirable. Unfortunately, information of such targets has not been found. An alternative to a solid composite target is tritium in its gas state. Calculations thereof were also given in Table 3.3, showing a substantial increase in yield for the p-T reaction (a factor of 7). For the d-T reaction, the increase was below a factor of 3. As was shown in Chapter 3.2.2.3, the d-T-reaction is suitable for coincidence measurements using the recoil of the reaction. This constitutes a problem using a gas target, because of the encapsulating container of the gas. The walls of such a container will block the recoil, preventing it from reaching the detector [61]. For the p-T-reaction however, a gas target could be an alternative, because of the limited possibilities of using a coincidence measurement as discussed in Chapter 3.2.2.1.

The calculations of the yield from p-^{7}Li and d-^{7}Li in Table 3.3 was based on two different targets, pure lithium and lithium fluoride. Additionally, the calculated yield from the use of a deuterated lithium target was provided from DROSG-2000. Of these target compositions, the highest yield was obtained for the pure lithium metal with the deuterated lithium closely behind (a factor of 1.4). The least prolific target material found was that of the lithium fluoride. The reason of the inclusion of other target materials in spite of lithium being a metal, is because of its troublesome characteristics, having a low melting point of 160°C as well as being highly reactive with air [62]. If a target of lithium hydride was to be used instead, the melting point would rise to 690°C and the yield would decrease with 30% [62]. With a lithium fluoride crystal, the melting point would increase additionally to 850°C, while the neutron yield would decrease close to 70% compared to a pure lithium target. It is probable that the yield of a target of lithium deuteride would be an improvement over that of lithium hydride for deuteron projectiles. In the work of [63], it is clear that the melting points of these two compositions are of similar value. Therein, it is also stated that the lithium deuteride is castable and could be use as a target in a cyclotron. More relevant information concerning the use of lithium deuteride for neutron production was not found. The use of a pure lithium solid target for neutron production is, however, an alternative. As has been shown by [62], such a target is in need of rigorous cooling and a simple mechanism for the exchange of old targets to new. More recently, interesting developments on a liquid-lithium target has been presented, accompanied with expectations of outperforming solid lithium targets [64] [65].

The calculated yield of the d-^{9}Be reaction was found using a pure beryllium target. Beryllium is advantageous to lithium metal for a number of reasons. The melting point of beryllium is 1285°C, more than a thousand degrees higher than that of pure lithium [66]. Its thermal conductivity of 180 W/mK is more than a factor 2 higher than that of pure lithium and a factor 15 higher than for LiF [65] [36]. Furthermore, beryllium has better mechanical properties than lithium and is

also easier to handle [66]. The problem of blistering, where protons which did not partake in the fusion process recombine with electrons and cause damage to the structures of beryllium, has been dealt with in recently developed three-layered targets [67].

3.2.4 Reactions of relevance for the experiment

In this section a brief introduction is given to some further reactions which are of relevance for the analysis of the experimental results given in Chapter 4.

3.2.4.1 d-C

The potential for the production of neutrons using carbon was presented in Table 3.3. Even though the reaction results in a useful neutron flow, it was not selected to be further evaluated as a target for reasons previously stated. However, it is of importance to introduce this reaction because of the composite materials used in some targets during the experiment. Moreover, as will be highlighted in Chapter 3.4, this reaction is also of relevance from the perspective of beamline construction. For this case, both d-^{12}C and d-^{13}C are presented in Equation 3.7. Herein, the C(p,n)-reactions were left out because of the high thresholds. The cross sections for the deuteron induced reactions can be seen in Figure 3.1.

$$\begin{array}{rcccl} d & + & ^{12}C & \longrightarrow & ^{13}N + n \quad \text{(Q=-0.281 MeV, E}_{th}\text{=0.328 MeV)} \\ & & ^{13}C & \longrightarrow & ^{14}N + n \quad \text{(Q=5.326 MeV)} \end{array} \tag{3.7}$$

3.2.4.2 x-^{19}F

The reactions of p-^{19}F and d-^{19}F are important to present because of the compound material of lithium fluoride used in the experiment. As will be seen in Chapter 4, this target was used for both proton and deuteron projectiles. The reactions are presented in Equation 3.8 and 3.9.

$$p + ^{19}F \longrightarrow \ ^{19}Ne + n \quad \text{(Q=-4.022 MeV, E}_{th}\text{=4.235 MeV)} \tag{3.8}$$

$$d + ^{19}F \longrightarrow \begin{cases} ^{20}Ne + n & \text{(Q=10.619 MeV)} \\ ^{16}O + \alpha + n & \text{(Q=5.889 MeV)} \\ ^{12}C + 2\alpha + n & \text{(Q=-1.273 MeV, E}_{th}\text{=1.408 MeV)} \end{cases} \tag{3.9}$$

Considering protons, it is evident from Equation 3.8 that the threshold for neutron production is above the maximum projectile energy available at the accelerator of LIBAF. For deuterons however, a number of different neutron producing reactions are possible. In Equation 3.9 it is seen that two of the possible reactions has a relatively high Q-value. If an isotropic approximation is done on the partial cross section of the two-body-reaction for E$_d$=3.1 MeV, the maximum total cross section amounts to ∼0.09 b [68]. Since different excited levels of ^{20}Ne are possible to be entered, there is a high probability of emitting an α-particle according to the second branch of Equation 3.9. If the decay enters excited levels of the daughter ^{16}O, α-emission is possible anew. Naturally, such a decay would create ^{12}C.

3.2.4.3 γ-contamination

Related to the experiment is also the possibility of having γ-contamination, the reason being the detection equipment of plastic scintillators without pulse-shape discrimination. Concerning all of the presented reactions, it is probable to have emission of γ-radiation below 10 MeV. γ-quantas above that energy are possible, but more improbable. For a more thorough presentation of the γ-yield from thick targets bombarded with deuterons, a spectrum can be found in [69].

As will be highlighted in Chapter 4.4, a high percentage of the generated γ-radiation is blocked using blocks of lead in front of the detector. However, to reduce the background further, the products of nuclear reactions/scattering related to both the proton and the deuteron can likely be used in a coincidence measurement. This was, however, not verified during the experiment.

3.3 Evaluation of Moderator Materials

Chapter 2.3 introduced the concept of neutron moderation and the related processes of elastic and inelastic scattering as well as radiative neutron capture. It was mentioned that while hydrogen rich materials are the most effective in slowing down neutrons, the high cross section for neutron absorption is an issue. Because of the problem of neutron absorption, other materials should be considered in order to find a suitable moderator with the characteristics of a high probability of thermalising neutrons as well as a low probability of neutron absorption. This chapter presents such an evaluation of commonly used materials for moderation, starting from the perspective of the first two processes.

The comparison of different moderator materials can be simplified through the concept of moderating ratio (MR) given in Equation 3.10,

$$MR = \frac{\xi \Sigma_s}{\Sigma_a}, \tag{3.10}$$

where ξ is the average lethargy change for one collision previously introduced in Chapter 2.3, Σ_s the macroscopic scattering cross section and Σ_a the macroscopic absorption cross section. The macroscopic cross section was previously defined in Equation 2.2. The numerator in Equation 3.10 can be defined as the moderating power of a material (MP). This quantity does not take into account the thermal absorption rate of a certain material. Thus, the moderating ratio of Equation 3.10 is a better indicator of the moderating efficiency for different materials.[70]

To find the moderating ratio of a compound, i.e. a material made up of different atoms, two quantities need to be redefined, the macroscopic cross section and the average lethargy change. The redefinition of the macroscopic cross section from Equation 2.2 to that of a compound material is given in Equation 3.11,

$$\Sigma = \frac{\rho N_A}{M}(n_1\sigma_1 + ... + n_i\sigma_i), \tag{3.11}$$

where M is the molecular weight of the compound and n_i the number of atoms of element i in one molecule of the compound.[71]

The second quantity to be redefined is the average lethargy change after one collision from Equation 2.26. For a compound material it is presented in Equation 3.12. The index i relates

the cross sections and the average lethargy change to a certain element of the compound.

$$\xi = \frac{\sum \xi_i \sigma_{s,i}}{\sum \sigma_{s,i}} \tag{3.12}$$

Table 3.4 is a summary of parameters of commonly used moderator materials relevant for further evaluation. Parameters included are the density of the material, the lethargy, the macroscopic cross sections of scattering and absorption, the number of collisions needed on average for thermalisation, the moderating ratio (MR) and the moderation power (MP). The two columns included beneath the wings of the overarching column named "Number of Collisions" are denoted by the starting energy, E_{n0} (MeV), of the neutrons before moderation. The first of the two included starting energies represents the fastest neutrons obtainable using projectiles at 2.5 MeV, i.e. the ones obtained from the d-T reaction. The second subgroup is the fastest neutrons obtained from the p-^{7}Li reaction at the same accelerator potential. The required number of collisions for thermalisation are calculated down to thermal energy (0.025 eV). Thus, the non-validity of the approximation of the moderating nucleus being at rest relative to the incoming neutron at thermal energies is overlooked.[72]

Table 3.4: Calculated moderator parameters. Relevant microscopic cross sections and densities were obtained from [5], [71] and [72].

					Number of Collisions			
	ρ	ξ	Σ_s	Σ_a	18.94	0.768	MR	MP
H_2O	0.998	0.923	1.492	0.022	22	19	62.1	1.38
D_2O	1.1	0.505	0.354	0.00004	40	34	4458	0.18
CH_2	0.94	0.912	1.841	0.027	22	19	62.3	1.68
CD_2	1.06	0.492	0.460	0.00018	42	35	1294	0.23
Be	1.85	0.207	0.743	0.00094	99	83	163.1	0.15
C	1.6	0.158	0.381	0.00027	130	109	222	0.06
	[g/cm^3]		[cm^{-1}]	[cm^{-1}]				

The number of collisions on average needed to thermalise a neutron given in Table 3.4 reflects the initial theory in Chapter 2.3. Moderator materials of higher A will on average require more collisions before the neutrons are thermalised. If this number is compared for the two different E_{n0}, it is worth noting that the difference in the number of required collisions increases with an increase of A. Thus, for hydrogen rich materials, the difference in the required number of collisions for thermalisation between the two starting neutron energies is the lowest (3) of all the evaluated materials. The same number for pure carbon moderators is 21. This number could give an initial idea of how much different moderators would need to be modified in order to optimise the number of thermalised neutrons for different E_{n0}. However, such modifications would also need to be balanced from the density of the material, the cross section for scattering and absorption and the average scattering angle.

The average number of collisions needed for thermalisation, as well as the moderating power, confirm what has already been mentioned in part. Materials involving hydrogen are by far the best moderators to use if a compact moderator is desired. However, because of the high absorption cross section of such materials, the moderating ratio is only average. The implication of the high moderating power but low moderating ratio, is that the size of such a moderator

is critical. If neutrons are over-moderated in this type of moderator, the thermal flux will be largely reduced. This can be contrasted with the high moderating ratio in deuterium rich materials. Their high moderating ratio is primarily caused by the low absorption cross section of deuterium. Even though the moderating power is significantly lower than for hydrogen rich materials, moderators with deuterium is of interest for the further discussion.

Beryllium and carbon are two other materials possible to use as moderators. Evidently, the number of required collisions for both materials are higher than for moderators consisting of either hydrogen or deuterium. The moderating power of pure carbon is low compared to most other materials in Table 3.4. Its moderating ratio, however, is triumphed only by the deuterium rich materials. For beryllium, the value of the moderating power is lower than that of both hydrogen and deuterium rich materials. Even though its moderating ratio is relatively high (above that of light water), its toxic characteristics makes the use of it questionable [73]. If proper security precautions are taken (for example enclosing and ventilation), beryllium could prove to be a viable alternative.

From the values in Table 3.4, it is evident that a larger moderation thickness is required if non-hydrogenous materials are to be used compared to hydrogen rich materials. For a given neutron producing reaction, the optimal size of moderators of different materials could be found using Monte-Carlo simulation software such as Geant4, MCNP or McStas. As different nuclear reactions will result in the emission of different neutron groups, the decision of which reaction and ion energy to be used in the future beamline at LIBAF needs to predate an optimisation simulation. Therefore, only some results of [74] on simulations of heavy water and light water moderators will be discussed here.

The simulation of [74] proceeds from the neutrons produced by 11 MeV protons impinging on a beryllium target (r=2 cm) surrounded by a beryllium reflector. The neutrons were thereafter moderated by either light or heavy water. Evidently, the projectile energy is beyond the reach of the accelerator at LIBAF, however, as p-^{9}Be is a threshold reaction, the energy of the produced neutrons are within the scope of this thesis. For a calculated spectrum of this reaction see [75].

In the simulation, an optimal cross sectional area of the moderators were found by specifying their thickness. The optimal thickness was thereafter found by fixing the area. The simulation provided an optimal dimension of the light water moderator of 30x30x4cm. For the heavy water moderator, the corresponding optimal dimension was found to be 50x50x18cm. For such a setup, the thermal flux was found to be about 1.7 times higher for the moderator with heavy water (5 m away from moderator, E_n <0.5eV). The increase of thermal flux using deuterium rich materials is not to be unexpected from the values in Table 3.4. The general trend was confirmed in the simulation of [76] on the moderation of neutrons from a ^{252}Cf source. Therein, it is also worth noting that a moderator of carbon was found to be less effective in thermalising neutrons than a moderator of heavy water.

The two simulations introduced above gave that heavy water was the best moderator from the pure perspective of thermalising neutrons. Another way of evaluating moderators is by comparing the characteristic neutron brightness on the surface of each moderator. The brightness is related to the L/D-ratio, where L is the length between the moderator and the target, and D the side length of the moderator. The L/D-ratio is a factor indicating the quality of the neutron beam (collimation) and thus the spatial resolution [77]. A plot of a simulation of the brightness on the surface of the two discussed moderators is presented in Figure 3.3. It is clearly seen that the thermal neutron flux in the centre of the moderators is higher for the light water moderator. Accordingly, for the same value of L, a higher value of the L/D ratio can be achieved using the light water moderator [74]. The result is refined in [77], confirming that if both the spatial

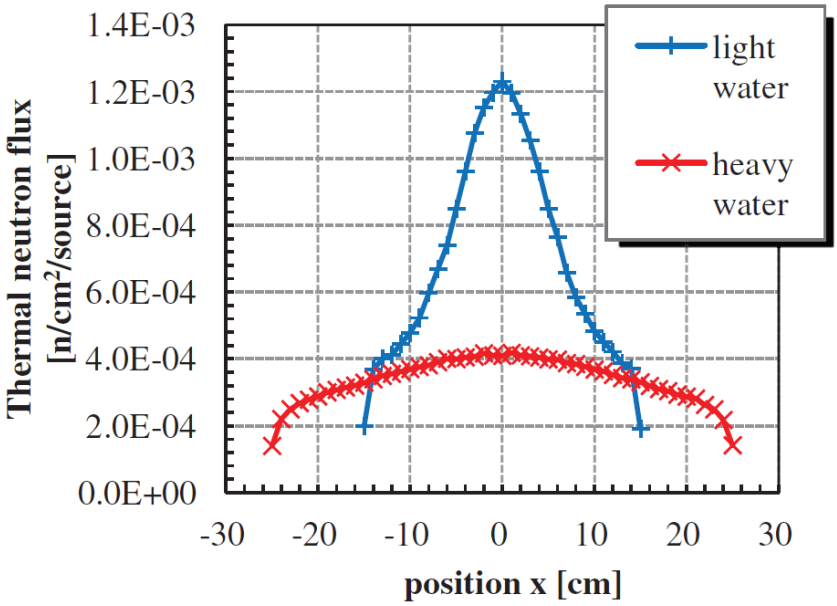

Figure 3.3: The thermal flux on the surface of the moderator as a function of distance from the centre. Results from the simulations of [74].

resolution of the beam and the thermal flux is taken into account, a smaller moderator of light water is more advantageous than using a larger moderator of heavy water.

An evaluation of moderator materials could also benefit from analysing the different pulse widths after moderation, i.e. the pulse broadening resulting as the pulsed neutron beam passes through the moderator (the pulse width is also a function of the duration of the pulsed ion beam) [78]. The pulse width is of importance for the energy resolution of an experiment and will depend on the wavelength of the neutrons [78]. In [74], simulations of the emission time as a function of wavelength for H_2O and D_2O were performed. The result is presented in Figure 3.4. Evidently, the pulse length of the slower neutrons (<0.1eV) is much longer in heavy water compared to light water. The increased pulse length could possible facilitate measurements of neutrons of a certain wavelength. Nonetheless, a broader pulse post moderation would require a reduction of the ion beam pulse frequency. Noteworthy is that the use of deuterium moderators (cold) are not preferred at short-pulsed spallation sources because of this issue [79]. The increased pulse length, and therefore also the decreased resolution, could be dealt with by installing a chopper [80].

The discussion above has highlighted the importance of deciding both the reaction to be used for neutron production and for what purpose the neutrons will be used. Beyond this, factors like wieldiness/adaptability, activation, toxicity and cost are of importance when evaluating possible moderator materials. The toxicity related to beryllium has been briefly touched upon. The remaining factors will be introduced in the following.

From the perspective of cost, the required investment for some of the moderator materials can be estimated from the optimal dimensions of a light water or heavy water moderator previously presented. Since light water is abundant and cheap, the cost thereof is minimal. It would however be beneficial to use high-purity water, i.e. water which has been demineralised [4].

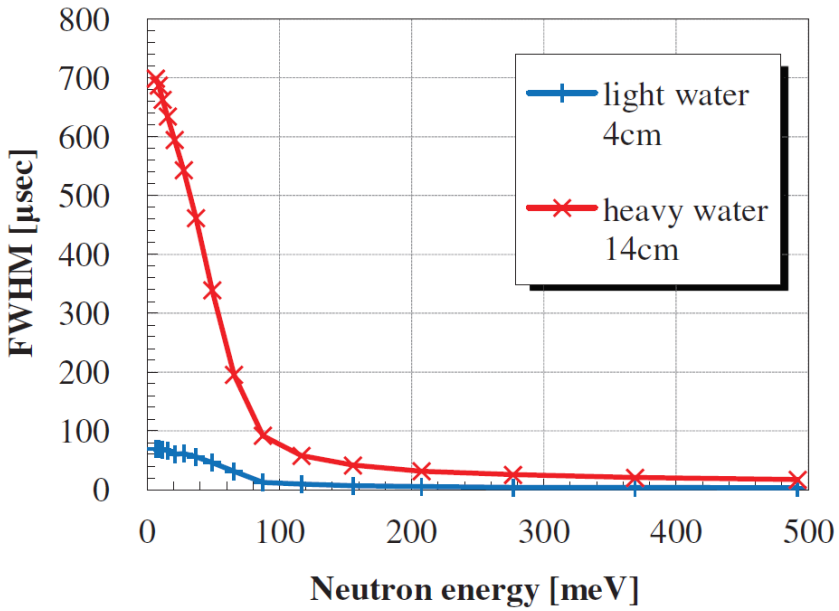

Figure 3.4: The full width half maximum (FWHM) time of emission of neutrons after moderation as a function of energy. Result from the simulations of [74].

The cost of purified water from the stated optimal dimension would be cheap because of its availability inhouse. Heavy water is more expensive than light water. The cost will depend on its percentage of isotopic purity. For the required 45 litres of heavy water (corresponding to the optimal dimension obtained from the simulation), this would amount to a minimal investment of 200 000 SEK for 99.9 % isotopic purity [81]. The required investment using a beryllium moderator is unknown. Yet, as reported by [82], it would amount to a high cost. In view of the cost of fine nuclear graphite (σ_a=3.8 mB) being around 2500$/ton (machined), the investment involved choosing a graphite moderator is relatively low [83].

In order for the facility to be able to offer user access to different kinds of neutrons, the perspective of moderator adaptability and wieldiness is of importance. From this perspective liquid moderators are more cumbersome than solid. If, for example, plastic blocks were to be used instead of water, the straightforward adaptability of the construction would increase. In Table 3.4, the difference of the moderating ratio and moderating power between liquids and solids of a certain isotope can be seen. For the hydrogen rich materials the difference in MR is minimal. The difference in MP, however, is to the advantage of the organic material (CH_2). For deuterium rich materials, the liquid is of much higher MR, while the deuterated plastic (CD_2) has a small advantage comparing the MP. If an organic material is chosen as the moderator, future analysis of the disintegration products caused by irradiation and its inflammability is required [82]. Related to the wieldiness is the point of activation. From this perspective, it is noteworthy that the amount of γ from radiative capture will be lower for the deuterium rich materials compared to moderators with hydrogen [79]. On the other hand, a much lower amount of atoms will be tritiated in ordinary water compared to heavy water. Thus, if a deuterium rich moderator is chosen, the increased level of activation would require a more careful handling.

3.3.1 Cold neutrons

The discussion above has been limited to the moderation of fast neutrons to thermal energies. For certain applications (e.g. scattering experiments) it is of interest to use cold neutrons. Cold neutrons are defined as being in the energy range between 0-0.025 eV. For this purpose liquid hydrogen/deuterium and solid methane can be used. An evaluation of these materials and the related cryogenics is not within the scope of this thesis. It is only listed here for the sake of completeness and as a future reference.[78][80]

3.3.2 Multiple moderator layers

It has previously been noted that the use of heavy water as a moderator would result in a higher thermal flux compared to using ordinary water. The higher flux was related to the much lower absorption cross section in heavy water. If a reaction like d-T is to be used with the release of very fast neutrons, the mean free path of the unscattered neutrons will be relatively large. The reason being that at higher neutron energies, i.e. around 14 MeV and above, the cross section for scattering is low (<0.5 b) in both light and heavy water [32]. With this issue in mind, a more efficient approach would be desirable in order to facilitate the thermalisation of neutrons. This is where multiple moderator layers have been introduced as a possible way to increase the thermalisation efficiency.

Multiple moderator layers are used in order to be customised to meet the neutrons at different part of their lifetime. Thus, a material can be chosen to effectively moderate the initially very fast neutrons and then another material to effectively thermalise them. Two materials possible to use as premoderators are tungsten and lead [84]. According to Equation 2.23, heavy elements will not have a huge impact on the decrease of the neutron energy through elastic scattering. However, if the incoming 14 MeV neutrons are scattered inelastically on heavy elements, the reduced energies are often below 3 MeV [84]. The cross section for inelastic scattering of lead/tungsten is not higher than that of elastic scattering in water [32]. This is however compensated by the higher density in lead/tungsten. The large decrease of neutron energy if the scattering is inelastic is not the sole advantage of using a premoderator material of lead or tungsten. At higher neutron energies, the heavier materials have a cross section around 2 b for (n,2n) [84]. Neutron multiplication is a threshold reaction with E_{th}=6-8 MeV depending on which isotope of lead/tungsten is involved. Thus, as a beneficial side effect of the desired moderation, a neutron multiplication effect can be achieved.

An evaluation of which material to use involves considering the moderating ratio, multiplication effect, threshold and cost. For the two materials mentioned previously (lead and tungsten), the multiplication cross section is almost equivalent. Hence, of greater importance to the current discussion are aspects concerning moderation ratio and cost. Costwise, tungsten is much more expensive compared to lead [84]. The moderating ratio was introduced previously in Chapter 3.3. It is connected to the cross sections of a material (elastic, inelastic and absorption) and density. The ability to moderate neutrons is much higher for tungsten because of its density being almost the double of lead [84]. For tungsten, however, the thermal absorption cross section is more than two order of magnitudes higher compared to lead. With this in mind, Monte-Carlo simulations would be beneficial to a final evaluation. Naturally, such an evaluation could also benefit from considering other materials (e.g. beryllium, copper and molybdenum) [85].

3.4 Dump target

In the coming neutron beamline at LIBAF an electrical system could be used in order to deflect the beam off from and back on to the target with a certain frequency. Such a deflection system can create well defined neutron pulses which could be used to tag neutrons. A beam dump will be used to collect the incoming particles when the beam is deflected away from the target. As the material of the dump will be activated by both impinging ions and neutrons, the purpose of this section is to find a material having a low probability of producing neutrons [86]. Since the beam will be dumped into this material, it is also of importance that the material has a high melting point and thermal conductivity as well as good electrical characteristics.

The materials that will be investigated are primarily those currently being used in other accelerator facilities [87] [88] [89]. As an example, a commonly used dump target for protons at LIBAF is carbon. This material will therefore be analysed together with iron, copper, tantalum, tungsten and gold. The materials were treated in a similar manner as the materials used for neutron production. The relevant cross sections proved hard to come by in the desired energy range, especially for deuteron projectiles. Moreover, the found cross sections were often given with around 1 MeV in between each value. The following evaluation is thus based on the assumption that the cross sections behave in a non-resonant fashion in between each value. The cross sections for the different elements are presented in Figure 3.5 and 3.6, where each isotope of an element has been coded in the same colour but different symbol. Also noteworthy is that it is only for the heavier elements that the data from both the proton and deuteron projectiles have been plotted. This is because of the too high threshold for the (p,n)-reactions of the lighter elements.

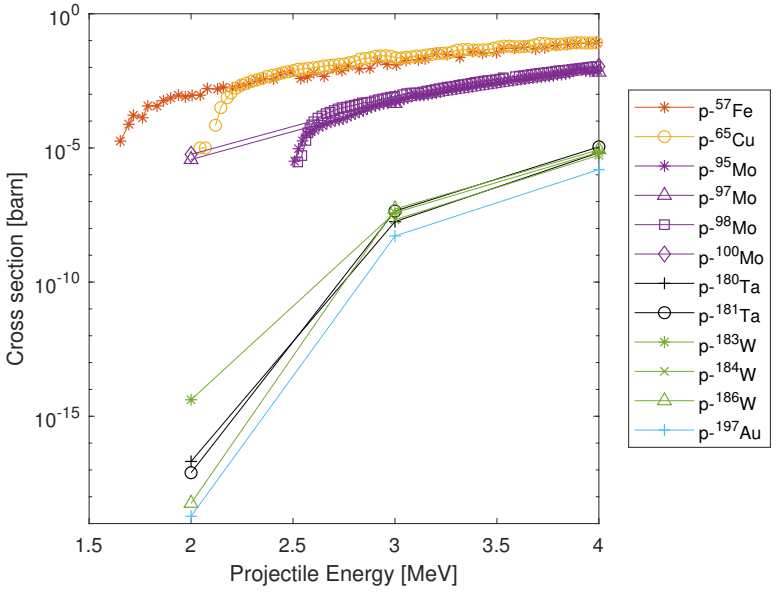

Figure 3.5: Cross sections of possible dump materials for proton projectiles. For the lighter materials the (p,n)-cross section has not been included since the threshold energy is above 3 MeV. The cross sections were obtained from [32] and [56].

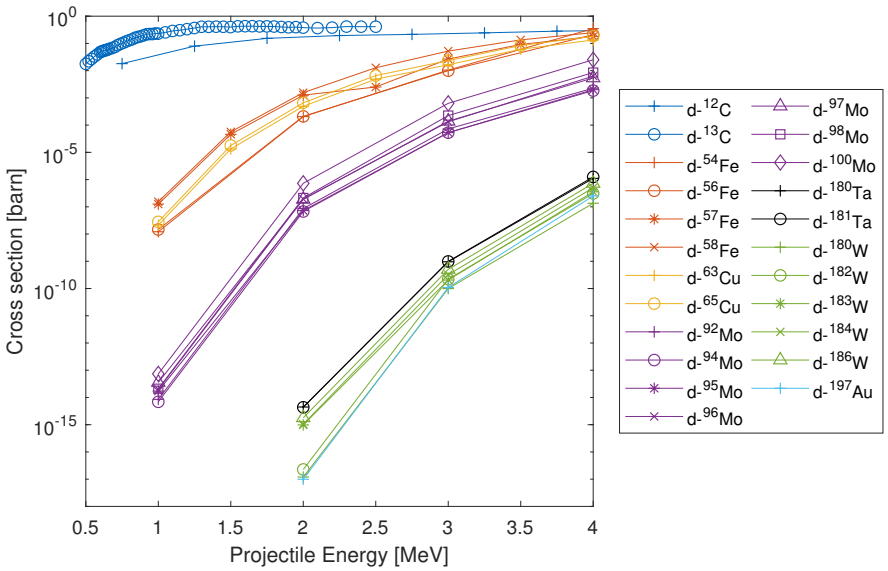

Figure 3.6: Cross sections of possible dump materials for deuteron projectiles. The cross sections were obtained from [56].

Even though it is important to not draw exhaustive conclusions from the scarce data sets in Figure 3.5 and 3.6, some general trends can still be distinguished. To begin with, it can clearly be seen that carbon is not a suitable dump material if deuteron projectiles are used since the cross sections of both d-^{12}C and of d-^{13}C are too high. For proton projectiles carbon is still a viable alternative because of the too high energy threshold for neutron production ($E_{th} > 3$ MeV). The cross section for neutron production in iron, copper and molybdenum are relatively high for protons. Although being lower than for carbon, their cross sections for neutron production with impinging deuterons are also relatively high. From the given data sets, the heavier elements of tantalum, tungsten and gold seem to be the most promising as the cross sections of the (p/d,n)-reaction are very low in the given energy range. For the heavier elements, these cross sections are relatively similar.

The conclusions above are confirmed in the experimental results of Simakov et al. [86]. Their findings are presented in Figure 3.7 for projectile energies of 9 MeV (protons) and 16 MeV (deuterons). These energies are higher than what will be used at the coming neutron beamline of LIBAF. The yields are therefore not entirely applicable. Nonetheless, it is worth to note that carbon is confirmed as being a viable alternative only for protons. This was suspected from the previous analysis of the cross sections and thresholds. Moreover, even though copper is confirmed as a better alternative than carbon for deuterons, its neutron yield is still more than a factor 10 higher than that of the heaviest materials previously considered in Figure 3.5 and 3.6. For the energies relevant for LIBAF, it is likely that this difference will be even larger according to the presented cross sections. Finally, the yield of molybdenum is somewhere in-between copper and the heaviest elements considered here.

The choice of which material to use in a future beam dump will have to be deduced out of a number of properties beyond the yield of a certain material. For this purpose some relevant parameters are summarised for the most interesting elements in Table 3.5 as a future reference.

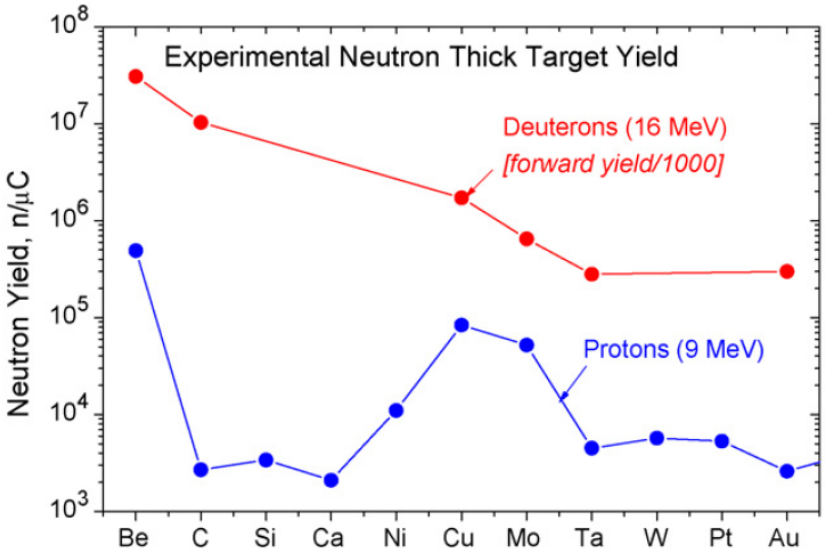

Figure 3.7: Experimentally measured neutron yields for two kind of projectiles, protons (9 MeV) and deuterons (16 MeV).[86]

The parameters include the density, Q-value, melting point, thermal conductivity, electrical resistivity, Brinell hardness and cost. Their importance will be briefly introduced in the following. A final evaluation would benefit from including simulations of the thermal and stress evolution, as well as simulations of the activation and required shielding.

,

Table 3.5: Density, thermal conductivity, electrical resistivity (@20°), Brinell hardness and cost for the candidate dump materials. The cost in £/g is calculated from the value of 100 g of powder, except for gold which was calculated from the found value of 2 g of powder. Values obtained from [36], [90] and [91].

	ρ	Q	Melting Point	Thermal Conductivity	Electrical Resitivity	Brinell Hardness	Cost
Cu	8.96	6.7	1083	401	16.78	520	0.90
Mo	10.28	5.2	2622	138	53.4	1340	1.33
Ta	16.69	4.9	3017	57.5	131	441-1224	4.21
W	19.25	3.8	3422	173	52.8	1960-2450	1.40
Au	19.30	4.9	1064	318	22.14	189	192
	[g/cm^3]	[MeV]	[°C]	[W/mK]	[nΩm]	[MPa]	[£/g]

The electrical conductivity (the inverse of the resistivity) is a parameter reflecting the ableness of a material to conduct a current. As of that, it is an important parameter for constructing a Faraday's cup. Materials which are considered as insulators have a resistivity well above the materials in Table 3.5 (10^{12}-10^{20} Ωm). A good conductor like copper has a resistivity of ∼17 nΩm. This value is very close to that of gold, and relatively close to the resistivity of tungsten and molybdenum. The resistivity of tantalum is worse, being a factor of 8 higher than the resistivity of copper. Nonetheless, as the resistivity of the candidate materials considered in Table 3.5 is of

relatively similar value, it is unlikely that this will be a deciding factor.

The melting point of a material is of importance to consider since the deposited energy of the ions will be converted into heat. The lower limit of the melting point will depend on the ion current and the intensity, the design of the beam dump and the cooling system. With a higher melting point the system is able to withstand higher intensity. This would also contribute to an increase in the safety regarding possible failures of the cooling system. Of the melting points in Table 3.5, gold and copper have the lowest values, surpassed by a factor of $\sim$3 by molybdenum, tantalum and tungsten. Related to the melting point is the thermal conductivity. With a high value of the thermal conductivity, the cooling of the material will be facilitated. Hence, as copper and gold have a higher thermal conductivity compared to molybdenum, tantalum and tungsten, they are more beneficial materials from this perspective. The specifics of the requirements of the melting point and a cooling system, as well as the developed stress, could be deduced from an analysis using a finite element model on a chosen beam dump design [92].

The Q-value of a reaction is of interest from the perspectives of shielding and activation. The less energetic neutrons that are produced, the less penetrating the neutrons will be. Less energetic neutrons amount to less activation in other parts of the beam dump as well as less shielding required. In Table 3.5, the Q-values of the (d,n)-reaction are given. The values correspond to the highest value found for a non-radioactive isotope of a certain element. Of those, tungsten is the more beneficial material. Future simulations of the activation in the beam dump would give an estimation of the required shielding to lower the radiation below the hands-on limit. For tungsten, such a simulation and estimation was reported by [93] for projectiles of both H_2 and deuterons.

The Brinell hardness is reciprocally related to the workability of a material [88]. As the Brinell hardness of both copper and gold is relatively low, both materials are easier to machine. Hence, the hardness of molybdenum and specifically tungsten is to the disadvantage of these materials. For these two, special fabrication techniques might be required [94].

Chapter 4

Experimental Evaluation

This chapter is an experimental evaluation of materials found to be of interest during the theoretical evaluation in Chapter 3. The experiment includes measurements on the yield related to both target materials and beam dump materials, and measurements on the moderator efficiency. Also included is a demonstration of a coincidence measurement.

4.1 Equipment

4.1.1 Accelerator

At LIBAF a single-ended electrostatic pelletron accelerator is used to accelerate ions up to 3 MeV. Through an ion source located inside the pressure tank of the accelerator, ions of hydrogen, deuterium or helium can be created in the case of LIBAF. The ions are injected into the accelerator and passes a prefocus magnet before an analysis magnet is used to steer the ions to the macro- or the sub-micron beamline. For this experiment the macro beamline was used, where a vacuum pump keeps the pressure at 10^{-6} mbar. In the macro beamline, quadrupole magnets can focus/defocus the beam, thus controlling its size. The size of the beam can also be controlled by the opening/closing of slits at two positions in the beamline. If the slits are closed, the current is diminished. Throughout the beamline, four beam stops are positioned. Two of the beam stops are used to measure the current and two act as a visual help in guiding the beam through to the target chamber. The visual help originates from the fluorescing material of the beam stops which gives an indication of the current position of the beam. As the trajectories of the ions change with the chosen accelerator energy, this is an important aid in tuning the magnets/slits in order for the projectiles to reach the chamber.[95]

4.1.2 Detectors

Three different detectors were used during the measurements, two for neutrons and one for charged particles. One of the two neutron detectors, a plastic scintillator detector, was used to detect fast neutrons. In the following, it will therefore be referred to as the fast detector. The scintillator consists of a 7x7x8 cm^3 piece BC-408 plastic from Saint-Gobain[96]. It was

connected to a photomultiplier tube (PMT) supplied with 2100 V. The purpose of the second neutron detector was primarily to detect thermal neutrons and will thus be referred to as the thermal detector. A boron doped plastic scintillator was used connected to a PMT supplied with 1200 V. The third detector was a charged particle detector used to detect the recoil of charged particles created in the fusion reactions. Being a semiconductor device, it was reverse biased with 30 V. The charged particle detector was only used during the coincidence measurements.

4.1.3 Electronics

Different electronics were used in order to process the signals received from the detectors. The circuit diagram used is schematically illustrated in Figure 4.1. Included are devices like a PMT, an amplifier, a discriminator, a fan-in/out, a gate generator, a busy unit, a time-to-digital converter (TDC) and an analogue-to-digital converter (ADC). Based on [8], the devices and their use will be further explained in this section.

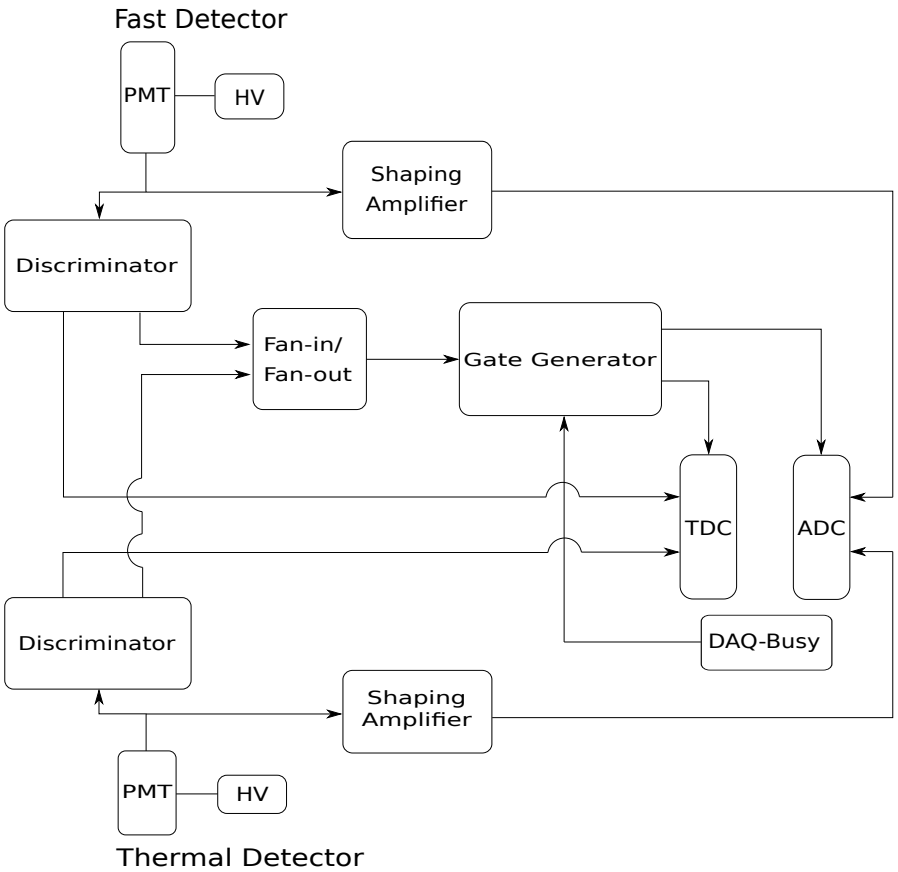

Figure 4.1: The circuit diagram of the electronics used during most of the measurements.

The interaction between neutrons and the plastic material of the neutron detector causes photons to be emitted (i.e. scintillations). In the PMT, which was connected to high voltage (HV), the scintillations in turn generate electrons in a process which ideally is proportional to the deposited energy. This process was briefly introduced in Chapter 2.4. To obtain a processable pulse signal,

these electrons are multiplied through a chain of dynodes. As a result of the amplification, a pulse signal is obtained which is large enough to be easily processed. In Figure 4.1, it is seen that the incoming signal from the PMT was connected to a splitter. During the experiment, the signal from the PMT was strong enough to allow the use of an analogue pulse splitter.

One of the outgoing signals from the splitter was connected to a shaping amplifier with a twofold function. As suggested by its name, one of the functions of the device is to amplify a received signal. Secondly, the amplifier can reshape the signal to avoid the effects of pile-up and for optimisation of the signal to noise ratio [8]. Pile-up is the effect where a signal is added on top of an earlier signal. The problem with pile-up will occur if the earlier signal has a long tail and a new signal arrives before the first signal has decayed. Using a unipolar output, the signal was lead onward from the amplifier to the ADC.

The second of the two identical signals is lead through a discriminator. The discriminator creates a logic signal if the incoming pulse signal is over a set threshold. The threshold prevents the system to be triggered on unwanted noise from the PMT. The triggering of the signal was performed using the leading-edge technique.

During the experiment, two logical signals were generated at the discriminator. One of the signals was connected to a Logic Fan-in/out unit. In the case of these measurements, the Fan-in only acted as a node point for the different detectors, without using its function of algebraic summation of the incoming signals. The signal from the logic fan-in/out was only continued to one other device, the gate generator.

A gate generator can be triggered to send out logical gate pulses of different width. The gate pulse can in turn allow for the collection of data during the set amount of time corresponding to the width of the pulse. This is accomplished by connecting the signal to an ADC and a TDC. As seen in Figure 4.1, a DAQ-Busy is also connected to the gate generator. The data acquisition busy unit blocks the generation of a gate if the data acquiring system is busy. The down-time corresponds to the time when the system (ADC, TDC) is occupied digitising the signal and recording it to the computer. During this time, the system does not accept new data. The time during which the system was offline is recorded and mirrored in the acquired data as the live time of the system.

The second signal from the discriminator was connected directly to the TDC, which, if the gate allows for collection of data, digitises the received logic signal (i.e. its time).

The ADC turns an analogue pulse into a digital signal. The data is then collected by a computer. It is the digitising of the pulse in the ADC, as well as the collecting of the data in the computer, which is the bottleneck that the busy-unit receives its feedback from. This information is communicated by the busy-unit to the gate generator.

A modification to the electronics was implemented for coincidence measurements to include the charged particle detector. The circuit diagram can be seen in Figure 4.2. Both the PMT:s were connected as in Figure 4.1. The triggering of the gate during the coincidence measurements was, again, performed with both the fast and the thermal neutron detector. Even though the gate was triggered by both neutron detectors, coincidences will primary be found in the fast detector because of the longer moderation process of thermal neutrons. Occasionally, however, a fast neutron might also give a coincidence in the thermal detector.

Close to the macro chamber, the detector was connected to a preamplifier, acting as an amplifier for a weak signal. Since the amplification process also results in the amplification of noise, it is beneficial if the preamplifier is connected in close proximity to the detector. After the

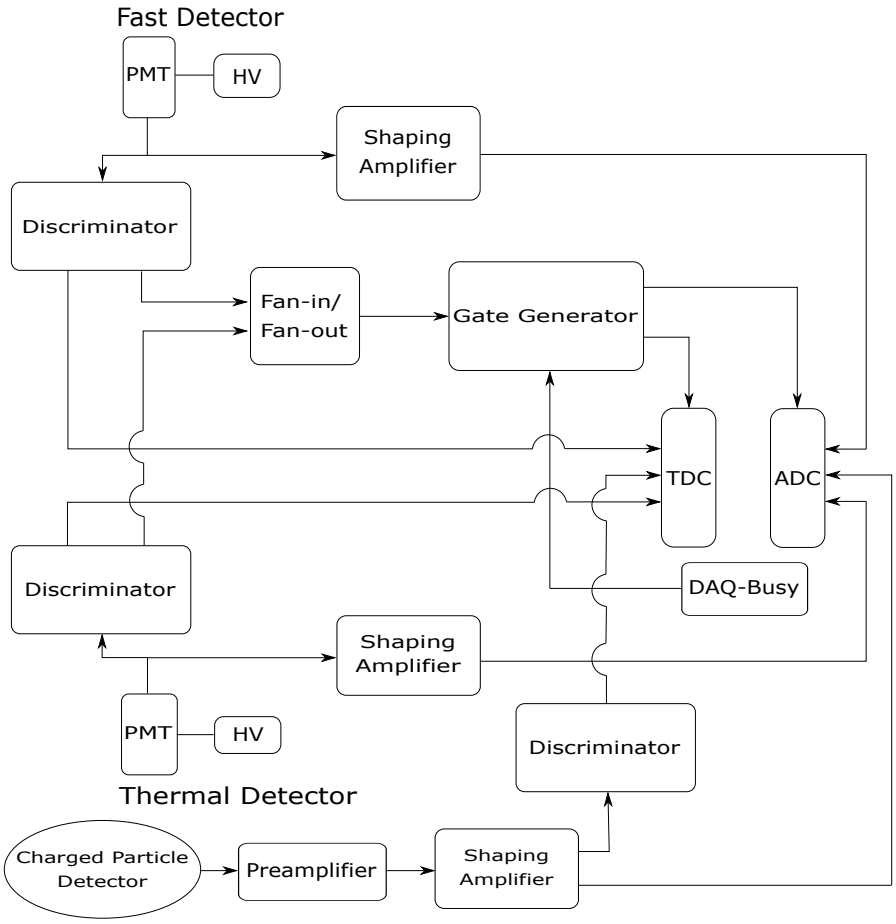

Figure 4.2: The circuit diagram of the electronics used during the coincidence measurements.

preamplifier, the signal was connected to a shaping amplifier, before being split into two identical signals. One of the split signals was connected to a discriminator. If a logic pulse is to be triggered, it is then lead onward to the TDC. The second signal is connected to the ADC. If a gate has been generated, the data from the charged particle detector is digitised and collected in the computer.

4.2 Experimental Setup

Figure 4.3 is a photograph of the general setup for the experiment. Two neutron detectors were positioned outside the macro chamber, each being covered with lead blocks on the front and on the sides. The detector in the foreground of Figure 4.3 is the fast neutron detector. A second detector is hidden inside the lead blocks further back in Figure 4.3. It is the boron doped detector used for thermal neutrons. In the figure, a block of plastic moderator material is also discernible. It was kept in front of the thermal detector during most of the experiments, except when the different moderator materials were tried. The dark blanket was used to cover

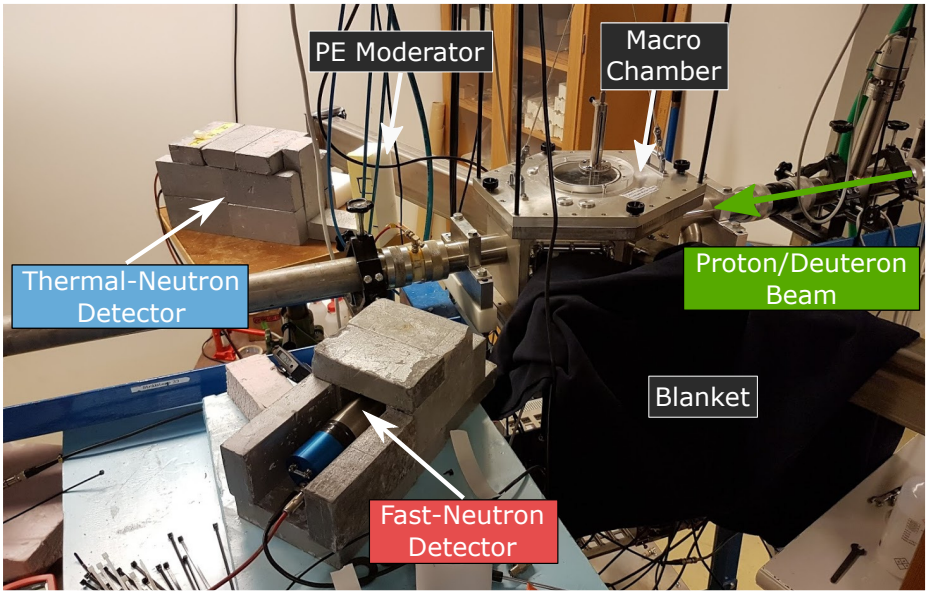

Figure 4.3: The experimental setup outside the macro chamber.

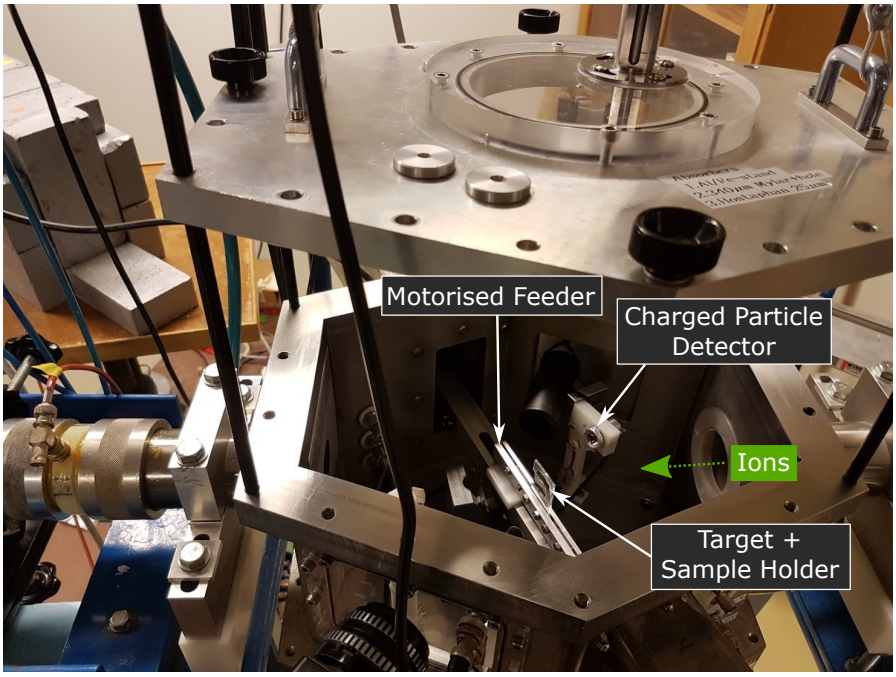

Figure 4.4: A close-up of the experimental setup inside the macro chamber.

the macro chamber during the coincidence measurements, in order to reduce the noise from light in the charged particle detector.

Figure 4.4 is a close up of the macro chamber, showing both a target sample, the motorised feeder and the charged particle detector. The target samples were placed in the motorised feeder which was steerable from the control room of the accelerator. Each target was put on a sample holder of glass, before being mounted in the feeder. Behind the target, the beamline continues into a beam dump which, if no target blocks the beam, can measure the current. However, since thick targets were used, and because of a malfunctional beam stop, the current was only measurable in-between each measurement.

A schematic illustration of the setup is shown in Figure 4.5. The fast detector was placed 55 cm from the middle of the target in the forward direction at an angle of 42° relative to the ion beam. On the right side to the direction of the ion beam, the thermal detector was placed 60.5 cm away from the middle of the target at an angle of 33°. Inside the Macro Chamber, sample holders with the target materials were placed on a 23° angle relative to the ion beam. Also inside the chamber, the charged particle detector was placed in the backward direction from the target, 18° relative to the ion beam. The setup was generally unchanged until the last three measurements, before which only temporal modifications to the setup were made in order in order to measure the effect of moderators. Thus, a number of blocks of different materials were added in front of the thermal detector. After the moderator measurements, these blocks were removed.

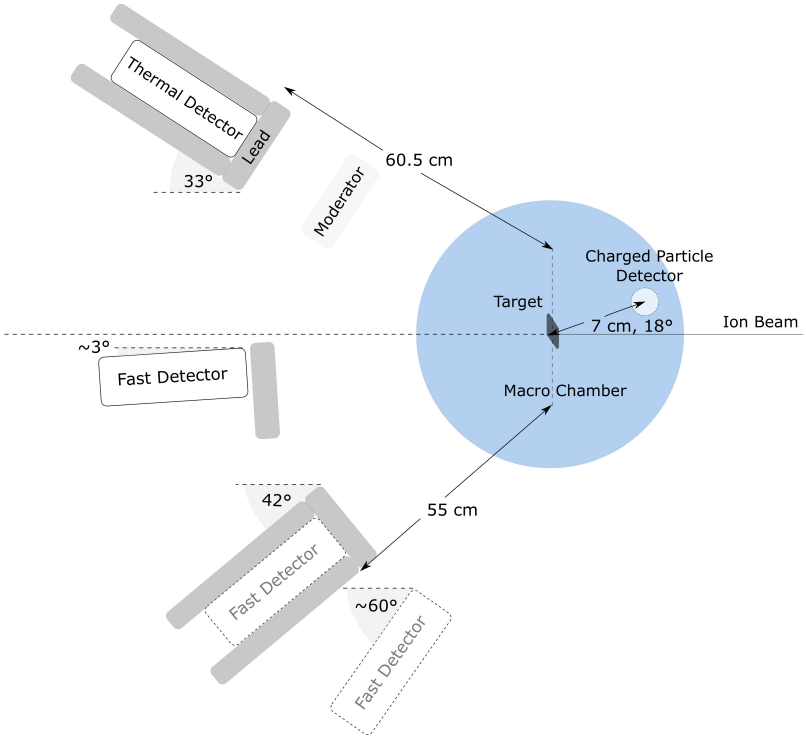

Figure 4.5: A schematic illustration of the experimental setup. Three representations of the fast detector are seen, indicating the different positions for the detector during the coincidence measurements. The standard position used for most of the experiments has been indicated by the arrow from the target inside the macro chamber.

The target, moderator and dump materials used during the experiments were primarily those of most interest from Chapter 3.2, 3.3 and 3.4. Beyond those, some additional materials where measured upon. The following thick target materials were included: deuterated plastics, titanium tritide, lithium fluoride, beryllium and carbon. As the facility was short on hydrogen gas, only lithium fluoride was tested using proton projectiles. This test was performed using three different projectile energies: 1.75 MeV, 2.1 MeV and 2.3 MeV. Otherwise, most of the target materials were bombarded with deuteron projectiles of 1.8 MeV and 2.2 MeV. The tested moderator materials included blocks of food graded plastics of polyethylene (20±0.2 cm, 10±0.2 cm, 5±0.2 cm), glass and plastic bottles filled with D_2O (d=7.5±0.6 cm, h=9.7±2.3 cm) and blocks of lead (18±2.2 cm, 9±1.2 cm, 4.5±0.6 cm). The neutrons used for the moderator measurements were produced using 2.2 MeV deuterons impinging on the LiF-target. The thick dump materials tested during the experiment included carbon, steel, aluminium, titanium, nickel, copper, tantalum and tungsten carbide. Most of the dump materials were tested using E_d=2.2 MeV. For carbon and tantalum, an additional measurement was performed using 1.8 MeV deuterons.

4.3 Calibration of the energy spectrum

4.3.1 ^{60}Co - daily calibration

The experimental work was primary performed over four consecutive days. In order to compare the results obtained from different days, a calibration of the fast detector was performed each day using a radioactive source of ^{60}Co. The decay scheme of the source is seen in Figure 4.6. To 99.88 %, the decay occurs through β-decay to the third excited state of ^{60}Ni. In turn, the deexcitation of ^{60}Ni to the ground state occurs through emission of two γ-quanta of 1.1735 MeV and 1.3325 MeV.

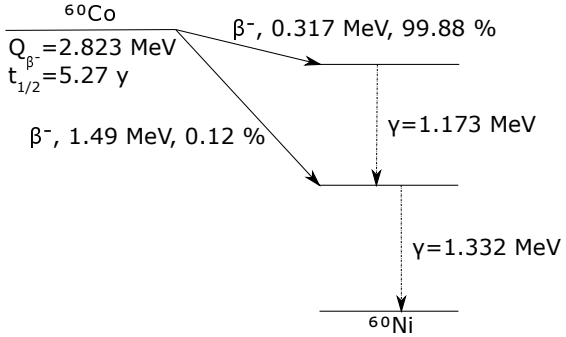

Figure 4.6: The decay scheme of ^{60}Co to ^{60}Ni and the subsequent γ-cascade.[45]

In Figure 4.7, a presentation is given of the spectra from the measurement of ^{60}Co for three different experimental days: two to four. The spectrum from the first day of the experiment is not included, as during this day, the only projectiles used were protons impinging on a single LiF-target. Since the reaction p-Li has a high threshold for neutron production, the kinetic energy of the produced neutrons is below the fast category. With the given setup, these neutrons are unresolved in the fast detector. Hence, only the thermal detector is of relevance for these measurements.

The calibration point for the spectra in Figure 4.7 is the Compton edge. For all of the relevant

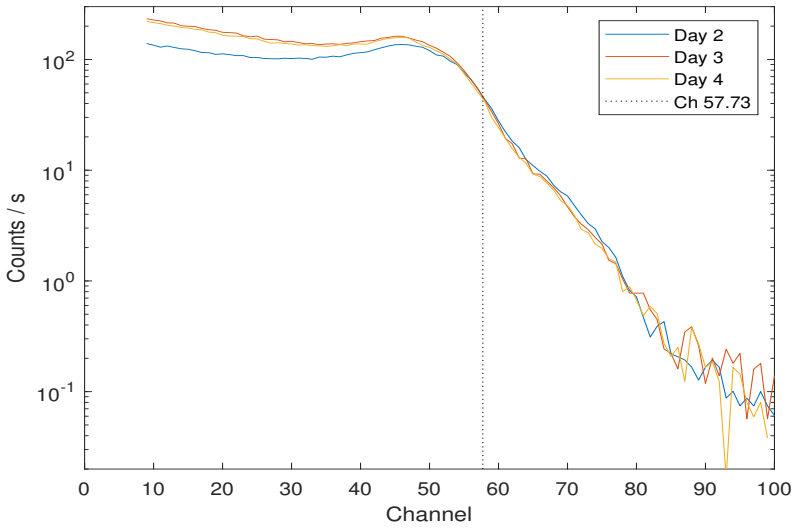

Figure 4.7: The fast detector spectra from the calibration measurements with ^{60}Co on days 2 to 4. The Compton edge at Channel 57.73±0.149 was identified using the derivative of the spectra and by taking the channel number at 50% of that value.

days, the Compton edge was found to be in vicinity of the same channel number (57.73±0.149). Thus, the measurements made are comparable without further modification except for the propagation of the uncertainty in the channel number. The method of selecting these channels will be highlighted in a following section. The difference in amplitude of the maximums before the Compton edge is irrelevant for the calibration. It is merely the result of where the target is placed, causing more or less γ-radiation to reach the detector. The maximum possible energy transferred in the detection process will be unchanged.

4.3.2 Calibration of fast detector

Figure 4.8 presents the spectra obtained from the fast detector when bombarding different target materials with deuterons. The reactions therein were used to calibrate the fast detector. It is possible to calibrate the detector since the maximum kinetic energy of the neutrons produced at a certain angle is well known for the different reactions. These energies are found from Equation 2.17 and are included in the legend of Figure 4.8. More calibration points were obtained as the impinging deuterons were run at two different energies for most of the target materials. The spectra obtained from the deuterated plastic were modified. A deuterated plastic material will inevitably result in a mixed spectrum of both the d-D- and d-C-reactions. As the d-C-reaction was measured upon separately in the carbon target, this data could be used to remove the d-C-spectrum from the spectrum obtained using the deuterated plastic (negative values put to zero). The modified spectrum is denoted dD-dC in Figure 4.8.

To relate the maximum kinetic energy of the neutrons to a channel number, the point in the spectrum where the number of normalised counts began to decrease at a high rate were identified using the derivative. This point will be referenced to as the "edge" in the following discussion. As has been discussed in Chapter 2.4, the limited resolution of the detector causes a smearing

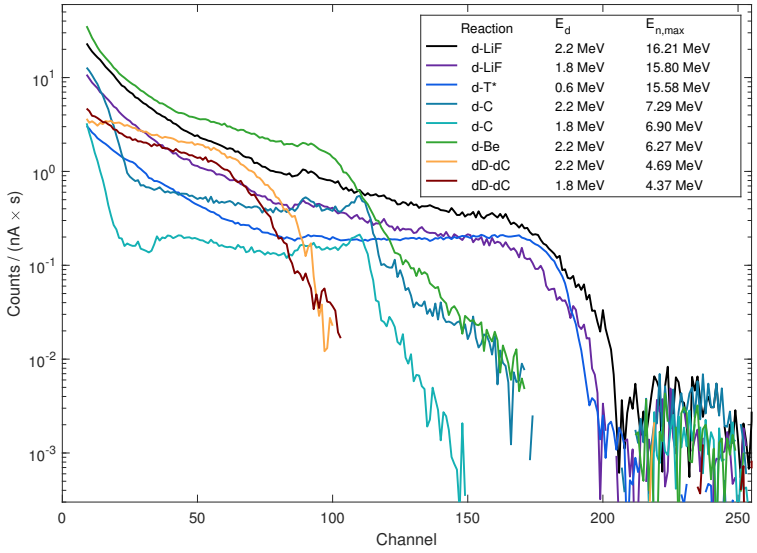

Figure 4.8: Spectra of the reactions used to calibrate the fast detector. The data of d-T has been scaled with the live time and an arbitrary current (80 nA). The dD-dC is the spectrum remaining after the d-C spectrum was removed from the data of the deuterated plastic with negative values put to zero. E_d states the energy of the incoming deuterons. $E_{n,max}$ represents the maximum neutron energy at an angle of 42° calculated from Equation 2.17.

of the detected neutron energy. Thus, a decision was made to relate the channel number, where the number of counts had been reduced by 50% from the edge, to the highest kinetic energy of the neutrons from the appropriate reaction. Due to limited statistics, it was necessary to re-bin the data to between 1/32 or 1/128 of the original channels for the method to work. This was accounted for in the error propagation.

The relationship between the maximum energy of the neutrons and the channel number is plotted in Figure 4.9. Two possible calibration curves are given, one linear and one quadratic. Both the linear and the quadratic fit involves the assumption of relating the first channel to zero energy. Visually, the quadratic fit seems to be the more appealing choice. If a χ^2-test is performed, the results are 1.97 and 0.98 for the linear and quadratic fit respectively, i.e. the quadratic function gives a better fit to the given data. According to the findings of [97] and [98], a nonlinear fit is motivated to use for neutrons, reflecting the non-linear response of the detector to lower energetic recoil protons [8]. For an improved fit, it would be beneficial to include more data points, especially at lower energies. In light of the stated literature, specifically [97], a quadratic fit will be used to calibrate the channels to energy in the following.

4.3.3 Calibration of the charged particle detector

Figure 4.10 is a calibration plot for the charged particle detector used during the coincidence measurements. The calibration was performed using a ^{228}Th source. A Gaussian function was fitted to each peak of the obtained spectrum, to find the channel number of its centroid and its

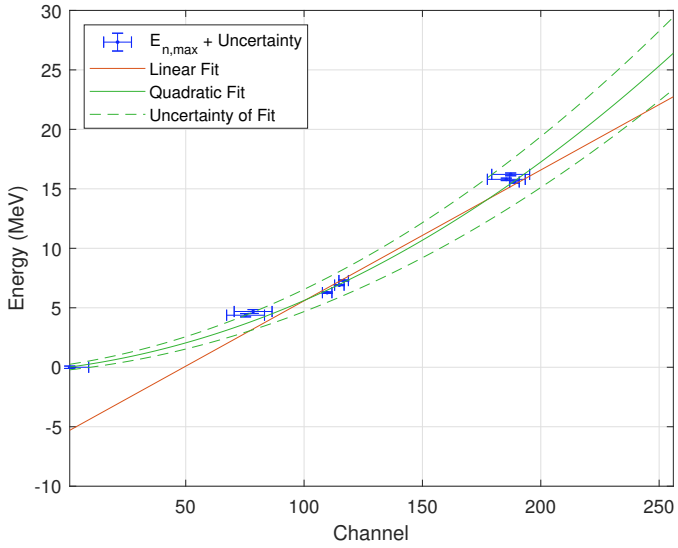

Figure 4.9: Energy calibration plot for the fast detector. The maximum neutron energy, $E_{n,max}$, of the reactions shown in Figure 4.8 is plotted as a function of the related channel number. Errorbars of the uncertainty in channel number and energy have also been included for each data point. The continuous lines represents the linear and the quadratic calibration functions. Dashed lines are the uncertainties of the quadratic fit.

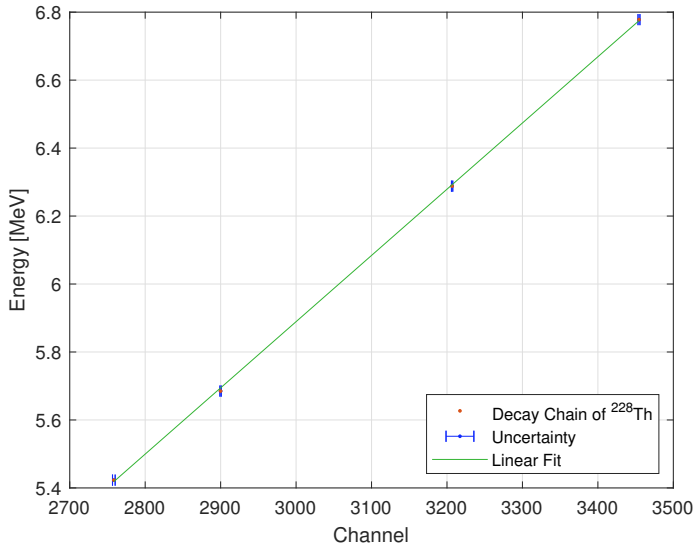

Figure 4.10: Energy calibration plot for the charged particle detector with a linear fit. The energy of the identified peaks of the decay chain of ^{228}Th has been plotted to the channel number found from fitting a Gaussian to each peak. The uncertainties of the channel numbers are derived from the 68.2% confidence interval of the Gaussian fit. The calibration energies as well as the related channels are found in Table 4.1.

related uncertainty. Through the well known decay chain of ^{228}Th, the channels were related to energy. A linear fit was performed on the channel numbers and the related energies given in Table 4.1. A χ^2-test resulted in a value of 0.014, indicating that the linear fit is good, being within one standard deviation of the measured data points. This function will thus be used to calibrate the charged particle detector during the coincidence measurements.

Table 4.1: The calibration energies of the α:s from the decay chain of ^{228}Th.[45]

Mother	Energy (MeV)	Channel
^{228}Th	5.423	2758.45±1.76
^{224}Ra	5.685	2899.92±0.88
^{220}Rn	6.288	3206.80±0.86
^{216}Po	6.778	3454.45±1.26

4.4 Results and discussion

The calibrated fast neutron spectra are presented in Figure 4.11. The light grey/white coloured area indicates the region of neutron energies used for the calibration. The number of counts has been normalised to the current and the active time of the system, i.e. the incoming charge, and is thus presented as the number of counts/(nA·s).

The spectra show generally a good reflection of the remarks from Chapter 2.4. Both the nonlinearity of the scintillator and the limited resolution of the detector at higher energies are visible. As is seen in Figure 4.11, the spectra do not entirely cease at the stated maximum neutron energy. A reason for this might be because of pile-ups in the counting system. Another possible explanation is because of contamination from γ-radiation.

The calibration performed with the ^{60}Co-sample is of importance when the possible contamination of γ-radiation is considered. In Figure 4.6, the maximum energy of the γ:s from the decaying source was given as 1.332 MeV. From the discussion in [99], it is found that such a photon transfers a maximum of 1.118 MeV through Compton scattering with the atomic electrons. In accordance with the method used for deciding the channel number related to the maximum energy of a neutron, the Compton edges of the 1.118 MeV γ:s in Figure 4.7, were found at channel 57.73. A quenching factor is involved when comparing the deposited energy of the electrons to that of the recoiling protons in the scintillator [8]. Hence, two different energy scales emerge, one for γ-radiation and one for neutrons. By translating the original channel number of the Compton edge of the γ through the quadratic fitting function, the corresponding neutron energy is found to be 2.50 MeV. In other words, the energy of a neutron which is detected in the same channel as the known γ-quanta, is in fact higher than what might initially be thought. Accordingly, the quenching factor is found to be close to a factor 2.24 at this energy. If a constant quenching factor is assumed, an axis of the γ-energy can be deduced from the quadratic fitting function. The axis is included on the top in Figure 4.11, giving an apprehension of possibly involved γ-radiation.

It was mentioned in Chapter 3.2 that the involved reactions also produces γ-radiation. Even though high energy γ:s in the 15 MeV range are possible, these reactions were found to be improbable. γ:s in the range of 7-8 MeV, and below, are more common. If this is related to the spectra in Figure 4.11, it is not improbable that the non-zero spectra above the maximum neutron energies are influenced by the generated γ-radiation. Especially so since the γ:s above the

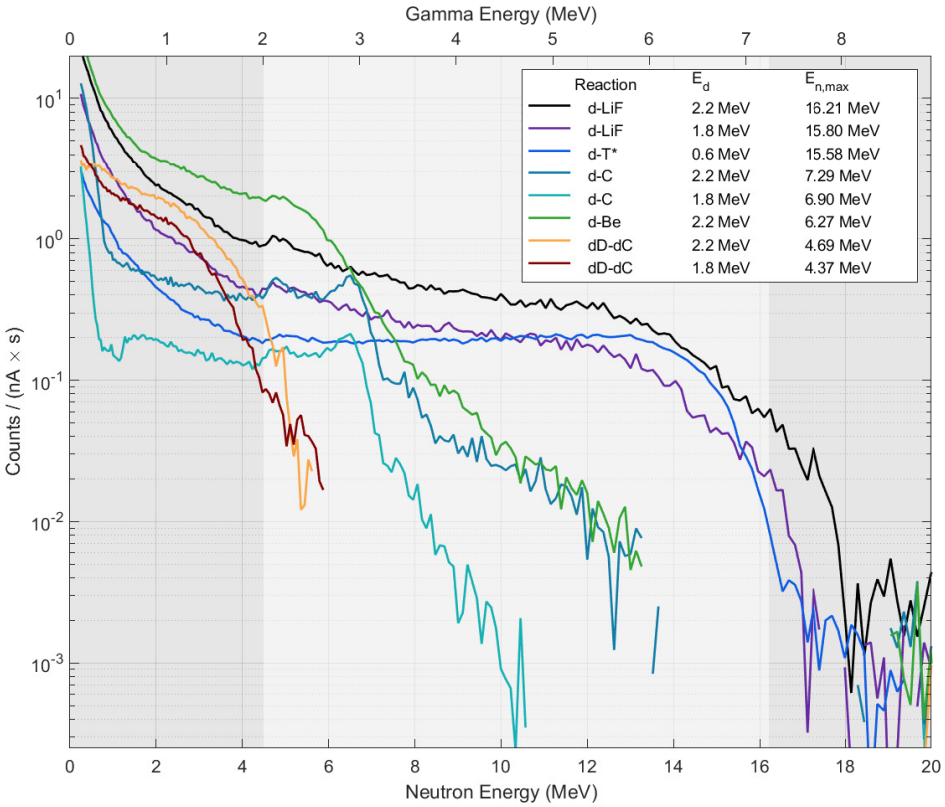

Figure 4.11: Calibrated spectra of possible target materials. The light grey/white area indicates the region of energies which was utilised for the calibration. The maximum kinetic energy of the neutron for each target material is presented at an angle of 42°. The d-T-reaction has been scaled down with an arbitrary factor. The axis included on the top in Figure 4.11 gives an apprehension of possibly involved γ-radiation.

highest detected neutron energies are in the 7-8 MeV-range (if the quenching factor is constant).

As was previously highlighted in Figure 4.5, blocks of lead were placed around the detectors in order to shield as much as possible of the γ-radiation. The transmittance of γ through matter decreases exponentially with the thickness of the material, i.e.

$$I(x) = I_0 e^{(-\mu x)}, \tag{4.1}$$

where I(x) is the intensity a distance x into the material, I_0 is the original intensity and μ is the mass attenuation coefficient[8]. Since μ is material and energy dependant, the attenuation of different γ-energies was investigated after passing through 5 cm of lead. The mass attenuation coefficients were obtained from [100]. Figure 4.12 presents the resulting absorption as a function of the thickness of the lead block. It is evident that the given setup should block at least 90% of the incoming γ-radiation. Thus, because of the high attenuation of γ-radiation in lead, as seen in Figure 4.12, the further analysis assumes its impact as small on the obtained result.

Two neutron detectors were used during the experiment. Initially, the discussion above has been

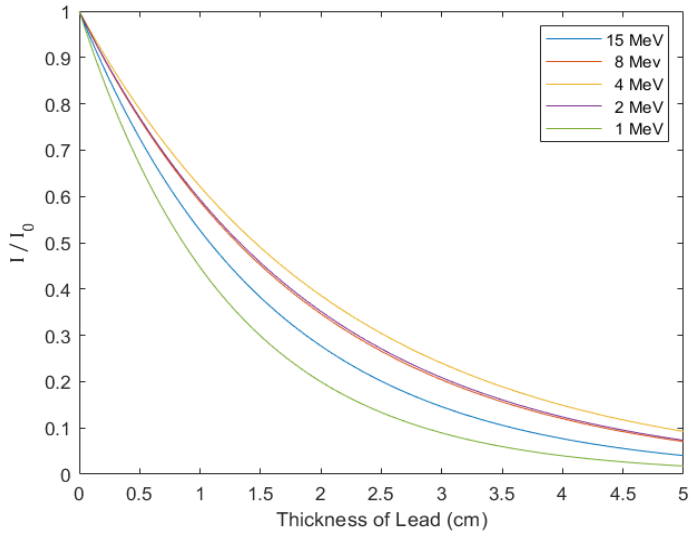

Figure 4.12: Attenuation of γ in lead, calculated from Equation 4.1.

related to the fast neutron detector. Figure 4.13 shows two typical spectra obtained from the second detector used for thermal neutrons. The spectra originates from the d-D reaction at two different deuteron energies, 1.8 MeV and 2.2 MeV. Herein, the primary areas of interest is the region surrounding the maximums just above channel 100. As discussed in Chapter 2.4, this well defined area corresponds to the detection of ^{10}B(n,α)^{7}Li. Since this detector also was surrounded with blocks of lead, the analysis related to the thermal neutrons will be performed with the same assumption of low γ-contamination used previously for the analysis of the spectra from the fast detector.

4.4.1 Quantification of results

In order to quantify the results from the fast detector related to the measurements on the possible target materials in Figure 4.11, an integration of the number of counts was performed from the channel number corresponding to the maximum energy of the neutrons down to 40% of the maximum energy. The value was chosen to limit the inclusion of the non linear region at lower energies in Figure 4.11. The uncertainties from the quadratic fit in Figure 4.9 was also integrated in a similar fashion.

For the spectra related to the thermal detector, the quantification process was taken in two steps. To begin with, a Gaussian function was fitted on top of an exponential background to the spectra from the different reactions The fit was made in MatLab using a non-linear least-squares method with the robust bisquare option and with included weights. An example of such a fit is included in Figure 4.14. This particular fit corresponds to the spectrum of the d-D reaction for E_d=2.2 MeV from Figure 4.13. The number of counts was found by calculating the area under the Gaussian using the coefficients obtained from the fit. The related uncertainty was calculated in the same way using the standard deviation for the found value of the different parameters.

A compilation of the results from the quantification of the spectra normalised to the charge

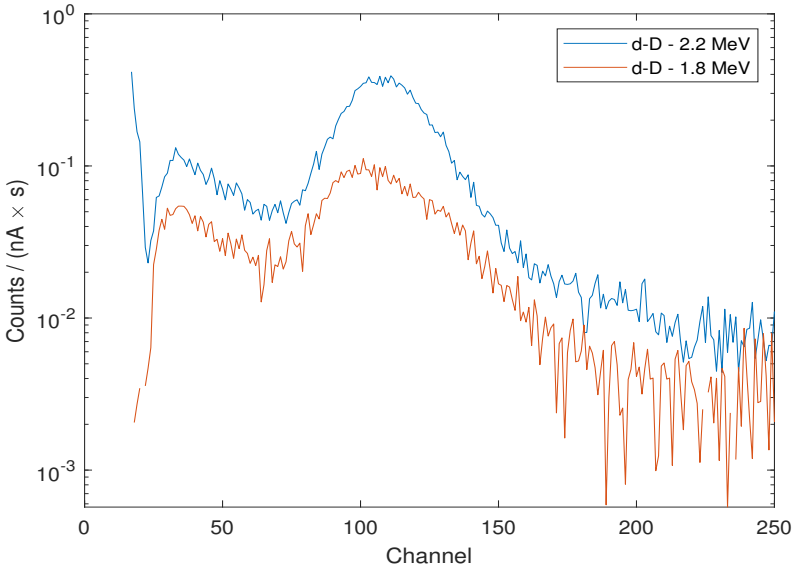

Figure 4.13: Representations of typical spectra from the thermal detector used in the experiment. Both spectra are from the d-D reaction, the blue for E_d=2.2 MeV and the red for E_d=1.8 MeV.

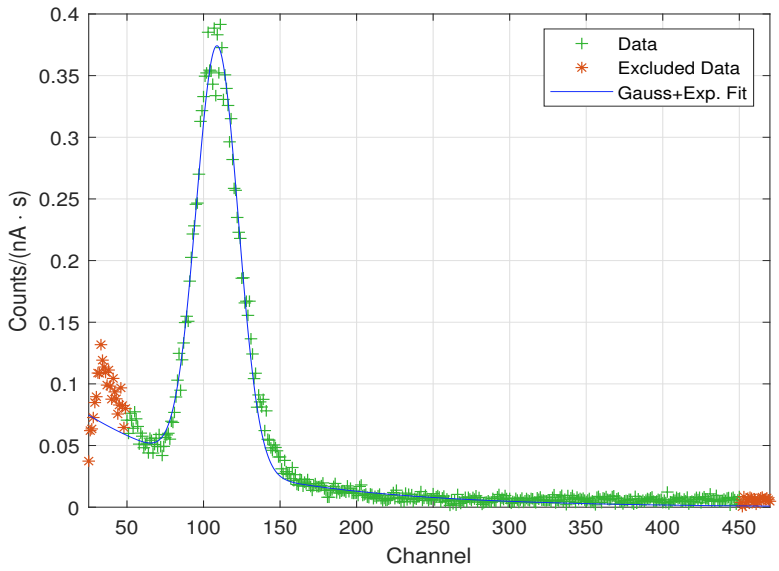

Figure 4.14: The fit of a Gaussian with an exponential background on the data of the thermal detector. This plot shows the data from the d-D reaction with E_d=2.2 MeV. The green dots corresponds to the data used for the fit. The red stars are excluded data.

is presented in Figure 4.15, where the fast detector is represented by the red column and the thermal detector by the blue column. The d-T-reaction, which was one of the reactions used for the calibration of the fast detector, has been excluded because of the lack of data on the current used for this reaction. The white coloured bars in the figure are related to a relative scaling of the fast detector which is soon to be discussed.

It is of importance to stress that the results presented in Figure 4.15 are not an absolute measure of the produced quantity of neutrons for each reaction. Rather, for the thermal detector, it is to be seen as an indicator of the number of obtained thermal neutrons for the given unoptimised setup. Once a certain reaction is chosen as the future neutron source, the result could undoubtedly be optimised by, e.g., improving the moderation geometry through Monte Carlo-simulations. Moreover, for the fast detector, the relative scaling in Figure 4.15 was performed in order to introduce an approximative correction for the energy dependant cross section of elastic scattering on hydrogen atoms. The values of the correction were obtained from [32] under the assumption of isotropic scattering. This assumption was confirmed in data from [32], specifically for the more energetic neutrons. The correction is also based on the assumption of a small scintillator compared to the mean free path of the neutrons. Without this assumption, all of the energy would have a high probability of being deposited. The relative scaling of the results was made relative to the cross section related with the most energetic neutrons, i.e. those of the d-Li-reaction with E_d=2.2 MeV. The scaling was only performed on the compilation from the fast detector.

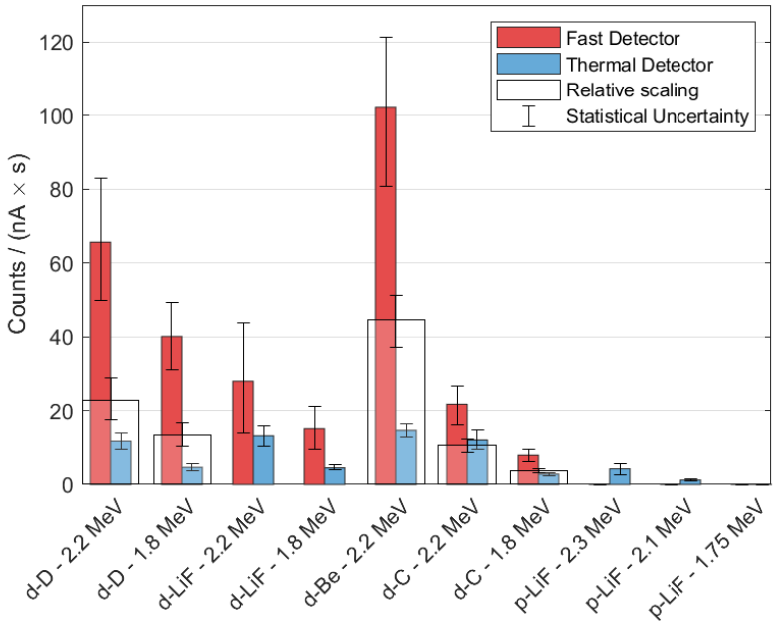

Figure 4.15: A compilation of the counts in the fast (red) and thermal (blue) detector for different targets. The counts have been normalised to the charge. The white coloured bars include a relative scaling of the counts from the fast detector. The scaling originates from the energy dependant cross section for elastic scattering of neutrons on hydrogen divided with the corresponding number for the fastest neutrons (i.e. that from the d-LiF-reaction at E_d=2.2 MeV). On the pinnacle of each bar, the propagated uncertainty of the model, the charge and the number of counts in each channel has been plotted.

The error bars included on the pinnacle of each bar in Figure 4.15 represents the propagated uncertainties of: the model, the current, the live time of the system and the detected number of counts in each channel. Normally, the current is repeatedly measured after a certain time interval during the whole measurement. Because of a malfunctioning deflector, this was not possible. Rather, the read-out was performed from the instrument panel before and after each measurement. For this purpose, the uncertainty of the read-out of the current was approximated to 0.5 nA and the uncertainty of the live time to 0.5 s. The influence on the size of the errorbars of the uncertainty of the calibration in the fast detector is up to 36% of its size.

4.4.1.1 The fast detector

The comparison of the data for E_d=2.2 MeV in Figure 4.15, indicates that the production of faster neutrons is most effective for deuterons impinging upon the beryllium target. This reaction results in a factor of 1.6 more counts than what is obtained using the deuterated plastic. With the scaling taken into account, the same difference is close to a factor of 2. Comparing d-Be with d-LiF, the difference is around a factor of 3.7. With the scaling, the difference is a factor of 1.6. The number of counts of the deuterated target is around 2.3 times higher than that of the lithium fluoride. Note that the spectrum of the deuterated target has been summarised using the full spectra (without removing the influence of the carbon spectrum) and that the summation proceeded from the maximum neutron energy related to the fusion of deuterium with deuterium. If the relative scaling is taken into account, the model used is inadequate to distinguish between the counts of the deuterated plastic and the lithium fluoride. The counts from the carbon target is lower than those from the beryllium and deuterated targets. When the carbon target is compared with the lithium fluoride, the unscaled number of counts cannot be distinguished from that of the lithium fluoride. With the scaling however, the number of counts of d-C is a factor 2.6 less compared to d-LiF.

The highest count rate in the fast detector was obtained from the d-Be-reaction. From the calculations presented in Table 3.3, the result is not unexpected. In the table, the calculations gave that a pure lithium target would produce more neutrons than a beryllium target. If a LiD-target was used however, the pure beryllium target was found to be the better producer. When comparing the Be- with the LiF-target used in the experiment, it is of importance to note the atomic density of the targets. The LiF-target, consisting of both lithium and fluoride, has an atomic density of $9.9{\cdot}10^{28}$ atoms/m^3 compared to $1.23{\cdot}10^{29}$ atoms/m^3 for ^{9}Be [28]. More importantly is that the LiF-target consists of 50% lithium atoms, of which about 90% pertains to the ^{7}Li-isotope. Hence, the number of target atoms that a deuteron has the potential to encounter during its deacceleration in a beryllium target, is at least a factor of 3 more compared to the ^{7}Li in the LiF-target. The difference in the detected number of neutrons (about a factor 3.7) is naturally related to the difference in target atom density, especially so as the cross section is relatively similar for ^{7}Li and ^{9}Be (see Figure 3.1).

The counts from the beryllium target was more than 50 % higher than that of the deuterated plastic. The calculated difference from Table 3.3 indicated that a beryllium target would produce close to 3.4 times more neutrons. With the relative scaling in Figure 4.15, the difference was close to a factor of 2. The inconsistency could disclose an error pertaining to the approximation of the calculated yield. In the calculation, the part related to neutron production from carbon was disregarded. The number of calculated neutrons from the deuterated plastic would be higher if the contribution from carbon atoms was included.

Comparing beryllium and carbon, the number of counts was a factor 4.7 higher for the beryllium

target (4.2 with the relative scaling). From the calculations in Table 3.3, the difference in the number of produced neutrons was a factor 3.3 to the advantage of the beryllium target. This discrepancy might be an indication of an important factor which is not to be overlooked when the carbon spectrum is analysed. The maximum kinetic energy of the neutrons from the d-^{13}C-reaction is 7.29 MeV and the isotopic abundance of carbon is about 99% ^{12}C and 1% ^{13}C. Since d-^{12}C is a threshold reaction, the maximum energy of the neutrons is below 2 MeV for an accelerator potential of 2.2 MeV. This value falls into the non-linear region which is not included in the summation of the counts in the detector. Naturally, this will result in a relatively high loss of the potential number of counts. Interestingly, however, the number of counts in the thermal detector from the beryllium and carbon targets is indistinguishable with the given model.

The beryllium target was only used for deuterons with an energy of 2.2 MeV. For the other targets, a second run at E_d=1.8 MeV was performed. At this projectile energy, both the deuterated plastic, lithium fluoride and carbon targets indicated a decrease in the number of counts compared to that of the higher projectile energy. Naturally, this is to be expected. The factor of difference between the lithium fluoride and the deuterated plastic was found to be a factor of 2.3 for the more energetic projectile and 2.6 for the less energetic projectile. The reason for this increase is not entirely clear. It could be related to an increase of production of neutrons with lower energy than the limit of the lower bound of integration (40% of $E_{n,max}$), if excited levels of the compound nucleus related to the d-^{7}Li-reaction are reached for the more energetic projectiles.

For a comparison of the measured counts with the expected calculated yield in Table 3.3, two things are of importance to consider: the detector efficiency and the surface area of the scintillator relative to the area where the neutrons are emitted (geometrical efficiency). For plastic scintillators for neutrons in the MeV-range, a rule of thumb is that the detector efficiency ϵ is 1% per cm of scintillator material [101]. For the scintillator used, this would amount to ϵ=0.08. The use of the same value of the detector efficiency for all reactions is overlooking the fact that the maximum energy of the neutrons of the different reactions vary with more than 10 MeV. If the emission of neutrons is approximated as being isotropic, the area of the detector over the area of the emission gives a factor of 0.0013. The approximated yields from the measured number of counts are found by dividing the measured counts by the detector efficiency and the geometrical efficiency. To facilitate the comparison to the calculated yields, the experimental yields were scaled from nA to μA. The result of scaling the experimental yields is given in Table 4.2, in which it can be seen that the experimental values fall well within an order of magnitude of the theoretical.

Table 4.2: The calculated yield for E_d=2.5 MeV and the experimental yield integrated from 40% of $E_{n,max}$ to $E_{n,max}$. The value was thereafter normalised to the detector efficiency and the geometrical efficiency, before being extrapolated from nA to μA to facilitate the comparison between this and the calculated yield.

Reaction	d-D	d-D	d-^{7}Li	d-^{7}Li	d-^{9}Be	d-C	d-C
Calc. Yield [n/μC]	2.8E8	-	3.5E8	-	9.1E8	2.7E8	-
Exp. Yield [n/μC]	6.4E8	3.9E8	2.7E8	1.5E8	9.9E8	2.1E8	0.8E8
E_d [MeV]	2.2	1.8	2.2	1.8	2.2	2.2	1.8

4.4.1.2 The thermal detector

Because of the uncertainties related to the model used and the charge, it is nearly impossible to discern between number of counts in the thermal detector in Figure 4.15 for a specific projectile energy. It is however interesting to note the relative change between the fast counts and the thermal counts when comparing the same target at different E_d. The difference of the thermal counts in the deuterated plastic was a factor of 2.5 and of the fast a factor of 1.6. For the lithium fluoride, a factor of 2.9 was found in the difference of the thermal counts and 1.8 in that of the fast detector. For the carbon target, the difference of thermal counts was a factor of 4.3 and of the fast counts a factor of 2.7. This deviation in the factor of difference between the two projectile energies will be further discussed in the following.

In Equation 3.7, it was previously shown that the d-^{12}C-reaction had a threshold of 0.328 MeV. In Equation 3.9, the ^{19}F(d,n)^{20}Ne was shown to have a positive Q-value of 10.6 MeV. However, the cross section for this reaction was relatively low. The threshold reaction producing ^{12}C+2α+n could possibly increase the yield of thermal neutrons. As reported, the magnitude of its cross section was not found. The neutron production of the reaction d-^{6}Li, has a Q-value of 3.4 MeV [40]. The cause for the increase of thermal neutrons in these two elements is thus hard to relate to the different compounds in the target. However, if a target surface has been oxidised, a possible explanation could be found. The threshold for neutron production for the d-^{16}O is 1.829 MeV, giving that the lower energetic neutrons would not be able to produce thermal neutrons from this reaction [40]. Deuterons of higher energy could, on the other hand, be involved in neutron production with ^{16}O with a cross section value of $\sim$0.15 b [32]. The explanation related to the oxidation of a surface is thus, possibly, only a viable explanation for the lithium fluoride, since the surface of a carbon material does not oxidise. The lithium fluoride target was analysed in a later study conducted at LIBAF [102]. Therein no significant levels of oxygen was found, thus disqualifying this possible explanation. For the carbon target material, it could also be thought that a low, but unknown, quantity of boron could be present. However, the Q-value for this reaction should not amount to the specific increase of thermal neutrons.

Another possible cause of the increase of thermal neutrons is if the higher energy projectiles overcome the threshold for neutron separation from an element. Of the considered elements, it is only ^{9}Be which has a low enough neutron separation energy of 1.66 MeV [45]. This target was only tested with one projectile energy, and it is therefore difficult to draw any further conclusion from this information. Additionally of interest concerning the neutron separation energy are the deuteron projectiles themselves having a separation energy of 2.225 MeV. The maximum projectile energy used was 2.2 MeV. Depending on the calibration of the machine, it is possible that the energy of the projectiles exceeded the separation energy, thus creating a lower energetic flow of neutrons. Two other explanations of the increase of thermal neutrons are mentioned in Chapter 3.1 related to d-^{7}Li and d-Be: threshold reactions and the density of excited levels. It is possible that these two explanations also extrapolate to the reactions of d-D and d-C.

In Figure 4.15, the compilation of the data from the p-LiF-reaction is also given. For this reaction, only the thermal detector was included since the energy of the produced neutrons falls into the non-linear region. At E_p=1.75 MeV, i.e. below the threshold for neutron production, it is clear that no thermal counts were obtained. Yet, at a projectile energy well above the threshold, with E_p=2.1 MeV and 2.3 MeV, a significant amount of thermal counts were obtained. The difference in the number of counts between the two energies is a factor of 3.5. Partly, this could be related to the higher cross sectional value at the higher projectile energy. At the peak of the resonance ($E_p \approx$2.26 MeV), the difference of the cross section is close to a factor of 2. The reason behind the remaining increase is for the moment unknown.

4.4.2 Moderators

After moderators had been introduced between the detector and the target chamber, the collected data from the thermal detector was processed in a similar manner as the data of the same detector previously discussed. As the normalisation to the charge resulted in too high uncertainties, an attempt was made to normalise the counts in the thermal detector to the counts in the fast detector (integrated over $E_{n,max}$ to 25% of that value). The chosen normalisation procedure is possible since it is the same reaction which is used for neutron production in all of the measurements of the moderators. The uncertainty of the measurements was provided using known formulas of error propagation related to the uncertainty of the model and the number of counts in each channel for both the thermal detector and the fast detector. For each moderator material, four thicknesses were investigated as reported in Chapter 4.2. The number was limited because of the available space and setup possibilities. A compilation of the counts in the thermal detector related to the different moderators is shown in Figure 4.16.

Because of the relatively high uncertainties related to the models used for analysing the data from the fast and thermal detector, and from the statistical uncertainty of the number of counts in each channel, it is not possible to draw any extensive conclusions from Figure 4.16. The findings in Chapter 3.3 were thus not possible to be confirmed in this experiment. Combinations of these moderators were never measured upon. But, as was highlighted in Chapter 3.3, such an arrangement could prove to be a more efficient moderator depending on the specific reaction that will be used in the coming beamline.

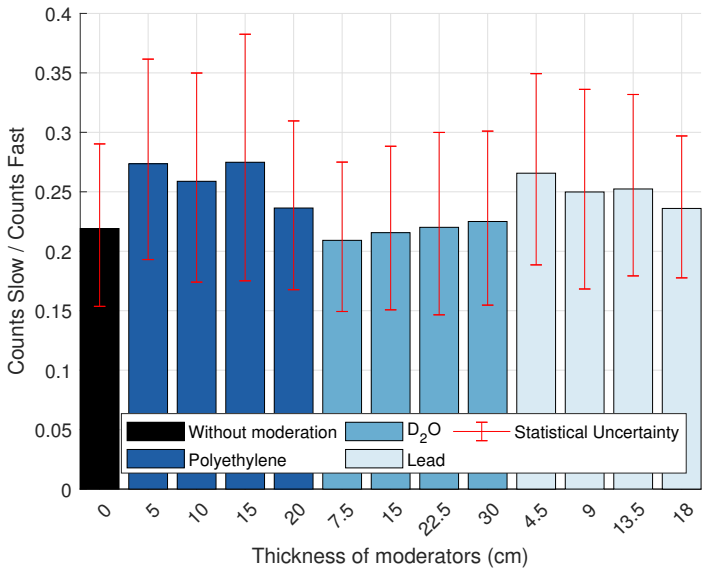

Figure 4.16: A compilation of the counts in the thermal detector when three different moderators were tested; polyethylene, D_2O and lead. Included on each bar is the uncertainty related to both the model used and to the detected number of counts in each channel.

4.4.3 Dump Materials

The calibrated fast spectra from the investigated dump materials are shown in Figure 4.17. As can be seen, the most prolific reaction was that of the carbon target with incident deuterons. The tungsten target displays a similar spectrum as the pure carbon target (although with lower intensity), indicating its composition as a compound of tungsten carbide. In light of this data, and from the discussion in Chapter 3.4, it is clear that pure carbon materials, or compounds including carbon, are unsuitable to be used as materials for the beam dump. On the contrary, Figure 4.17 demonstrates that both copper, nickel and tantalum are promising dump materials for deuteron beams because of their lower neutron yield.

Figure 4.18 shows the counts in the thermal detector for the targets investigated as potential dump materials. The data used for this compilation was treated in a similar manner as was the data for the target materials previously, i.e. by fitting a Gaussian on top of an exponential background. The conclusions drawn from the spectra in Figure 4.17 are confirmed by the data presented in Figure 4.18. Thus, carbon, or materials containing carbon (e.g. tungsten carbide and steel) are not suitable materials in a future beam dump. Titanium was also shown to be an unsuitable material due to its relatively high neutron production. Interestingly, and in contrast to its fast spectrum, aluminium did not indicate the production of a considerable amount of thermal neutrons. The reason for this is unclear, especially since [32] indicates that the cross section for neutron production is higher for the production of lower energy neutrons (note that this data is for E_d=5 MeV).

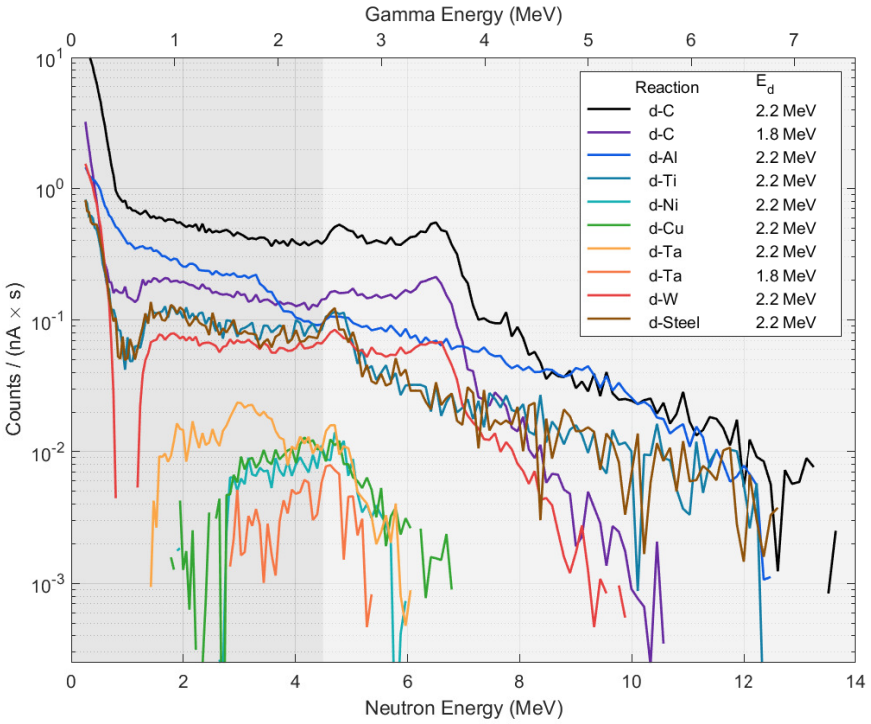

Figure 4.17: Calibrated spectrum of possible dump materials. The light grey/white area indicates the region of energies which was utilised for the calibration.

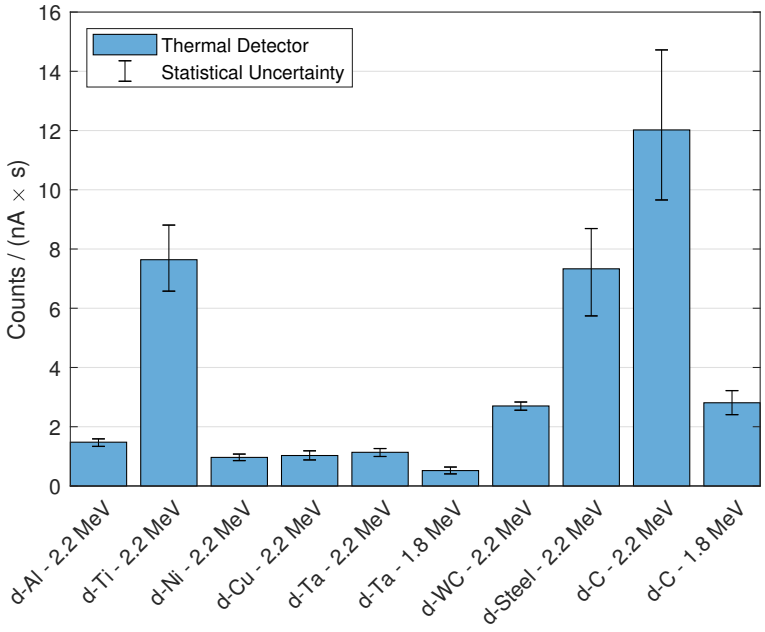

Figure 4.18: Comparison of the number of counts normalised to the charge on measurements of possible dump materials. The compilation originates from the counts obtained after a Gaussian fit was made on an exponential background on the data from the thermal detector.

4.4.4 Coincidence measurement

To demonstrate the measurement of a neutron and a charged particle in coincidence, the d-T-reaction was chosen because of the relatively high energy of the α-particle. A spectrum from the fast neutron detector for this reaction was previously shown in Figure 4.8. The spectra of the charged particle detector can be seen in Figure 4.19, where the calibration was performed using the linear function obtained from the ^{228}Th-measurement. These spectra were recorded with both the thermal and the charged particle detector held in fixed locations during the different measurements. Only the fast detector was mounted at three different locations and angles to the incoming ion beam. Hence, the given angles in the legend of Figure 4.19 are only related to the position of the fast detector in line with Figure 4.5.

In Figure 4.19, the spectra have been normalised to the number of counts in the thermal detector. The number of counts of the thermal detector was obtained by a similar procedure as described in Chapter 4.4.1. The light grey coloured area in between 1.068-2.037 MeV is the region of interest (ROI) which is used as a condition in the following treatment. The regions under the well defined peaks around 1.65 MeV indicate that the number of coincidences is greater at an angle of 3° compared to the two other angles.

The energy values of the detected ions are slightly lower than the value of 2.207 MeV that would would be expected from a kinematic calculations of the recoil of an α at an angle of 162° [1]. This is to be expected, since this equation leaves out the penetration distance needed for an ion to escape from the target, causing a loss of energy as described by Equation 2.8. The varying depth of the fusion reaction causes energy straggling of the ions, as can be seen in Figure 4.19.

Figure 4.20 shows the coincidence spectra related to the fast neutron detector. In this figure, the condition of the ROI has been applied to the data. As anticipated from the kinematics of the reaction, the positioning of the two detectors relative to each other effects the number of coincidences seen in Figure 4.20. It is only for the measurement with the smallest angle between the fast detector and the incoming beam, i.e. at 3°, that the the fast neutron spectrum of the d-T-reaction in Figure 4.8 is relatively well replicated. For the two other angles, this relationship can not be observed.

Figure 4.21 shows the energy-energy-plots of the data from the fast and the charged particle detectors. Therein, the y-axis has been calibrated to the linear function related to the diode detector and the x-axis to the quadratic function related to the fast neutron detector. The coincidence plots indicate the importance of a kinematic analysis to align the system to optimise the statistics. It is noticeable that the energy of the detected neutrons decreases with an increased angle of the fast detector relative to the incoming ion beam. This is to be expected following Equation 2.17, giving the maximum neutron energy at 3° to 16.05 MeV, at 42° to 15.58 MeV and at 60° to 15.14 MeV.

The results presented demonstrates the ability at LIBAF to use coincidence measurements with neutrons, thus providing future experiments with the possibility of having a reduced background. Moreover, since the energy of the detected recoil is known and the kinematics is fixed, the energy of the neutron will also be known within the degree of the ability to measure the energy of the α-particle. As for now, further analysis and tests are required to investigate the possibility of using a coincidence method with other reactions such as d-Li or p-T.

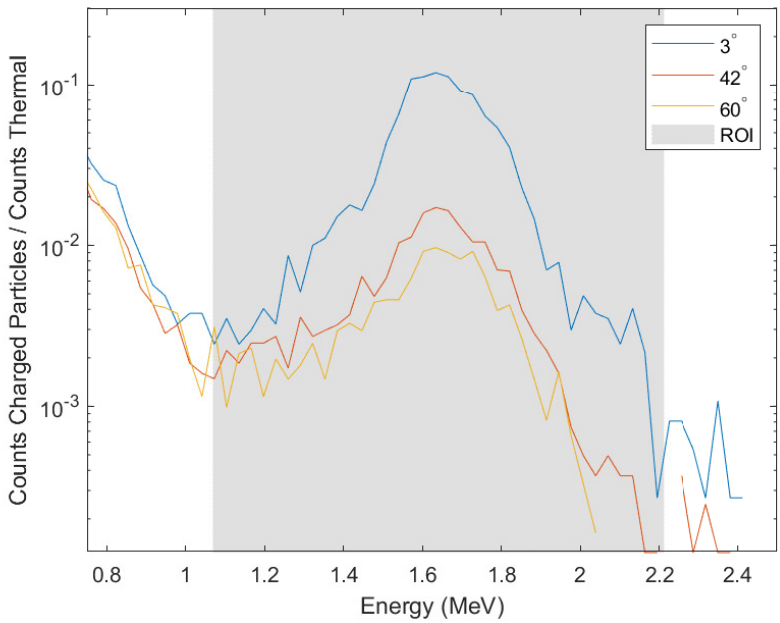

Figure 4.19: The calibrated spectra from charged particle detector for three different angles of the fast detector. The region of interest (ROI) have been marked by light grey in between 1.068 and 2.037 MeV.

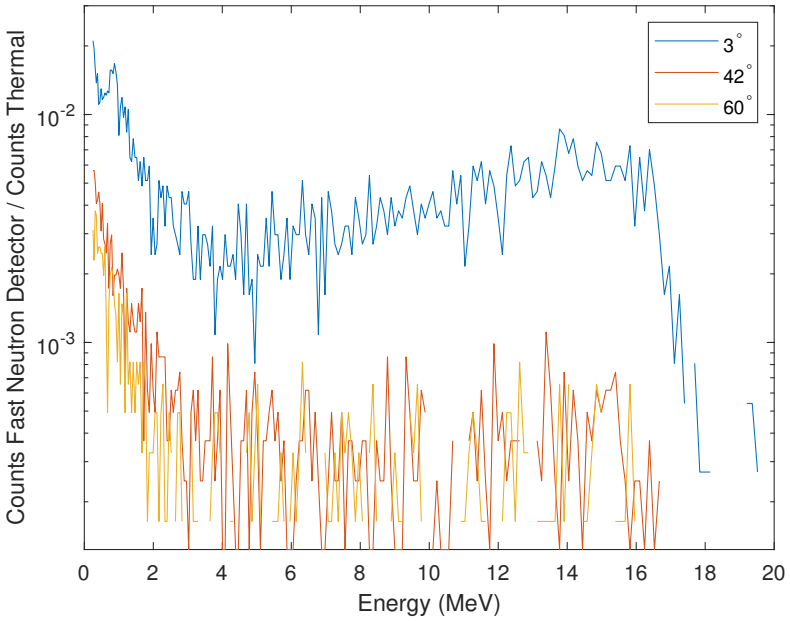

Figure 4.20: The fast neutron spectrum in coincidence with the marked ROI in the diode spectrum of Figure 4.19.

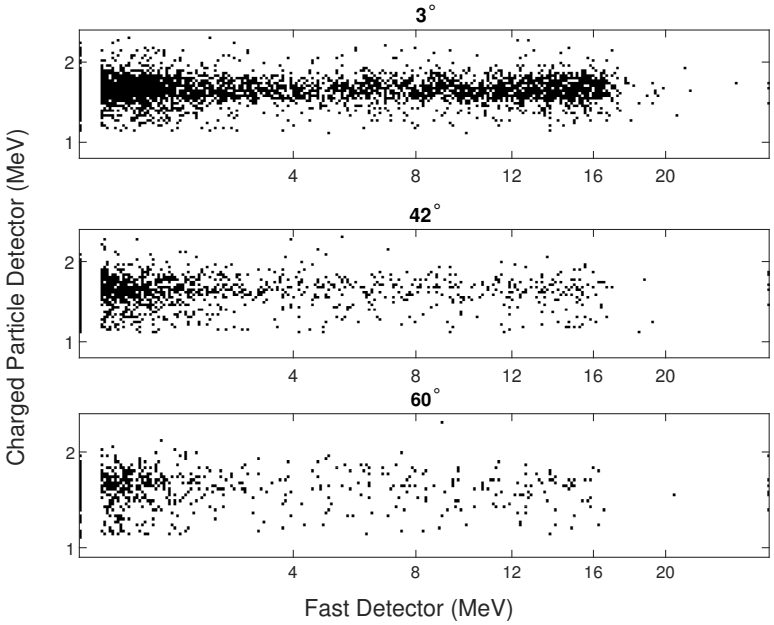

Figure 4.21: Three energy-vs-energy plots for the coincidences between the fast neutron detector (x-axis) and the ions in the region covering the peak at around 1.65 MeV in Figure 4.19 (y-axis).

Chapter 5

Conclusions

In this thesis various topics of importance for the coming neutron beamline have been evaluated with the help of a literature study, calculations and measurements. Included in the evaluation were the topics of nuclear reactions resulting in a high neutron yield using beams of protons or deuterons impinging on low-A-targets, materials for thermalisation of the produced neutrons and materials with a low neutron yield for impinging protons/deuterons suitable to be used in a future beam dump. The evaluation of these topics will be summarised in turn in this chapter, before suggestions of possible improvements and a final recommendation will be given.

5.1 Summary

From the initial theoretical evaluation, a number of different reactions where found to give a feasible flow of neutrons. These reactions were discussed in Chapter 3.2.2. For the most promising reactions, the threshold energy, the maximum neutron energy, the calculated and experimental yield and the target material used have been summarised in Table 5.1.

Table 5.1: A summary of the most useful reactions stating the threshold energy, maximum neutron energy at 0°, calculated and measured yield and target material. The neutron energies and calculated yields stated are given for 2.5 MeV projectiles, except for d-T which is given for E_d=0.6 MeV. The normalised experimental yields are given for 2.2 MeV projectiles. This yield was not measured in the fast detector for p-T, d-T and p-LiF.

Reaction	d-D	p-T	d-T	p-^{7}Li	d-^{7}Li	d-^{9}Be
E_{thres} [MeV]	-	1.02	-	1.88	-	-
$E_{n,max}$ [MeV]	5.76	1.71	16.05	0.79	17.08	6.85
Calc. Yield [n/μC]	2.8E8	4.9E8	2.9E8	2.5E8	3.5E8	9.1E8
Exp. Yield [n/μC]	6.4E8	-	-	-	2.7E8	9.9E8
Target	CD_2	Ti_2T_3	Ti_2T_3	LiF	LiF	Be

Two of the reactions in Table 5.1, p-T and p-^{7}Li, require the projectiles to supercede a minimum threshold energy for the production of neutrons to be possible. Even though such neutrons will have a relatively low maximum kinetic energy, they will need to be moderated to achieve

thermal energy. If a deuteron beam is used instead of protons, neutrons of much higher energies are obtained. This versatility could prove beneficial to a user of the coming neutron beamline at LIBAF, as the facility could provide neutrons with different energies.

Of the calculated yields in Table 5.1, the highest was obtained for the beryllium target using deuteron projectiles. The high yield of the d-Be-reaction was also observed in the fast detector during the experiment as seen in Figure 4.15 and Table 5.1. Beyond its high yield, the use of beryllium as a target material is advantageous for a number of reasons. Its melting point of 1285°C is more than 1000°C higher than that of solid lithium and the temperature where tritium is starting to be released from a TiT_x-target. Its thermal conductivity of 180 W/mK is more than a factor 2 higher than that of metallic lithium. Moreover, beryllium has better mechanical properties than lithium, it is not radioactive and it is easier to handle than both lithium and tritium. The downside of beryllium is its poisonous characteristic. In the controlled environment of the beamline, this should be resolved with proper ventilation.

The yields of the remaining reactions in Table 5.1 are highly dependant on their target compositions. Of the targets with solid deuterium, the deuterated plastic was found to be the most prolific (not considering LiD). Unfortunately, this target suffers from the problem of erosion. Future studies of the durability of such a target is wanted. The use of tritiated titanium is not an optimal solution for a target system, as the incoming ions experience additional stopping power due to the higher Z of titanium. Alternative encapsulating materials are unknown to the author. For the d-D reaction, a higher-yield alternative is to use a gas target. Primarily for reasons of safety, a gas target with tritium is not suggested to be used. A gas target is also unsuitable for the d-T reaction, since its recoil can be used in fast coincidence measurements. The calculated yields of the two reactions with lithium fluoride are also limited by the target composition. Using metallic lithium is possible and would increase the yield between a factor of 3 and 4. The use of metallic lithium is problematic from two points of view, its low melting temperature of 160°C and its high reactivity in air. Alternatives with higher melting point and reduced reactivity, such as lithium hydride/deuteride or lithium fluoride, affect the yield and thermal conductivity negatively. Development on liquid-lithium targets has recently been performed. The possibility of incorporating such devices into the future beamline at LIBAF remains to be studied.

Time tagging of the more energetic neutrons produced by the accelerator is a problem if a deflection system is used. The time uncertainty of when the deflection system shifts the beam on and off is in the order of hundreds of ns [103]. To obtain an effective start signal for the TDC, the detection of the recoil is a requirement. As was demonstrated in Chapter 4.4.4, a coincidence measurement with fast neutrons and a recoil is feasible at LIBAF. Because of its high cross section at lower projectile energies and its high Q-value, the most suitable reaction was found to be the d-T-reaction. The high cross section at lower energies imply that the projectiles will not penetrate the target too deep before the fusion reaction occurs, leaving the recoil with a high probability of escaping the target material. The benefit of performing a coincidence measurement includes the possible removal of background noise. Also beneficial is the possibility of knowing the energy of the neutron to the degree of certainty that the energy of the recoiling ion can be measured. It is worth to note that the use of the recoil product seem to be limited to the use of solid targets. If gaseous or liquid targets are used, the encapsulating container of the gas will block the recoil from escaping and reaching the detector.

In Chapter 3.3 an evaluation of possible moderator materials were presented. From the well known parameters of moderating ratio and power, it is evident that both light and heavy water, ordinary and deuterated plastic and carbon are functional moderator alternatives. During the experiment, three possible moderator materials were measured upon: light water, heavy water and

lead. Unfortunately, as was seen in Figure 4.16, the uncertainties related to the measurements, the model used and the geometry of the moderators, limited the usefulness of the data. From the presented simulation in Chatper 3.3, it is clear that the choice of material will influence not only the thermal flux, but also the quality of the neutron beam and the possible deflection frequency of the pulsed ion beam (because of the pulse broadening). The choice of which moderator material to use will therefore depend on the intended future use of the beamline. If a high thermal flux is of highest priority, the use of heavy water (or deuterated plastic) would be the best choice. If a shorter pulse is preferred, as well as an increased resolution, hydrogenous materials would be the better alternative. The thermal flux could possibly be increased if a premoderator of lead or tungsten was to be used. This is, however, yet to be confirmed experimentally. The optimal dimensions of a moderator will depend on the reaction chosen for neutron production and the projectile energy used. For the final decision of the moderator design, it would be beneficial, as well as necessary, to perform simulations.

An evaluation of materials suited for use in a beam dump was presented in Chapter 3.4 and 4.4.3. It is desirable to keep the neutron production in a beam dump as low as possible for at least two reasons: reducing the background and limiting the activation of the materials inside the beam dump. One of the evaluated elements, carbon, was found to be suitable only for impinging protons because of the threshold for neutron production being higher than the maximum energy that is provided by the accelerator. For impinging deuterons however, a relatively high yield of neutrons was anticipated from the calculations. As can be seen in Figures 4.15 and 4.18, this was observed during the experiment. Carbon is a commonly used material in components of the accelerator at LIBAF (steel and tungsten carbide). If deuterons were to be used for the production of neutrons in the coming beamline, this issue needs to be addressed to limit the increase of background resulting from the use of these projectiles. Of the considered materials, the most interesting for use in a future beam dump for both protons and deuterons were summarised in Table 3.5. The most promising materials were found to be gold or tungsten. The advantage of gold to tungsten was its higher thermal conductivity (a factor of 1.8) as well as its lower electrical resistivity (a factor of 2.4) and Brinell hardness (a factor of 10). The downside, however, was the lower melting point of gold (a factor of 3.2) and the higher cost (a factor of 137). Before a final decision is made of which of the two materials to use, simulations are required related to the activation of the materials as well as to their respective thermal and stress evolution.

5.2 Improvements

The detectors used (plastic scintillators) during the measurements were covered with blocks of lead, enabling the approximation that the influence of γ-contamination on the measurements could be disregarded. Two different techniques to improve the measurements could have been employed, either rigging up a complementary detector to measure the γ produced during the experiment or choosing a detector system with the possibility to discriminate between the pulses resulting from different kind of radiations. In Figure 4.12 it was indicated that 90% of the incoming γ-radiation would be blocked. Hence, with a system of pulse discrimination in place, it would be possible to improve the results by 10%.

In Chapter 4, a quadratic function was suggested as being the better fit to the data over a linear function. To verify that this is an appropriate function to describe the response in the detector, it would be beneficial with more calibration points, especially for lower energies, and with smaller uncertainties. This would also rule out the assumption of 0 eV at the first channel in the calibration. To reduce the uncertainties of the calibration points, a number of different steps

could be taken. The uncertainty related to the maximum energy at a given angle could be reduced by moving the detector further away from the target, limiting the angle of neutron production, translating to an increase of certainty of the knowledge of the maximum neutron energy. If the uncertainty of the angle is reduced from 5° to 1°, the uncertainty of the maximum kinetic energy is reduced roughly by a factor between 3 to 5. By limiting the angle, the measurements could be improved with a similar factor, assuming that the uncertainties propagates proportionally. As the detector is moved further away, the measurement time required to compensate for the reduction of counts with the decrease in solid angle, is inversely proportional to the reduction of the solid angle, i.e. it is increased by a factor of five. A beneficial side-effect of moving the detector away from the target is the decrease of random coincidences causing pile-ups. For d-Be, the rate of random coincidences corresponds to less than 0.1% of the total number of counts, indicating that the effect on the results of having less pile-ups with the increased distance will be minimal.

The uncertainties are affected by the re-binning of the data into 1/32-1/128 of the original channels and the smearing caused by uncertainties in the amplification process. To address the effects of the re-binning used, two steps can be taken. If the experiments were to be allowed to collect additional data by increasing the current or the measuring time, the need for re-binning could be removed. With a similar measurement time, the increased current needed would amount to around 0.13 μA. This is feasible in the accelerator of LIBAF. If the measuring time was increased instead, this would require between 32 to 128 times longer measurements depending on the chosen reaction. For d-Be, which was re-binned into 1/32 of the original channels, this translates to 3 h and 50 minutes of required beam time. The reduction of the resolution caused by the noise introduced in the amplification process could also be improved. The extent of its effect on the result was not investigated, but will need to be considered in the future.

The uncertainties of the results could be reduced further if the uncertainty of the current was to be reduced. With the deflection system in use, the related uncertainty used in experiments at LIBAF is 3% [103]. This would reduce the uncertainties of the results of the fast detector between 7% to 46% and of the thermal detector between 18% and 78%.

5.3 Recommendations

From the evaluation performed in this thesis, the author's recommendation is to use two different target materials, beryllium and TiT_x with impinging deuterons. The beryllium target is to be used for measurements where a high flow of neutrons is of importance and the tritiated titanium target for use in fast coincidence measurements.

If a deuteron beam is to be used in the coming beamline of LIBAF, the materials therein should be considered carefully in order to reduce the background. It is especially important to not include materials involving carbon, e.g. steel or tungsten carbide, or titanium.

Suggested materials for use as moderators are either hydrogeneous or deuterated materials. The final decision will need to be based of the main purpose of the beamline, if the focus primarily is a short pulse with increased resolution or a high thermal flux. Simulations of the moderation process will be needed in order to decide upon the optimal dimensions of the moderator.

A beam dump for both protons and deuterons would benefit from being coated with the higher-Z materials of gold or tungsten. The final choice of which material to use will require simulations related to activation as well as thermal and stress evolution.

Bibliography

[1] K. S. Krane. *Introductory Nuclear Physics.* John Wiley Sons, 1988.

[2] M. Åberg, N. Ahlfors, R. Ainsworth, C. Alba-Simionesco, S. Alimov, N. Aliouane, B. Alling, Kasper Grann Andersson, Niels Hessel Andersen, Britt Rosendahl Hansen, et al. *ESS technical design report.* European Spallation Source, 2013.

[3] Assoc. Prof. Kevin Fissum Prof. Per Kristiansson. A facility for tagged thermal neutrons - application from science and technical faculty.

[4] F. Messi, H. Perrey, K. Fissum, M. Akkawi, R. Al Jebali, J.R.M Annand, P. Bentley, L. Boyd, C.P Cooper-Jensen, D.D DiJulio, et al. The neutron tagging facility at lund university. *arXiv preprint arXiv:1711.10286*, 2017.

[5] Paul Reuss. *Neutron Physics.* EDP Sciences, 2008. ISBN 978-2-7598-0041-4.

[6] J. P. Freidberg. *Plasma Physics and Fusion Energy.* Cambridge University Press, 2007. ISBN 0-511-27375-4.

[7] T. Koohrokhi, A. M. Izadphanah, S. K. Hosseini. Fusion cross section of T(d,n)^{4}He and ^{3}He(d,p)^{4}He reactions by four parameters formula. *J Fusion Energ*, 35, 2016.

[8] W.R. Leo. *Techniques for Nuclear and Particle Physics Experiments.* Springer-Verlag, 1994.

[9] Stefaan Tavernier. *Experimental techniques in nuclear and particle physics.* Springer Science & Business Media, 2010.

[10] B.A. Ludewigt, R.P. Wells, and J. Reijonen. High-yield D-T neutron generator. *Nuclear Instruments and Methods in Physics Research Section B: Beam Interactions with Materials and Atoms*, 261(1):830–834, 2007. Elsevier.

[11] Arnd Junghans. Neutron beams for nuclear data measurements.

[12] J. Meyer-Ter-Vehn S. Atzeni. *Inertial Fusion - Beam Plasma Interaction, Hydrodynamics, Dense Plasma Physics.* Clarendon Press-Oxford, 2004. ISBN 0-19-856264-0.

[13] Huang, WJ and Audi, G and Wang, Meng and Kondev, FG and Naimi, S and Xu, Xing. The AME2016 atomic mass evaluation (I). Evaluation of input data; and adjustment procedures. *Chinese Physics C*, 41(3):030002, 2017.

[14] G. H. Miley D. R. Kingdon A. A. Harms, K. F. Schoepf. *Principles of Fusion Energy.* World Scientific Publishing Co. Pte. Ltd., 2000.

[15] Y. A. Berezhnoy. *The Quantum World of Nuclear Physics*. World Scientific Publishing Co. Pte. Ltd., 2005. ISBN 981-256-387-3.

[16] V. Lamirand. *Determination of cross sections for the production of low-energy monoenergetic neutron fields*. Université de Grenoble, 2011.

[17] K.-H. Schmidt. Deexcitation mechanisms in compound nucleus reactions. 2009.

[18] Simon Fraser University. Direct and compound nucleus reaction, 2017-11-19. URL `https://web-docs.gsi.de/~wolle/TELEKOLLEG/KERN/LECTURE/Fraser/L24.pdf`.

[19] Masatoshi Arai and K Crawford. Neutron sources and facilities. In *Neutron imaging and applications*, pages 13–30. Springer, 2009.

[20] R.M. Ball. Characteristics of nuclear reactors used for the production of molybdenum-99. *IAEA-TECDOC*, 1065:5–17, 1999.

[21] Institut Laue-Langevin, 2018-01-10. URL `https://www.ill.eu/`.

[22] INTERNATIONAL ATOMIC ENERGY AGENCY. *Neutron Generators for Analytical Purposes*. Number 1 in IAEA Radiation Technology Reports. Vienna, 2012. URL `http://www-pub.iaea.org/books/IAEABooks/8505/Neutron-Generators-for-Analytical-Purposes`.

[23] European Spallation Source, 2017-11-20. URL `https://europeanspallationsource.se/`.

[24] S. Peggs, K. Andersen, D. Argyriou, K. Batkov, C. B'ohme, S. Bousson, I. Bustinduy, C. Carlile, P. Carlsson, L. Celona, et al. ESS conceptual design report. 2012.

[25] NG Sjöstrand. Reaktorfysik - föreläsningar av professor N.G. Sjöstrand, 1996. Chalmers University of Technology.

[26] Julius Scherzinger. Neutron irradiation techniques. 2016. Lund University, Faculty of Science, Department of Physics.

[27] Richard B. Firestone, Virgina S. Shirley, C.M. Baglin, S.Y. Frank Chu, and J. Zipkin. Table of isotopes, 8-th ed. *John Willey & Sons, New York*, 1996.

[28] JF Ziegler. Stopping of energetic light ions in elemental matter, version SRIM-2012.

[29] V. Valkovic. *14 MeV Neutrons*. CRC Press, 2016. ISBN 978-1-4822-3801-3.

[30] J.I.W. Watterson. Accelerators for neutron generation and their applications. *Reviews of Accelerator Science and Technology*, 4, 2012.

[31] Richard T. Kouzes and James H. Ely. Status summary of ^{3}He and neutron detection alternatives for homeland security. Technical report, Pacific Northwest National Laboratory (PNNL), Richland, WA (US), 2010.

[32] Experimental Nuclear Reaction Data (EXFOR), 2018-01-19. URL `https://www-nds.iaea.org/exfor/exfor.htm`.

[33] A.J. Koning, D. Rochman, J. Kopecky, M. Fleming Sublet, E. Bauge, S. Hilaire, P. Romain, B. Morillon, H. Duarte, S. van der Marck, et al. TENDL-2015: TALYS-based evaluated nuclear data library, 2015.

[34] J.J. Devaney. ^{9}Be(d,n)^{10}B cross section in the range 0 to 2.8 MeV. 1972. doi: 10.2172/4635530.

[35] D Karamanis. A study on the utilization of tritide titanium targets for monoenergetic neutron production. *Nuclear Instruments and Methods in Physics Research Section B: Beam Interactions with Materials and Atoms*, 195(3-4):350–357, 2002. Elsevier.

[36] American Elements - The Advanced Elements Manufacturer, 2018-05-17. URL `https://www.americanelements.com`.

[37] M. Drosg. DROSG-2000, PC database for 56 neutron source reactions. *Documented in the report IAEA-NDS-87 Rev*, 5, 2000.

[38] M.A. Lone, C.B. Bigham, J.S. Fraser, H.R. Schneider, T.K. Alexander, A.J. Ferguson, and A.B. McDonald. Thick target neutron yields and spectral distributions from the ^{7}Li(pd, n) and ^{9}Be(pd, n) reactions. *Nuclear Instruments and Methods*, 143(2):331–344, 1977. Elsevier.

[39] Robert Wray Hamm and Marianne Elizabeth Hamm. *Industrial accelerators and their applications*. World Scientific, 2012.

[40] Q-value calculator, 2017-11-22. URL `https://www.nndc.bnl.gov/qcalc/index.jsp`.

[41] C. R. Brune et al. Total cross section of the ^{3}H(p,n)^{3}He reaction from threshold to 4.5 MeV. *Physical Review C*, 60:1, 1999.

[42] H. Liskien, A. Paulsen. Neutron Production Cross Sections And Energies For The Reactions T(p,n)^{3}He,D(d,n)^{3}He, And T(d,n)^{4}He. *Nuclear Data Tables*, 11, 1973.

[43] M. Drosg, N. Otuka. Evaluation of the Absolute Angle-Dependent Differential Neutron Production Cross Sections by the Reactions ^{3}H(p,n)^{3}He, ^{1}H(t,n)^{3}He, ^{2}H(d,n)^{3}He, ^{3}H(d,n)^{4}He, and ^{2}H(t,n)^{4}He and of the Cross Sections of Their Time-Reversed Counterparts up to 30 MeV and Beyond. *INDC (AUS)-0019*, 2015.

[44] J. H. Gibbons, R. L. Macklin. Total neutron yields from light elements under proton and alpha bombardment. *Physical Review*, 114, 1958.

[45] Live chart of nuclides, 2018-04-12. URL `https://www-nds.iaea.org/relnsd/vcharthtml/VChartHTML.html`.

[46] A. Meulenberg, K. P. Sinha. Decay Modes of excited ^{4}He below the fragmentation levels. 2011.

[47] T. P. Lou. Compact D-D/D-T Neutron Generators And Their Applications. 2003.

[48] Y. Kim, J.M. Mack, H.W. Herrmann, C.S. Young, G.M. Hale, S. Caldwell, N.M. Hoffman, S.C. Evans, T.J. Sedillo, A. McEvoy, et al. Determination of the deuterium-tritium branching ratio based on inertial confinement fusion implosions. *Physical Review C*, 85(6): 061601, 2012. APS.

[49] G.L. Morgan, P.W. Lisowski, S.A. Wender, Ronald E. Brown, Nelson Jarmie, John F. Wilkerson, and D.M. Drake. Measurement of the branching ratio ^{3}H(d,γ)/^{3}H(d,n) using thick tritium gas targets. *Physical Review C*, 33(4):1224, 1986.

[50] Konstantin V. Mitrofanov, Vladimir M. Piksaikin, Konstantin I. Zolotarev, Andrey S. Egorov, and Dmitrii E. Gremyachkin. The energy spectrum of neutrons from ^{7}Li(d,n)^{8}Be reaction at deuteron energy 2.9 MeV. In *EPJ Web of Conferences*, volume 146, page 11041. EDP Sciences, 2017.

[51] Jingsheng Yan, F.E. Cecil, J.A. McNeil, M.A. Hofstee, and P.D. Kunz. Deuteron-induced reactions on ^{9}Be, ^{10}B, and ^{11}B at low energies. *Physical Review C*, 55(4):1890, 1997. APS.

[52] Christian Nussbaum. *Effets d'interférences dans la réaction ^{7}Li(d,n)^{8}Be au voisinage de la résonance à l MeV*. PhD thesis, Birkhäuser, 1969.

[53] D.R. Tilley, J.H. Kelley, J.L. Godwin, D.J. Millener, J.E. Purcell, C.G. Sheu, and H.R. Weller. Energy levels of light nuclei A= 8, 9, 10. *Nuclear Physics A*, 745(3-4):155–362, 2004.

[54] J. W. Meadows. The ^{9}Be(d,n) thick-target neutron spectra for deuteron energies between 2.6 and 7.0 MeV. *Nuclear Instruments and Methods in Physics Research*, A324, 1993.

[55] J.I.W. Watterson. Use of accelerator based neutron sources: A review of accelerator based neutron sources and their applications. 2000.

[56] R.A. Forrest et al. *The European activation system: EASY-2007 overview*. Citeseer, 2007.

[57] Donald J. Gillich, Andrew Kovanen, and Yaron Danon. Deuterated target comparison for pyroelectric crystal D–D nuclear fusion experiments. *Journal of Nuclear Materials*, 405(2): 181–185, 2010. Elsevier.

[58] M. Febbraro, D. Walter, S.C. Shadrick, S.D. Pain, K.A. Chipps, C. Thornsberry, and E. Lesser. Improved technique for preparation of deuterated-polyethylene targets. *Nuclear Instruments and Methods in Physics Research Section B: Beam Interactions with Materials and Atoms*, 410:53–59, 2017. Elsevier.

[59] Axel Klix, Toralf Döring, Alexander Domula, and Kai Zuber. The intensive DT neutron generator of TU Dresden. In *EPJ Web of Conferences*, volume 170, page 02004. EDP Sciences, 2018.

[60] Sudhirsinh Vala, M Abhangi, Ratnesh Kumar, B Sarkar, and M Bandopadhyay. Rotating tritium target for intense 14-MeV neutron source. *Fusion Engineering and Design*, 123: 77–81, 2017. Elsevier.

[61] T. Senga, H. Sakane, M. Shibata, H. Yamamoto, K. Kawade, Yoshimi Kasugai, Yujiro Ikeda, and Hiroshi Takeuchi. Measurement of neutron activation cross sections in the energy range between 2 and 7 MeV by using a Ti-deuteron target and a deuteron gas target. Technical report, 2000.

[62] B. Bayanov, V. Belov, and S. Taskaev. Neutron producing target for accelerator based neutron capture therapy. In *Journal of Physics: Conference Series*, volume 41, page 460. IOP Publishing, 2006.

[63] Raleigh L. McKisson. The Preparation of a Lithium Deuteride Casting and Some Properties of Lithium Deuteride. 1950.

[64] M. Friedman, D. Cohen, M. Paul, D. Berkovits, Y. Eisen, G. Feinberg, G. Giorginis, S. Halfon, A. Krasa, A.J.M. Plompen, et al. Simulation of the neutron spectrum from the ^{7}Li(p,n) reaction with a liquid-lithium target at Soreq Applied Research Accelerator Facility. *Nuclear Instruments and Methods in Physics Research Section A: Accelerators, Spectrometers, Detectors and Associated Equipment*, 698:117–126, 2013. Elsevier.

[65] S. Halfon, M. Paul, A. Arenshtam, D. Berkovits, M. Bisyakoev, I. Eliyahu, G. Feinberg, N. Hazenshprung, D. Kijel, A. Nagler, et al. High-power liquid-lithium target prototype for accelerator-based boron neutron capture therapy. *Applied Radiation and Isotopes*, 69 (12):1654–1656, 2011. Elsevier.

[66] Santiago Terrón, F. Sordo, Miguel Magán, A. Ghiglino, F. Martinez, P.J. de Vicente, R. Vivanco, Knud Thomsen, J.M. Perlado, Francisco Javier Bermejo, et al. Conceptual design of the beryllium rotating target for the ESS-Bilbao facility. *Nuclear Instruments and Methods in Physics Research Section A: Accelerators, Spectrometers, Detectors and Associated Equipment*, 724:34–40, 2013. Elsevier.

[67] Hiroaki Kumada, Toshikazu Kurihara, Masakazu Yoshioka, Hitoshi Kobayashi, Hiroshi Matsumoto, Tomei Sugano, Hideyuki Sakurai, Takeji Sakae, and Akira Matsumura. Development of beryllium-based neutron target system with three-layer structure for accelerator-based neutron source for boron neutron capture therapy. *Applied Radiation and Isotopes*, 106:78–83, 2015. Elsevier.

[68] R.H. Siemssen, R. Felst, M. Cosack, and J.L. Weil. The reaction ^{19}F(d,n)^{20}Ne. *Nuclear Physics*, 52:273–285, 1964. Elsevier.

[69] Z. Elekes, A.Z. Kiss, I. Biron, T. Calligaro, and J. Salomon. Thick target γ-ray yields for light elements measured in the deuteron energy interval of 0.7–3.4 MeV. *Nuclear Instruments and Methods in Physics Research Section B: Beam Interactions with Materials and Atoms*, 168(3):305–320, 2000. Elsevier.

[70] T. Mollik, M.M. Hossain, S. Hasan, M.A.R. Sarkar, and M.A. Zulquarnain. Conceptual Study and Analysis of Neutron Diffusion and Moderation in Nuclear Reactor.

[71] P. Rinard. Neutron interactions with matter. *Passive Nondestructive Assay of Nuclear Materials*, (375-377), 1991. NUREG/CR-5550, US Nuclear Regulatory Commission, Washington, DC.

[72] A. Borio, M. Cagnazzo, F. Marchetti, P. Pappalardo, and A. Salvini. Moderating ratio parameter evaluation for different materials by means of Monte Carlo calculations and reactivity direct measurements. 2004.

[73] New Jersey Department of health and senior services. Hazardous Substance Fact Sheet. 2004.

[74] Hiroyuki Hasemi, Fujio Hiraga, and Yoshiaki Kiyanagi. Neutronic studies on a pulsed thermal neutron source based on the Be(p,n) reaction by using a compact proton accelerator. *Physics Procedia*, 26:88–96, 2012. Elsevier.

[75] Yasuo Wakabayashi, Atsushi Taketani, Takao Hashiguchi, Yoshimasa Ikeda, Tomohiro Kobayashi, Sheng Wang, Mingfei Yan, Masahide Harada, Yujiro Ikeda, and Yoshie Otake. A function to provide neutron spectrum produced from the ^{9}Be+p reaction with protons of energy below 12 MeV. *Journal of Nuclear Science and Technology*, pages 1–9, 2018. Taylor & Francis.

[76] Jinzhao Zhang and Xianguo Tuo. PGNAA neutron source moderation setup optimization. *arXiv preprint arXiv:1309.1308*, 2013.

[77] Hiroyuki Hasemi, Takashi Kamiyama, and Yoshiaki Kiyanagi. Studies on a pulsed thermal/epithermal neutron source with a compact accelerator for neutron imaging. *Physics Procedia*, 43:86–91, 2013. Elsevier.

[78] John M Carpenter. Cold moderators for pulsed neutron sources. Technical report, Argonne National Lab., IL (USA), 1990.

[79] Heidrun Barnert-Wiemer. Conceptual Design of a Cold Methane Moderator System for the European Spallation Source (ESS). 2002.

[80] U. Rücker, T. Cronert, J. Voigt, J.P. Dabruck, P.-E. Doege, J. Ulrich, R. Nabbi, Y. Beßler, M. Butzek, M. Büscher, et al. The Jülich high-brilliance neutron source project. *The European Physical Journal Plus*, 131(1):19, 2016. Springer.

[81] Isowater, 2018-07-01. URL `https://www.isowater.com`.

[82] Yong Zhou. *Nuclear Power Generation: Modern Power Station Practice*. Elsevier, 2013.

[83] Richard Edwin Nightingale. *Nuclear Graphite: Prepared under the Auspices of the Division of Technical Information United States Atomic Energy Commission*. Academic press, 2013.

[84] Cheng Dao-wen, Lu Jing-bin, Yang Dong, Wang Hui-dong, and Ma Ke-yan. Improvement of the moderator's thermalization efficiency for 14 MeV neutrons in boron neutron capture therapy. *Journal of Radioanalytical and Nuclear Chemistry*, 292(3):1085–1088, 2012. Springer.

[85] D. Flammini, R. Pilotti, and A. Pietropaolo. A possible approach to 14 MeV neutron moderation: A preliminary study case. *Applied Radiation and Isotopes*, 125:129–133, 2017. Elsevier.

[86] S.P. Simakov, P. Bém, V. Burjan, U. Fischer, R.A. Forrest, M. Götz, M. Honusek, H. Klein, V. Kroha, J. Novák, et al. Activation of the IFMIF prototype accelerator and beam dump by deuterons and protons. *Fusion Engineering and Design*, 83(10):1543–1547, 2008. URL `https://www.sciencedirect.com/journal/fusion-engineering-and-design/vol/83/issue/10`. Elsevier.

[87] M. Parro, P. Karditsas, A. Caloutsis, D. Iglesias, B. Brañas, and A. Abánades. Corrosion and activation analysis of the LIPAC beam dump cooling circuit. *Fusion Engineering and Design*, 88(6):827–830, 2013. Elsevier.

[88] Bharat Singh Rawat, Sudhirsinh Vala, Mitul Abhangi, Ratnesh Kumar, and Sanket Chauhan. Design and Simulation of 10kW Faraday Cup for Ion Beam Current Measurement. In *2017 25th International Conference on Nuclear Engineering*, pages V009T15A051–V009T15A051. American Society of Mechanical Engineers, 2017.

[89] S. Virostek, D. Oshatz, and J. Staples. A thermal analysis model for high power density beam stops. In *Particle Accelerator Conference, 2001. PAC 2001. Proceedings of the 2001*, volume 2, pages 1577–1579. IEEE, 2001.

[90] Walter Benenson, John W Harris, Horst Stöcker, and Holger Lutz. *Handbook of physics*. Springer Science & Business Media, 2006.

[91] Goodfellow, 2018-09-07. URL http://www.goodfellow.com.

[92] S. Virostek, D. Oshatz, and J. Staples. A thermal analysis model for high power density beam stops. In *Particle Accelerator Conference, 2001. PAC 2001. Proceedings of the 2001*, volume 2, pages 1577–1579. IEEE, 2001.

[93] Proton and Deuteron induced Activation of the IFMIF Prototype Accelerator and Beam Dump components, 2018-07-13. URL http://www.ccfe.ac.uk/easy2007/prague2009/eaf2009-13_simakov.pdf.

[94] ESS Bilbao, 2018-07-16. URL https://www.essbilbao.org/index.php/en/component/docman/doc_view/434-05-bedu-00-1300-ess-00-pre-ganil-review-jan.

[95] Dr. Linus Ros. A detector system for light–element analysis using a nuclear microprobe: for applications in geoscience. 2016.

[96] Saint Gobain Ceramics Plastics, Inc. BC-400,BC-404,BC-408,BC-412,BC-416 Premium Plastic Scintillators, 2018-05-07. URL https://www.crystals.saint-gobain.com/sites/imdf.crystals.com/files/documents/bc400-404-408-412-416-data-sheet.pdf.

[97] Sara A. Pozzi, James A. Mullens, and John T. Mihalczo. Analysis of neutron and photon detection position for the calibration of plastic (BC-420) and liquid (BC-501) scintillators. *Nuclear Instruments and Methods in Physics Research Section A: Accelerators, Spectrometers, Detectors and Associated Equipment*, 524(1-3):92–101, 2004. Elsevier.

[98] Mark A. Norsworthy, Alexis Poitrasson-Rivière, Marc L. Ruch, Shaun D. Clarke, and Sara A. Pozzi. Evaluation of neutron light output response functions in EJ-309 organic scintillators. *Nuclear Instruments and Methods in Physics Research Section A: Accelerators, Spectrometers, Detectors and Associated Equipment*, 842:20–27, 2017. Elsevier.

[99] Daniel Söderstrom. Development of a Detector System for Detection of Thermal Neutrons from Spent Nuclear Fuel. 2016.

[100] Mass attenuation coefficient, 2018-04-16. URL https://physics.nist.gov/PhysRefData/XrayMassCoef/ElemTab/z82.html.

[101] Private communication with Nicholai Mauritzson.

[102] Nathaly De La Rosa, Per Kristiansson, E.J. Charlotta Nilsson, Linus Ros, Mikael Elfman, and Jan Pallon. Lithium analysis using a double-sided silicon strip detector at LIBAF. *Nuclear Instruments and Methods in Physics Research Section B: Beam Interactions with Materials and Atoms*, 404:29–33, 2017. Elsevier.

[103] Private communication with Prof. Per Kristiansson.